Modeling of Metal Particle Combustion

Detailed Numerical Studies of Micron-sized Iron and Aluminum Particles

Qiu, Yue

2025

Document Version:
Publisher's PDF, also known as Version of record

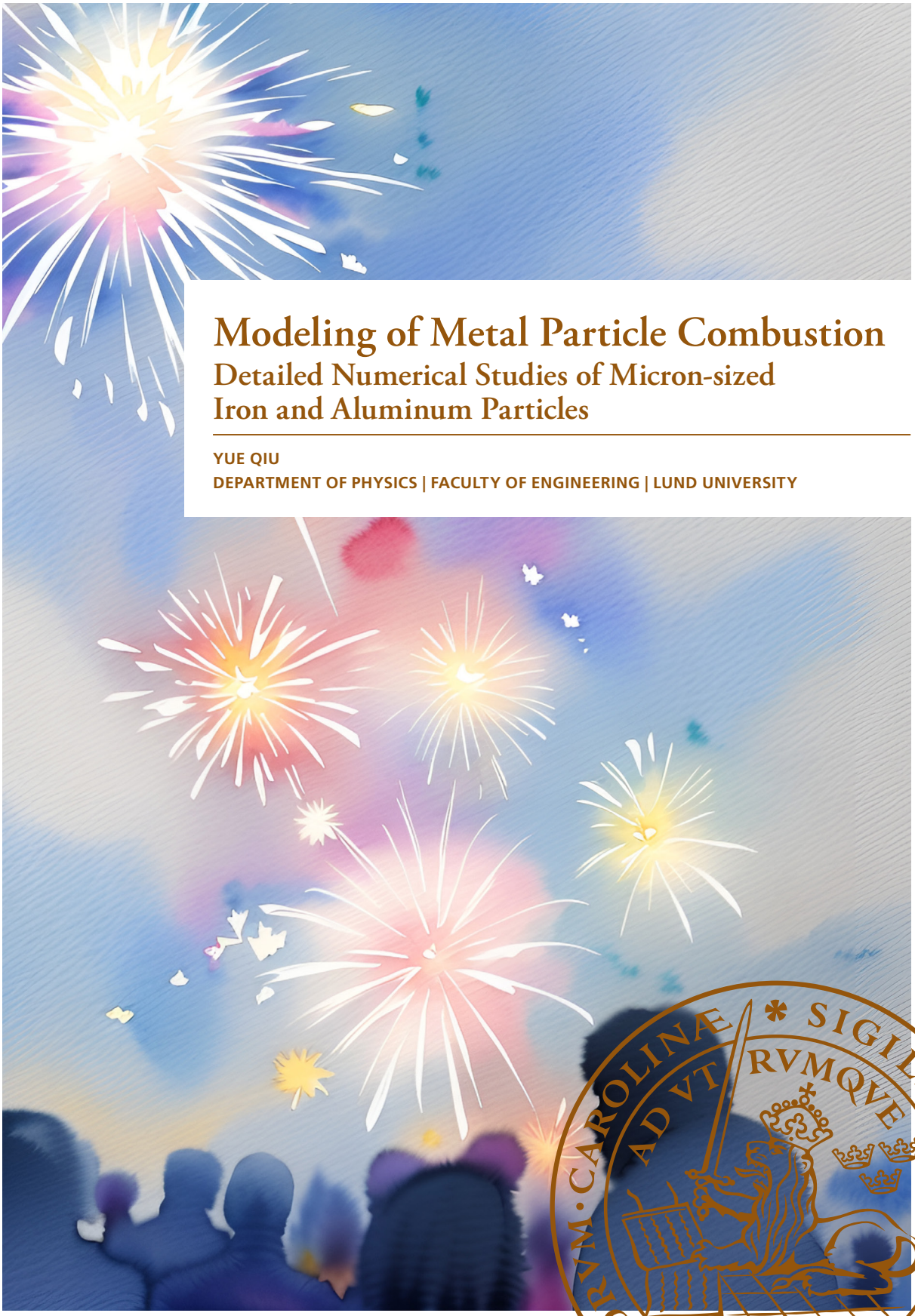

Modeling of Metal Particle Combustion

Detailed Numerical Studies of Micron-sized Iron and Aluminum Particles

YUE QIU
DEPARTMENT OF PHYSICS | FACULTY OF ENGINEERING | LUND UNIVERSITY

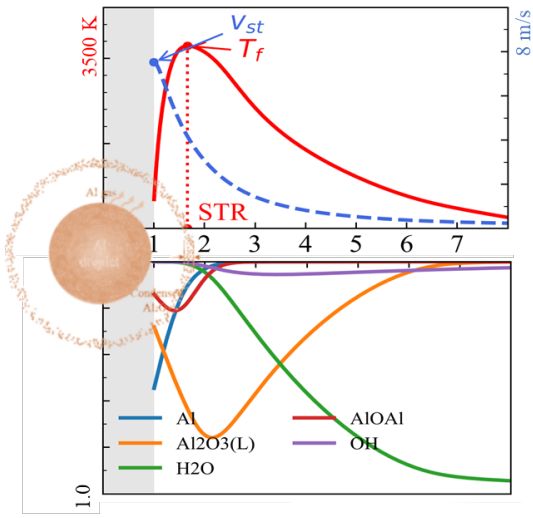

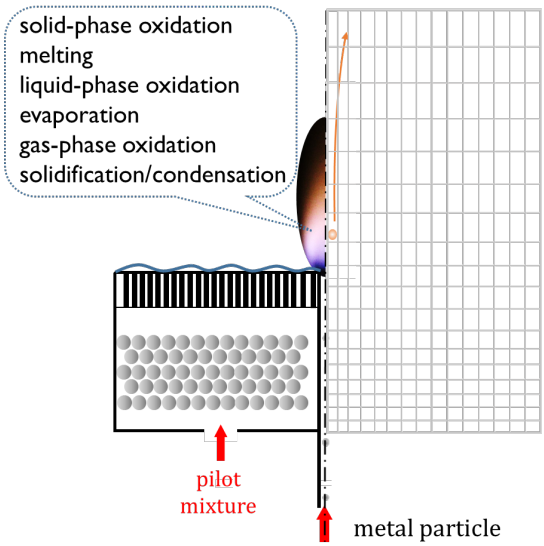

Printed by Media-Tryck, Lund 2025 NORDIC SWAN ECOLABEL 3041 0903

LUND UNIVERSITY

Faculty of Engineering
Department of Physics

Lund Reports on Combustion Physics, LRCP-265
ISBN 978-91-8104-417-1
ISSN 1102-8718

Modeling of Metal Particle Combustion

Modeling of Metal Particle Combustion

Detailed Numerical Studies of Micron-sized Iron and Aluminum Particles

by Yue Qiu

LUND
UNIVERSITY

Thesis for the degree of Doctor of Philosophy
Thesis advisors: Dr. Elna Heimdal Nilsson, Prof. Xue-Song Bai
Faculty opponent: Prof. Christian Hasse

To be presented, with the permission of the Faculty of Engineering of Lund University, for public criticism in the Rydberg lecture hall at the Department of Physics on Friday, the 4th of April 2025 at 09:00.

Organization
LUND UNIVERSITY
Department of Physics
Box 118
SE–221 00 Lund
Sweden

Document name
DOCTORAL DISSERTATION
Date of disputation
2025-04-04
Sponsoring organization

Author(s)
Yue Qiu

Title and subtitle
Modeling of Metal Particle Combustion: Detailed Numerical Studies of Micron-sized Iron and Aluminum Particles

Abstract

Metal fuels can be promising candidates as alternative energy sources and renewable energy carriers within the metal-fuel cycle. They feature high energy density, low environmental impact, and broad production and application. One challenge in metal particle combustion lies in its multi-physics complexity compared to traditional hydrocarbon fuels. This thesis intends to investigate the combustion physics of a single Iron (Fe) or Aluminum (Al) particle with currently available and self-designed modeling tools.

One novelty of this thesis is the construction of a generalized single metal particle combustion scheme, including sub-stages of solid-phase oxidation, melting, liquid-phase oxidation, evaporation, gas-phase oxidation, and solidification/condensation. Relevant reactants and products are identified for each sub-stage, and the kinetic rate is quantified. The constructed combustion scheme can characterize the vapor phase reaction dominated Al combustion and the heterogeneous surface reaction dominated Fe combustion.

Another novelty is the proposal of two models based on the OpenFOAM-7 platform: the metal "Point particle model" within the Lagrangian-Eulerian framework and the "Boundary layer resolved model" within the Eulerian framework, from different aspects of the above-generalized combustion scheme. The metal "Point particle model" intends to capture the whole combustion process of single Fe / Al particles. For Fe modeling, the predicted temperature evolution of a single Fe particle shows a similar trend to the experimental radiant intensity curve. The proposed conjecture of "super-cooled solidification" explains the experimentally observed radiant intensity jump. For Al, a "Melt-Ejection-Model"(MEM) is proposed to explain the observed pre-ignition phenomenon. The simulated Ignition Delay Time (IDT) statistically correlates well with experimental data. The detailed flame structure of a micron-sized Al droplet in hot steam-dominated environments is simulated with the "Boundary layer resolved model". Good agreement with experiment data is observed in the flame temperature for all the droplet sizes, and in the flame stand-off ratio and the Stefan flow velocity for the small droplet size group. Lastly, this thesis provides the first comprehensive review and analysis of Al / O_2 / H_2O gas-phase combustion kinetics in a "real-case" droplet combustion simulation based on the "Boundary layer resolved model".

It is hoped that this thesis can provide new foundational insights as well as some analyzing models for readers interested in the combustion kinetics and modeling of single metal particles.

Key words
Metal fuel, Micron-sized particle, Numerical Modeling, Combustion kinetics, Flame structure

Classification system and/or index terms (if any)

Supplementary bibliographical information

Language
English

ISSN and key title

ISBN
978-91-8104-417-1 (print)
978-91-8104-418-8 (pdf)

Recipient's notes

Number of pages
218

Price

Security classification

Signature _____ Date 2025-02-15

Modeling of Metal Particle Combustion

Detailed Numerical Studies of Micron-sized Iron and Aluminum Particles

by Yue Qiu

LUND
UNIVERSITY

Cover illustration front: A beautiful watercolor style painting generated by **PortraitArt** based on a photo taken by the author during the 2024 New Year's Eve fireworks show at Sankt Hans Hills in Lund.

Cover illustration back: Illustration of the metal "Point particle model" and the "Boundary layer resolved model" proposed in this thesis.

Funding information: This work was financially supported by the Knut and Alice Wallenberg (KAW) Foundation within the COCALD project. The computations were enabled by resources provided by the National Academic Infrastructure for Supercomputing in Sweden (NAISS) and the Swedish National Infrastructure for Computing (SNIC) at NSC, HPC2N, and PDC, partially funded by the Swedish Research Council through grant agreements no. 2022-06725 and no. 2018-05973, and for awarding access to the LUMI supercomputer, owned by the EuroHPC Joint Undertaking, hosted by CSC (Finland) and the LUMI consortium.

Faculty of Engineering, Department of Physics

ISBN: 978-91-8104-417-1 (print)
ISBN: 978-91-8104-418-8 (pdf)
ISSN: 1102-8718
LRCP: LRCP-265

Printed in Sweden by Media-Tryck, Lund University, Lund 2025

Media-Tryck is a Nordic Swan Ecolabel certified provider of printed material. Read more about our environmental work at www.mediatryck.lu.se

Printed matter 3041 0903

MADE IN SWEDEN

Dedicated to my parents
Yingjing Qiu and Fang Liu

Contents

List of publications

This thesis is based on the following publications, referred to by their Roman numerals:

I **Phase change and combustion of iron particles in premixed CH_4 / O_2 / N_2 flames**
S. Xu, **Y. Qiu**, L. Xu, J. Huang, S. Li, E. J. K. Nilsson, Z. Li, W. Cai, M. Aldén, X.-S. Bai
Combustion and Flame, 259 (2024): 113171

II **Modeling of micron-sized aluminum particle combustion in hot gas flow**
S. Feng, **Y. Qiu**, S. Xu, Z. Wu, C. Ruan, A. Roth, E. J. K. Nilsson, E. Berrocal, Z. Li, M. Aldén, X.-S. Bai
Fuel, 369 (2024): 131718

III **Detailed numerical simulation and experiments of a steadily burning micron-sized aluminum droplet in hot steam**
Y. Qiu, S. Feng, Z. Wu, S. Xu, C. Ruan, X.-S. Bai, E. J. K. Nilsson, M. Aldén, Z. Li
Proceedings of the Combustion Institute, 40 (2024): 105717

IV **A comprehensive review of aluminum gas phase combustion kinetics in oxygen and steam environments**
Y. Qiu, X.-S. Bai, E. J. K. Nilsson
Renewable and Sustainable Energy Reviews, under review

V **An updated kinetic mechanism for aluminum gas phase combustion in oxygen and steam environments**
Y. Qiu, X.-S. Bai, E. J. K. Nilsson
Manuscript for journal submission.

Related work

VI **Combustion of micron-sized Al-Mg alloy wires in hot H_2O / O_2 / N_2 flows**

C. Ruan, Z. Wu, M. Stiti, M. Snellman, **Y. Qiu**, A. Ahamed Subash, E. Berrocal, M. Aldén, Z. Li
Fuel, 357 (2024): 129719

VII **Flame structure of single aluminum droplets burning in hot steam-dominated flows**
Z. Wu, C. Ruan, **Y. Qiu**, M. Stiti, S. Xu, N. Jüngst, E. Berrocal, M. Aldén, X.-S. Bai, Z. Li
Combustion and Flame, 271 (2025): 113838

VIII **Quantitative measurement of aluminum atom number density around a burning micron-sized aluminum droplet using spatially resolved laser absorption spectroscopy**
C. Ruan, Z. Wu, **Y. Qiu**, E. Berrocal, M. Aldén, X.-S. Bai, Z. Li
Combustion and Flame, under review

Acknowledgements

More than four years have passed before I finally reach the end of this PhD journey. I would like to thank all the people who have stayed with me along this journey. Without you, I would not be able to accomplish this metal research project.

This work was financially supported by the Knut and Alice Wallenberg (KAW) Foundation within the COCALD project. The computations were enabled by resources provided by the National Academic Infrastructure for Supercomputing in Sweden (NAISS) and the Swedish National Infrastructure for Computing (SNIC). I am grateful for this opportunity to pursue my PhD under this project.

I would like to express my gratitude to my main supervisor Dr. *Elna Heimdal Nilsson*. When I first arrived here in December 2020, the division was about to close due to COVID-19, and we were recommended to work from home. You texted me and asked if I need some food you can go and buy for me. That was a very warm welcome to me. You set a very good example for me at work in terms of time management and your consistently positive attitude. You are there helping out whenever I need you and, at the same time, also encourage me to think independently. I appreciate that very much.

I would also like to express my gratitude to my co-supervisor Prof. *Xue-Song Bai* from the Department of Energy Sciences. Your expertise and experience in computational fluid dynamics, as well as combustion chemistry, are really helpful in my PhD project. You can always grab the key points and come up with nice ideas from a bunch of simulation data and literature studies. I benefited a lot from those scientific discussions with you.

I would like to extend my gratitude to Assoc. Prof. *Yong Qian* from my master's group. It is you who passed the advertisement for this PhD position to me. Dr. *Shijie Xu*, thank you for introducing me to the OpenFOAM software and helping me overcome the initial challenges using the software. You also designed the first version of the metal point particle model code when we were working on Fe combustion. I benefited a lot from your guidance on programming, manuscript writing, and career discussions. I wish you all the best on your academic journey. I would also like to thank *Yuchen Zhou* from Prof. Bai's group. Your expertise in programming and code implementation helps me fix the bugs so quickly and efficiently. Thank you my collaborator *Sheng Feng* from Prof. Bai's group, your contributions to those publications mean a lot. Thank you all for the fruitful discussions on this project.

I would also like to thank my collaborators from the Lund Metal Research Lab. Prof. *Zhongshan Li*, thank you for organizing those weekly metal meetings where I can be involved in fresh experimental discussions. *Zhiyong Wu*, thank you for your effort in pushing forward the metal particle experiments. I feel I can always trust your experimental data. The new

phenomena from your experiment observations inspired my modeling work a lot. Thank you very much also for your generosity and openness in sharing and discussing the experimental data. Dr. *Shen Li*, Dr. *Jianqing Huang*, and Dr. *Can Ruan*, thank you for your effort in experimental measurements and patience in answering my questions regarding experiments. I learned a lot from those discussions.

I would also like to give my sincere thanks to all the colleagues here in the combustion division for creating a friendly, pleasant, and encouraging working environment. Thank you *Marcus Aldén*, *Per-Erik Bengtsson*, and *Joakim Bood* for taking good care of the whole division. Thank you *Vladimir Alekseev*, *Martin Passad*, and *Frej Ryde* for sharing our kinetic group. We should have more hiking mornings and pizza nights! Thank you *Igor Buzuk*, *Minna Ramkull*, *Emelie Niléhn*, *Ida Scherman*, *Ceciia Bille*, *Charlotta Åberg*, and *Elizabeth Zhang*, for always offering valuable support in administration work and technical issues. Thank you *Sven-Inge Möller* and *Göran Frank* for taking care of the ISP updates. Thank you *Adrian Roth*, *Emma Axebrink*, *Sabrina Gericke*, *Vladimir Alekseev*, *Zhiyong Wu*, *David Sanned*, *Megha Prakash*, *August Thomasson*, *Shubham Singh*, and *Jan-Peter Hannappel* for all the fun time in trivselgruppen activities. Thank you *Jundie Chen*, *Meena Raveesh*, *Megha Prakash*, *Kailun Zhang*, *Zhiyong Wu*, *Weilun Cheng*, *Jinguo Sun*, *Siyu Liu*, *Qi Qi*, *Lisa Rämisch*, *Saga Bergqvist*, *Christian Brackman*, and so many others for the happy lunches. There are so many to thank for all the fun time we spent after work.

I would also like to thank all my friends outside of work. You make my life colorful. I am lucky to have you with me to try so many new activities. Special thanks to my Wednesday, Friday, and Sunday badminton friends. With you, I progressed with mixed double, women's double, single, and even started a tournament! I really enjoyed the moment on the court with you. Thank you *Xin*, *Yupan*, *Jundie*, *Ruiyu*, *Huinan*, *Miao*, and *Leilei* for the help and fun activities. Thank you *Jing*, *Yu*, *Naxin*, *Zhaozhao*, and *Wei* for being so emotionally supportive. Thank you *Slyer*, *Xiuli*, *Yi*, *Meili*, and *Han* for all the support along with even though we are so far away. It is hard to imagine that I have known you for so long. And thank you *Walden* for having me here for my first two years. I wish you happiness in your life.

Last but not least, I would like to express my deepest gratitude to my *mom*, *dad*, *grandma*, and my *sister*. Your unwavering financial and mental support is my great treasure. You are the ones who hold and stand by me for whatever decision I make. You are too shy to express your love and kindness in words, but I totally feel it through your actions. I am lucky to have you.

Popular summary in English

Combustion has been existing for a long time in human life to provide heat and power. Most of the energy supply relies on the combustion of traditional fossil fuels, which refer to coal, oil, and natural gas. They also account for a great portion of the most concerned CO_2 emission, and it is just the process of generating CO_2 from carbon that releases the energy we need. Facing this, researches on renewable energy sources such as solar and wind power comes to the stage. One challenge in utilizing these intermittent energy sources lies in energy storage and transportation. This thesis intends to explore the potential of metal powders as renewable energy carriers. The metal powders can be burned to provide heat and energy whenever and wherever needed. The products, solid metal oxides, are then transported to places where renewable energy sources are abundant and available to be reduced back to metal powder. This loop is conceptualized as a "metal-fuel cycle".

The combustion of metal powder is an important part of this loop. Although burning metals to provide heat and power sounds new to us, the burning process itself has been around in our lives. Recalling the beautiful colors from the "flame test" experiments in chemistry classes, you would probably be amazed at the green color from burning copper, the yellow from sodium, etc. This metal property also inspires the creation of beautiful and cheerful fireworks in celebrations. Metal fuel can provide with us more than beauty. They can also be favored for civilian power and heat production. They are not carbon-based. They have quite high energy densities. They have abundant resources on Earth. They can be collected and recycled. Moreover, there have already been prototypes of metal powder burners set up in the Netherlands for brewery production and district house heating.

Encouraged by its potential applications, this thesis intends to deepen the understanding of the combustion kinetics and modeling of metal powder combustion with self-designed modeling tools. Iron (Fe) and Aluminum (Al) are considered as case studies. We will start with the different combustion modes to understand the dominant process in metal particle combustion, e.g., surface reaction dominated or vapor phase reaction dominated. Then we will introduce the phase diagram which helps distinguish a metal's combustion mode from information of different morphologies and their transition temperatures.

A general metal oxidation scheme considers different steps of oxidations in solid, liquid, and gaseous phases as well as the phase transition in between. Two numerical models based on different scales are developed to quantitatively characterize the metal particle burning scheme. Characteristic parameters for study include the burning time, the temperature, and species compositions. Collaborative experimental works have also been performed facilitating model validation. For metals featuring surface reaction dominated combustion mode, a metal "Point particle model" is designed to track the position and movement of the burning particles, where the temperature and composition evolution are also predicted.

This information helps us to quantify how much heat the metal particle can produce and how quickly it can burn. For the metal featuring vapor phase combustion mode, another "Boundary layer resolved model" is designed to resolve the surrounding gas phase and the flame structure of the particle. The metal point particle model focuses more on the particle, while the Boundary layer resolved model focuses more on the gas phase region surrounding the particle. Agreeable simulation results compared with experimental observations have been found for both models, and further model improvements are identified. Besides, this thesis also takes one step further to look at the Al gas phase kinetics based on the designed "Boundary layer resolved" model. Different sources of reaction rates are analyzed and compared in a "real-case" model for the first time, offering some guidance for future kinetic optimization and simulations.

The next time we enjoy the new year fireworks show, we probably can appreciate the science behind its beauty and cheerfulness. We hope that this thesis can provide readers with new foundational insights as well as some analyzing models to understand the combustion kinetics of single metal particles. This research on single metal particles marks just the beginning of an exploration into metal fuel combustion. Through this, we hope to pave the way for future applications in metal particle cloud combustion experiments and simulations in burners.

科普性概述

人类很早就开始利用燃烧提供热量和动力。当前，能源供应仍主要依赖传统化石燃料的燃烧，如煤炭、石油和天然气。这些化石燃料将碳转化为二氧化碳的过程是其释放能量的核心机制，但同时也导致了大量的二氧化碳排放。面对这一困境，对太阳能和风能等可再生能源的研究开始兴起。然而，这些可再生能源的能量生产具有间歇性特点，这使得高效的能源储存和运输面临着挑战。我的博士课题旨在探索一种新的移动式可长距离运输的储能方式—“金属颗粒燃烧”。你可以想象金属颗粒像煤炭一样被输送到燃烧炉燃烧提供热量和动力；燃烧生成的固态金属氧化物被回收运送到可再生能源丰富的地区，再通过还原反应转化为金属颗粒实现循环。这个概念被称为“金属燃料循环”。

金属颗粒的燃烧是“金属燃料循环”中的关键一环。尽管燃烧金属来提供热量和动力对我们而言是一个新颖的概念，但金属燃烧本身我们并不陌生。还记得化学课堂上的“焰色反应”实验吗？不同金属燃烧呈现出不同的颜色，绿色的铜火焰，黄色的钠火焰等等。以及你一定喜欢节日里绚丽多彩的烟花，它给我们留下美好珍贵的记忆。在能源与动力领域，金属作为一种燃料它无碳排放、高能量密度、有丰富的资源储量和良好的回收利用性。在荷兰已有金属燃烧炉试运营于啤酒厂生产和居民住房的区域供暖。

具体而言，我的博士课题研究金属颗粒的燃烧机理并在此基础上构建出不同尺度下的仿真模型。我首先介绍了金属颗粒燃烧中的不同主导模式，例如表面应主导或气相反应主导。它们可以通过相图来表征。相图还可以给出反应物、产物以及两者的平衡转化信息。我的论文以铁 (Fe) 颗粒和铝 (Al) 颗粒为具体研究对象构建了一个通用的金属颗粒氧化机制。两者中铁的燃烧主要由表面反应主导，而铝的燃烧主要由气相反应主导。这个通用的金属颗粒氧化模型涵盖了固态氧化、融化、液态氧化、蒸发、气相反应和凝固/凝结过程。在此基础上，我在博士课题中构建了两个仿真模型：“金属粒子追踪模型”和“边界解析模型”。金属粒子追踪模型可用来追踪颗粒的移动和反应，量化金属颗粒燃烧中的放热、燃烧速率和组分变化等信息。边界解析模型可用于解析燃烧的颗粒周围的火焰结构。前者的研究重心在粒子本身，而后者更关注颗粒周围的气体及火焰。通过与实验观测数据的对比验证，两种模型均表现出较好的合理性与可靠性。此外，我还进一步利用边界解析模型对铝的气相反应机理进行综述研究，以探究气相反应中的组分变化和放热性能。这些燃烧机理和模型的研究是我们利用好金属燃料的基础。

当你下一次欣赏新年的烟花表演时，或许可以联想到这篇论文中描述的复杂燃烧机理而从一个科学的角度来感受烟花背后的美丽。希望我的论文能够帮助你理解金属颗粒燃烧和了解目前的仿真模型研究。单个的金属颗粒研究仅仅是探索金属燃料应用于能源与动力领域的起点，以为后续研究燃烧炉内金属颗粒群燃烧打下基础。

Abstract

Metal fuels can be promising candidates as alternative energy sources and renewable energy carriers within the metal-fuel cycle. They feature high energy density, low environmental impact, and broad production and application. One challenge in metal particle combustion lies in its multi-physics complexity compared to traditional hydrocarbon fuels. This thesis intends to investigate the combustion physics of a single Iron (Fe) or Aluminum (Al) particle with currently available and self-designed modeling tools.

One novelty of this thesis is the construction of a generalized single metal particle combustion scheme, including sub-stages of solid-phase oxidation, melting, liquid-phase oxidation, evaporation, gas-phase oxidation, and solidification/condensation. Relevant reactants and products are identified for each sub-stage, and the kinetic rate is quantified. The constructed combustion scheme can characterize the vapor phase reaction dominated Al combustion and the heterogeneous surface reaction dominated Fe combustion.

Another novelty is the proposal of two models based on the OpenFOAM-7 platform: the metal "Point particle model" within the Lagrangian-Eulerian framework and the "Boundary layer resolved model" within the Eulerian framework, from different aspects of the above-generalized combustion scheme. The metal "Point particle model" intends to capture the whole combustion process of single Fe / Al particles. For Fe modeling, the predicted temperature evolution of a single Fe particle shows a similar trend to the experimental radiant intensity curve. The proposed conjecture of "super-cooled solidification" explains the experimentally observed radiant intensity jump. For Al, a "Melt-Ejection-Model"(MEM) is proposed to explain the observed pre-ignition phenomenon. The simulated Ignition Delay Time (IDT) statistically correlates well with experimental data. The detailed flame structure of a micron-sized Al droplet in hot steam-dominated environments is simulated with the "Boundary layer resolved model". Good agreement with experiment data is observed in the flame temperature for all the droplet sizes, and in the flame stand-off ratio and the Stefan flow velocity for the small droplet size group. Lastly, this thesis provides the first comprehensive review and analysis of Al / O_2 / H_2O gas-phase combustion kinetics in a "real-case" droplet combustion simulation based on the "Boundary layer resolved model".

It is hoped that this thesis can provide new foundational insights as well as some analyzing models for readers interested in the combustion kinetics and modeling of single metal particles.

Nomenclature

Abbreviations

Al	Aluminum
CFD	Computational Fluid Dynamics
DFT	Density Functional Theory
Fe	Iron
HAB	Height Above Burner
IDT	Ignition Delay Time
LPT	Lagrangian Particle Tracking
l.h.s	left hand side
r.h.s	right hand side
MEM	Melt Ejection Model
PDF	Probability Density Function
PTV	Particle Tracking Velocimetry
RPA	Reaction Pathway Analysis
RHR	Reaction Heat Release
RRKM	Rice Ramsperger Kassel Marcus
SEM	Scanning Electron Microscopy
TGA	Thermogravimetric Analysis
VTST	Variational Transition State Theory

Chapter 1

Introduction

1.1 Motivation

In compliance with the Paris Agreement, Sweden started a long-term climate act and policy in 2017 to commit to zero net greenhouse gas emissions by 2045 at the latest (1). Within the framework, the emission should be 63% lower than in 1990 by 2030, and 75% by 2045. In 2023, the emissions from the transport and energy sector were 18.4 Mt of CO_2 equivalents, accounting for ∼41.4% of the total emission that year (2). Combustion engines and power plants fueled with fossil fuels contribute a significant portion to the emissions. The pursuit for non-fossil energy sources (e.g., H_2 (3; 4), NH_3 (5; 6), and biofuel (7)) to replace the traditional hydrocarbon fossil fuel has become a prominent topic in the combustion research field. Another research focus is the exploration of a potential medium for renewable energy storage and transport (8; 9; 10). Metal fuels can be an appropriate candidate both in terms of transportation fuels and as renewable energy carriers due to their agreeable performance regarding energy output and emission control.

Metal fuels feature non-carbon-based, which eliminates CO_2 emission at the fuel source. They also feature high energy density and abundant resources. Metal fuels, when burned, release a significant amount of heat. The energy density of most metals, e.g., Al (∼84 MJ/L) and Fe (∼61 MJ/L), is equivalent or even higher than that of diesel (∼35 MJ/L) (8). This facilitates the potential transition from diesel to metal powders in normal internal combustion engines without losing the output power. Aluminum (Al) and Iron (Fe) are the two most abundant metal elements in the earth's crust, and they are widely mined and applied in industrial constructions (11). More attractively, the concept of the metal-fuel cycle, as proposed by Bergthorson *et al.* (9), offers a solution to mitigate the geographical gap between energy production and energy consumption. The metal particles can be trans-

ported to places with high energy demand, where they are burned to release the chemical energy. The combustion product, metal oxides, is then transported back to places with abundant renewable energy, e.g., wind and solar, which can be used for the reduction of the metal oxides. In this way, the metal particles serve as clean-energy carriers. With dense energy, abundance in production, recyclability with clean energy, and low environmental impact, the metal-fuel cycle seems to be a promising alternative for a CO_2-neutral society.

The Fe-fuel cycle has been researched in universities and institutions in, for example, the Netherlands and Germany (12; 13). Iron is of special interest in this metal-fuel cycle because of the convenience of retrofitting an existing production infrastructure and transportation network. Considering its fuel characteristics, iron can, in theory, replace coal in existing power plants, requiring limited modifications for retrofitting, e.g., to adopt higher particle loading, air/particle separation, and post-combustion particle collection (9). In the Netherlands, there have already been demonstrations of applying an iron-fuel combustor at brewery Bavaria (14) and an industrial prototype test of providing sustainable heating to 500 houses with an iron-fuel boiler (15).

The Al-fuel cycle has also been proposed with an intention for simultaneous hydrogen and power production when the oxidizer is water (8). There have been combustor tests of the reactor prototypes both for Al-water system (16) and the Al-steam systems (17) but not to a large scale as that of Fe. One challenge of Al oxidation is the passivating layer of the dense alumina oxide. Although Al is a quite active type of metal, the existence of this oxide layer prohibits Al from further reacting with oxidizers. The advance of technologies on how to modify or break the passivating layer facilitates further application of the Al-fuel cycle.

The metal research lab here at Lund University has contributed to the investigation of both the Fe-fuel cycle and the Al-fuel cycle for the past few years, supported by the Knut and Alice Wallenberg Foundation for exploring CO2-neutral energy conversion using advanced laser diagnostics and modeling (18). Joint efforts of experiments, kinetics, and modeling are employed to deepen the understanding of single metal particle combustion. Experiments have been performed by the collaborators both on the single particle tracking (19; 20) and the resolved droplet flame structure (21; 22; 23), together with some preliminary investigation of particle dust cloud combustion (24; 25). These experimental data offer valuable information for constructing a general metal particle combustion model and its application in Computational Fluid Dynamics (CFD) simulations.

Within that project framework, this thesis focuses on the kinetic and modeling aspects based on the measured experimental data. A general combustion scheme for single metal particles is illustrated, taking Fe and Al as case studies. Metal particle combustion differs from traditional hydrocarbon fuel combustion in that multi-physics complexity is involved. Phase changes occur between solid, liquid, and gas states. Different combustion modes can also occur, either in the gas phase or at the particle surface. Thus, different sub-

models are needed to characterize the whole combustion process. This thesis proposes two models to address different aspects of the general combustion scheme: the metal "Point particle model" within the Lagrangian-Eulerian framework and the "Boundary layer resolved model" within the Eulerian framework. Apart from those, for the gas phase reactions, this thesis presents a comprehensive review and analysis of the Al gas phase kinetics, with an intention to extend the kinetic analysis method on conventional hydrocarbon fuels to this type of new fuel.

1.2 Background

Metal combustion has been explored dating back to 1960s (26) when metals were widely utilized in high temperature and corrosive environments, as well as increasing interest in metal powders as fuel additives for rocket and jet engine propulsion. Different from conventional fuel, metal burning mostly features the formation of condensed-phase products, which introduces complex multi-phase physics into the combustion system. The existence of heterogeneous reactions leads to a more varied combustion mode, which needs to be clarified before we dig into the physiochemical details of the single metal particle combustion.

The "combustion modes" can refer to the fact that: 1) based on a spatial scale, chemical reactions can occur in the vapor phase or heterogeneously at the particle surface, and 2) based on a temporal scale, the process can be dominated either by chemical kinetics or molecular diffusion. To distinguish between different modes, Fig. 1.1 qualitatively describes the normalized temperature and species mole fraction distribution in the surroundings of a droplet.

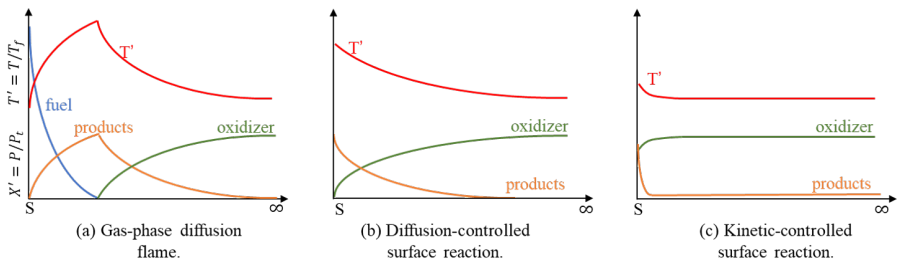

Figure 1.1: Illustration of the normalized temperature and species mole fraction distribution under different combustion modes: (a) gas-phase diffusion flame; (b) diffusion-controlled surface reaction; (c) kinetic-controlled surface reaction. The horizontal axis denotes the distance from the droplet surface marked as "S" in the coordinate origin.

In the vapor phase diffusion flame combustion mode (Fig. 1.1(a)), combustion occurs as a diffusion flame surrounding the particle. The temperature peaks some distance away from the surface and is generally considered to be limited by its metal oxide's vaporization/dissociation temperature due to the endothermic nature of the vaporization/dissociation

process. The particle temperature is close to its boiling temperature. In the surface combustion modes (Figs. 1.1(b)–(c)), the fuel is usually in the condensed phase and does not diffuse outwards. The chemical reactions occur quite close to or at the surface, and the flame temperature is close to the particle temperature. The products can exist in either the condensed phase or the gas phase. In the latter case, they diffuse outward.

The classical "Glassman's criteria" (26; 27) is well known for classifying vapor phase and surface combustion modes of different metals by their respective thermodynamic properties. For metal oxides, it is difficult to define a "boiling point", as many metal oxides vaporize/decompose to sub-oxides instead of forming the gaseous original metallic oxides. The metal flame temperature is considered to be limited by this vaporization/decomposition temperature in that the metal combustion heat is insufficient to sustain further vaporization/dissociation of the metal oxide product. This vaporization/decomposition temperature is also termed the "boiling point" of the metal oxides in the metal combustion field, although it is not a true "boiling" point in common sense. "Glassman's criteria" states that for a metal to burn in the vapor phase, the metal flame temperature, i.e., the oxide's "boiling" temperature, should be higher than the boiling temperature of the metal. Otherwise, combustion proceeds heterogeneously on the particle surface.

Set against this, Fe has a boiling temperature of 3133 K, and the currently available Fe-oxide decomposition temperature is ∼1730 K (Table 1.1). This indicates that Fe typically burns in the surface reaction mode. On the contrary, Al has a boiling temperature of ∼2790 K and its oxides, alumina, has a dissociation temperature of ∼4000 K (Table 1.2), which indicates that Al typically burns in the vapor phase shown as a detached condensation layer wrapping the particle. This idea of different combustion modes was later adopted by many experimental and modeling works for Fe (28; 29; 30) and Al (31; 32; 33; 34).

It should be noted that although metals mainly follow the above criteria, later studies on closer visualization of the single metal droplet do reveal some signs of vapor phase combustion for Fe and heterogeneous surface reaction for Al. A distinct reddish tail around the particle was spotted (35) and further visualized in detail (19) in the burning intensity of single Fe particles. Ning *et al.* (36) measured the critical temperature for nanoparticle cloud formation to be ∼2100 K. For Al particle combustion, Dreizin *et al.* (37) found Al-O solutions formed inside the burning aluminum particle from the cross-section of the quenched burning particle, revealing the occurrence of internal phase change of the burning particle due to heterogeneous Al/O_2 reactions at the surface. A transition from vapor phase combustion to surface combustion was observed in the shock tube experiment by Bazyn *et al.* (38) and predicted by Mohan *et al.* (39). In correspondence with this experimental finding, Glorian *et al.* (40) included a surface reaction subset in their model where absorption of H on the surface with formation of OH, H and AlH were considered.

The other aspect of the different combustion modes is on a temporal scale, where diffusion-

controlled or kinetic-controlled combustion can dominate depending on their rates. For droplet combustion, this distinction mainly occurs in the surface reaction mode (Fig. 1.1(b,c)). In a diffusion-controlled case (Fig. 1.1(b)), the diffusion of reactants and products is slower than the reaction rate, resulting in a spatial non-uniformity due to the concentration gradient, whereas in a kinetic-controlled case (Fig. 1.1(c)), the reaction rate is slower than the diffusion rate.

To distinguish between the kinetic-controlled mode and the diffusion-controlled mode, the time scales can be compared. In a kinetic-controlled surface reaction mode, the burning time can be written as (41)

$$t_{b,kin} = \frac{\rho_p d_0}{2W_p k P X_{O,\infty}}, \tag{1.1}$$

where ρ_p is the particle density; d_0 is the particle initial diameter; W_p is the molecular weight; k is the surface reaction rate; P is the oxidizing pressure; $X_{O,\infty}$ is the oxidizer mole fraction in the surrounding.

On the other hand, in a diffusion-controlled surface reaction mode, the combustion time is written as

$$t_{b,diff,g} = \frac{\rho_p d_0^2}{8\rho_g D_g ln(1+\xi Y_{O,\infty})}, \tag{1.2}$$

where ρ_g is the gas density; D_g is the gas diffusivity; ξ is the stoichiometric fuel-oxidizer mass ratio; $Y_{O,\infty}$ is the oxidizer mass fraction in the surrounding.

Sundaram *et al.* (42) also included a combustion time scale when diffusion inside the particle is dominant:

$$t_{b,diff,c} = \frac{d_0^2}{24 D_p}, \tag{1.3}$$

where D_p is the mass diffusion coefficient in the particle.

With these, a Damköhler number, D_a, given as the ratio of diffusion time scale to the reaction time scale, is introduced (41),

$$D_a = \frac{t_{b,diff,g,c}}{t_{b,kin}} = \frac{4\rho_g D_g ln(1+iY_{O,\infty})}{W_p k P X_{O,\infty}}. \tag{1.4}$$

$D_a < 1$ means the reaction rate is slower than the diffusion rate, thus a kinetic-controlled mode featuring Fig. 1.1(c). $D_a > 1$ means a diffusion-controlled mode featuring Fig. 1.1(b). Many experimental studies tried to identify the kinetic-controlled/diffusion-controlled mode in Al combustion on a more general level by correlating the global combustion time dependence on the particle diameter, oxidizer composition, and pressure conditions (38). In the diffusion-controlled mode, the combustion time is quadratically dependent on particle

size and independent of pressure. In contrast, in the kinetic-controlled mode, the combustion time is proportional to particle size and decreases with increasing pressure. Meanwhile, larger particles and higher pressure tend to lead to diffusion-controlled combustion. Both Fe and Al single particles feature the diffusion-controlled combustion mode.

The multi-phase metal oxidation reactants and products can be characterized by the phase diagram, where the different structures and compositions of the metal and its oxides are shown. The transitions between different phases and their characteristic equilibrium temperatures are also indicated in the phase diagram.

Figure 1.2 shows the Fe-O phase system. Solid state Fe structures include αFe, γFe, and δFe, where the transitions occur at ~912 °C and 1392 °C in sequence. Melting of the solid Fe occurs at ~1528 °C (~1800 K) with δFe $\rightleftharpoons$ L_1. L_1 denotes the Fe-rich liquids, in which the oxygen content can vary depending on the equilibrium temperature, shown as the boundary line between L_1 and the $L_1 + L_2$ mixture.

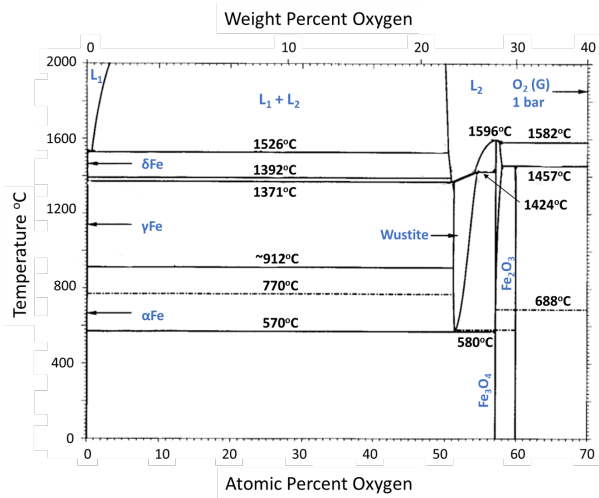

Figure 1.2: The Fe-O phase diagram. Adapted from Wriedt (43). Wustite can have a FeOx composition with x varying from 51.2% to 54.6%, depending on the equilibrium temperature. In this work, Wustite is simplified as FeO. L_1 denotes the Fe-rich liquids, and L_2 denotes the O-rich liquids. Note that the atomic O% in both L1 and L2 can vary depending on the equilibrium temperature.

Table 1.1: The melting, boiling, and decomposition temperatures, and the latent heat of fusion for Fe and Fe oxides. Data sources: (43; 44)

	Melting Temp. T_m [K]	Decomposition Temp. T_{decomp} [K]	Boiling Temp. T_b [K]	Latent heat of fusion H_f [kJ/kg]
Fe	1810	-	3133	247
FeO	1650	-	-	335
Fe_3O_4	1870	-	-	540
Fe_2O_3	-	1730	-	596

Iron oxides have three stable structures in the solid phase depending on the oxygen content, namely FeO (wustite), Fe_3O_4 (magnetite), and Fe_2O_3 (hematite). Note that the oxygen content can vary to some degree from the stoichiometric mixture composition. In the liquid phase, iron oxides appear as O-rich liquids denoted as L_2, which have a broad range of oxygen content depending on the equilibrium temperature. This indicates that the melting of Fe oxides can be incongruent, and it is difficult to specify a melting point for an individual Fe-oxide. For FeO, the phase diagram suggests a eutectic reaction of $L_2 \rightleftharpoons \gamma Fe + FeO$ at ~1650 K. For Fe_3O_4, a congruent melting occurs at a temperature of ~1870 K, while a eutectic type transition between Fe_3O_4 and L_2 occurs at ~1870 K. For Fe_2O_3, instead of melting, it has a decomposition reaction via $Fe_2O_3 \rightleftharpoons Fe_3O_4 + O_2$ at a temperature of ~1730 K. To simplify the modeling in this work, the complex reactions reflected from the phase diagram are not considered in detail. Instead, the typical temperature points, as well as the latent heat of fusion of Fe and Fe oxides, from the Janaf database listed in Table 1.1 are adopted.

Compared with Fe, the Al-O phase diagram is simpler, as shown in Fig. 1.3. Stable structures are Al and αAl_2O_3 in the solid phase, and L_1 and L_2 in the liquid phase. The melting of Al and αAl_2O_3 occurs at ~933 and 2327 K, respectively. Fig. 1.3 also includes the gas phase, where a gas mixture of Al, AlO, AlO_2, Al_2O, Al_2O_2, O, O_2 and O_3 is considered. The system reaches a three-phase equilibrium state at ~2485 K, wherein L_1, L_2, and gas co-exist. The phase diagram also reveals that L_2 decomposes at ~4000 K into the gas mixture. Typical temperature points, as well as the latent heat of fusion of Al and Al oxides, are listed in Table 1.2.

Table 1.2: The melting, boiling, and decomposition temperatures, and the latent heat of fusion of Al and αAl_2O_3. Data sources: (44; 45)

	Melting Temp. T_m [K]	Boiling Temp. T_b [K]	Decomposition Temp. T_{decomp} [K]	Latent heat of fusion H_f [kJ/kg]
Al	933	2790	-	397
αAl_2O_3	2327	-	~4000	1090

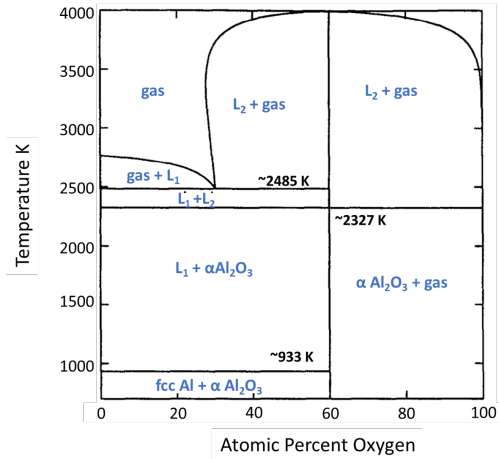

Figure 1.3: The Al-O phase diagram. Adapted from Taylor *et al.* (45). L_1 and L_2 refer to the Al-rich and Al_2O_3-rich liquids, respectively. In the original figure, "Corundum" is adopted instead of αAl_2O_3.

1.3 Research questions and thesis scope

Starting with knowledge of traditional hydrocarbon combustion and a preliminary understanding of the multi-physics involved in metal particle combustion, this thesis intends to deepen the knowledge of metal particle combustion using currently available and self-designed modeling tools. The following research questions are outlined and addressed:

- Development of a generalized model for multi-physics involved metal particle combustion. This thesis divides the process into six sub-stages, i.e., solid-phase oxidation, melting, liquid-phase oxidation, evaporation, gas-phase oxidation, and solidification/condensation. The main reactants and products at each stage are identified, and the kinetic rate is quantified. Governing equations for each sub-stage are listed. The metal "Point particle model" for Fe and Al is constructed based on this general combustion scheme, with emphasis on different sub-stages for different metals. The model is also validated against the experimental data provided by the collaborators.

- Characterization and modeling of vapor flame structure and chemistry for metals featuring vapor phase combustion mode. This thesis proposed a "Boundary layer resolve model" for Al particle combustion, based on which flame temperature and stand-off ratio are predicted and also evaluated against the experimental data provided by the collaborators. The proposed model is further utilized for a comprehensive analysis of Al gas-phase kinetics in oxygen and steam environments.

- Improved understanding and enhanced modeling of extraordinary phenomena observed in experiments, e.g., the radiant intensity jump for the Fe particle combustion

and the eggshell morphology for the Al particle combustion. Based on the "Point particle model", this thesis incorporated conjectured mechanisms and verified them with experimental data.

This thesis focuses on studying combustion kinetics and modeling of micron-sized single Fe and Al particle combustion in hot oxidizers. In real applications, particle cloud combustion is more common where both the individual particle combustion performance and the particle-particle interaction are important. Currently, this thesis only addresses single particle combustion as a starting point. The oxidizer condition of interest is for high-temperature oxygen or steam. Therefore, the low-temperature oxidation, e.g., the diffusion of ions through the oxide layers, is not treated extensively. Moreover, only Fe and Al are studied, while there are other metals, such as B, featuring a different combustion mode. Although the proposed general metal combustion scheme includes most of the sub-stages during combustion, the detailed combustion scheme is case-specific. It should also be noted that the particle sizes in this thesis are limited to micron-sized scale. The combustion behavior at the nano-sized scale can differ significantly. Therefore, extending the current model to the nano-sized particle combustion should be cautious. It is hoped that this thesis can offer the key background knowledge from literature as well as some analyzing models for readers who are interested in the combustion kinetics of single micron-sized metal particles.

1.4 Thesis outline

This thesis is organized as follows:

- In **Chapter 2**, the modeling methodology is presented. The governing equations for the "Boundary layer resolved model" based on the Eulerian framework and the metal "Point particle model" based on the Lagrangian-Eulerian framework are listed. The Eulerian framework includes mainly the gas phase domain. The mass and heat exchange between the single particle and the surrounding gas is captured by the boundary condition. The Lagrangian-Eulerian framework includes both the particle phase and the gas phase with coupled mass and heat exchange. Based on the proposed model in the Eulerian framework, a mechanism analysis structure is also introduced as a guideline to examine the Al gas phase combustion mechanisms in the open literature.
- In **Chapter 3**, the different sub-stages in the general combustion scheme of single metal particle combustion are described, which is divided into solid-phase oxidation, melting, liquid-phase oxidation, evaporation, gas-phase oxidation, and solidification/condensation. The mathematical descriptions of the mass and heat change

rate for each sub-stage, as well as the choice of model parameters, are presented. Modeling of special phenomena such as intensity jump and ejection before ignition is also included.

- **Chapter 4** presents the modeling results together with experimental data for validation. This chapter is divided into four sections, including the metal "Point particle model" for the Fe particle, the metal "Point particle model" for the Al particle, the "Boundary layer resolved model" for the Al particle, and the analysis of Al gas phase combustion kinetics.
- **Chapter 5** provides thesis conclusions together with suggestions for future work.
- Lastly, the publications related to the thesis are included in the Appendix, followed by a summary of author contributions.

Chapter 2

Methodology

In this chapter, the methodology of modeling metal particle combustion in this thesis is presented. Two models, namely the metal "Boundary layer resolved model" within the Eulerian framework and the metal "Point particle model" within the Lagrangian-Eulerian framework, are proposed. The Eulerian framework treats the particles as boundaries of fluid and models the fluid flow using classical governing equations for fluid flow based on the conservation laws for mass, species, momentum, and energy. The flame structure in the vicinity of a burning droplet can be accurately resolved. The Lagrangian framework adopts the Lagrangian Particle Tracking (LPT) approach to track the motion of the particles and the rates of change of some conserved properties of the particles, e.g., mass and temperature, which are described by a set of mass, momentum, species, and enthalpy equations. The mass and heat exchange between the particle and the surrounidng fluid is realized by additional source terms to the governing equations of the Eulerian framework. With proper submodels, a general combustion scheme for a single metal particle with different stages can be characterized. Based on the "Boundary layer resolved model", the chemical kinetic mechanisms of metal vapor can be analyzed. This thesis also presents a comprehensive and detailed Al gas-phase chemical kinetic analysis. Detailed descriptions of the two models and the chemical kinetic analysis are given below.

2.1 Eulerian framework

The governing equations for mass, species, momentum, and energy are described as follows:

$$\frac{\partial \rho}{\partial t} + \nabla \cdot (\rho \vec{u}) = \dot{\omega}_p, \tag{2.1}$$

$$\frac{\partial \rho Y_i}{\partial t} + \nabla \cdot (\rho \vec{u} Y_i) - \nabla \cdot (\rho D_i \nabla Y_i) = \dot{\omega}_{g,i} + \dot{\omega}_{p,i}, \tag{2.2}$$

$$\frac{\partial \rho \vec{u}}{\partial t} + \nabla \cdot (\rho \vec{u} u) - \nabla \cdot \tau + \nabla p = \vec{F}_p, \tag{2.3}$$

$$\frac{\partial \rho h_s}{\partial t} + \nabla \cdot (\rho \vec{u} h_s) - \nabla \cdot (\rho \alpha \nabla h_s) = \dot{Q}_g + \dot{Q}_p, \tag{2.4}$$

where the subscript "p" represents source terms from the particles due to mass, momentum, and heat exchange with the gas phase. The subscript "g" stands for "gas"; ρ is the gas density; $\vec{u}$ is the gas velocity vector; Y_i is the mass fraction of species i in the gas mixture; D_i is the diffusion coefficient of species i in the gas; p is the gas pressure; τ is the viscous stress tensor of gas; h_s is the sensible enthalpy of the gas mixture; α is the thermal diffusion coefficient. $\dot{\omega}_{g,i}$ and $\dot{Q}_g$ depict the chemical reaction rate for species i and heat release rate due to gas phase reactions, respectively. They can be characterized by the implementation of a detailed gas phase mechanism.

For metal particles featuring vapor phase combustion dominated mode, the Eulerian framework can be applied to resolve the temperature and species profiles in the surroundings of the metal particle. Accordingly, a "Boundary layer resolved model" is developed. In this approach, the source terms with subscript "p" in the governing equations disappear since the particle/gas interaction is resolved using boundary interface exchange models.

A typical simulation domain to model the gas phase region is shown in Fig. 2.1. The region outlined with solid orange lines denotes a pseudo-1D computational domain approximating the symmetrical spherical surroundings. Along the radial direction, the *Fuel* boundary resides at the droplet surface, and the "Outlet" boundary is 40R away from the surface. Each cross-section is a square, with the side length being 0.0375R at the droplet surface and 1.5R at the furthest point. All the other faces are "symmetry".

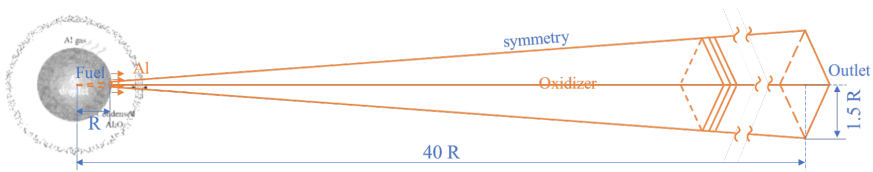

Figure 2.1: Illustration of the simulation domain modeling the gas phase region surrounding a single metal particle (Paper III).

At the *Fuel* boundary, some physio-chemical processes can lead to mass and heat transport between the particle and the gas domain. Such processes can include evaporation of the condensed phase (metal and its oxides), the deposition of gaseous species to the metal particle surface, and heterogeneous surface reaction on the metal particle surface. It is necessary to establish appropriate boundary conditions, especially for the *Fuel* boundary, to complete the model. The boundary condition involves the gas composition, temperature,

velocity, and pressure. As an initial model, only the evaporation process is currently considered at the *Fuel* side. The detailed equations will be addressed in Section. 3.4 where modeling of the evaporation process is discussed.

2.2 Lagrangian framework

The Lagrangian framework is usually coupled with the Eulerian framework to model the moving metal particle combustion process in the burner (46; 47). The LPT captures the particle phase, while the Eulerian framework describes the flow field. The mass and heat exchange between the two phases is also considered via additional source terms ($\dot{\omega}_p$, $\dot{\omega}_{p,i}$, $\vec{F}_p$, and $\dot{Q}_p$) to the governing Eqs. 2.1-2.4 within the Eulerian framework. Figure 2.2 shows a schematic Lagrangian-Eulerian framework considering different sub-models in the metal "Point particle model".

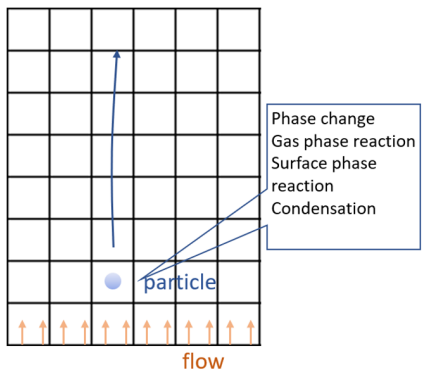

Figure 2.2: Illustration of the Lagrangian-Eulerian framework, as well as the different sub-models considered in the metal "Point particle model".

In the LPT, the particle position $\vec{x}_p$ is tracked via:

$$\frac{d\vec{x}_p}{dt} = \vec{u}_p. \tag{2.5}$$

The subscript p denotes the particle phase. $\vec{u}_p$ is the particle velocity calculated from the Newton's second law:

$$\frac{d\vec{u}_p}{dt} = \vec{f} + \vec{g}, \tag{2.6}$$

where $\vec{f}$ denotes the drag force and $\vec{g}$ is the gravity. The drag force can be explained as

$$\vec{f} = \frac{C_D \rho_g}{\tau_p \rho_p} \frac{Re_p}{24} \left(\vec{u}_g - \vec{u}_p\right), \tag{2.7}$$

where $\vec{u}$ is the velocity and ρ is the density. The subscripts p and g denote particle and gas phases, respectively. Re_p is the particle Reynolds number calculated as $Re_p = |\vec{u}_g - \vec{u}_p|d_p/\nu$. C_D is the drag coefficient modeled as

$$C_D = \frac{24}{Re_p}(1 + \frac{1}{6}Re_p^{2/3}) \tag{2.8}$$

for $Re_p \leqslant 1000$ (48). $\tau_p = d_p^2/18\nu$ is the characteristic time of the particle, in which ν is kinematic viscosity and d_p is the particle diameter. Re_p is the particle Reynolds number calculated as $Re_p = |\vec{u}_g - \vec{u}_p|d_p/\nu$.

Apart from particle movement, the evolution of particle mass and temperature is also modeled through a series of sub-models, including the oxidation sub-models in solid, liquid, and gas phases, and the phase change processes in between. Some other special phenomena, such as metal particle early ignition due to ejection are also incorporated in the Lagrangian framework. Detailed modeling equations will be presented in Chapter 3.

Heat transfer ($\dot{H}_{ht}$) between the particle and the surrounding gas includes mainly radiation ($\dot{H}_r$) and convection ($\dot{H}_c$). The radiation is modeled as

$$\dot{H}_r = A_p\sigma\epsilon(T_p^4 - T_g^4), \tag{2.9}$$

where A_p is the particle surface area. T_p and T_g are particle and gas temperatures, respectively. σ is the Stefan-Boltzmann constant and ϵ is the emissivity.

The convection is determined as

$$\dot{H}_c = A_p\frac{Nu\lambda_f}{d_p}(T_p - T_g), \tag{2.10}$$

where λ_f and Nu are the film layer thermal conductivity and the Nusselt number, respectively. It is worth noting that, for micron-sized metal particles modeled in this work, the maximum particle Biot number is ~0.002, which is much smaller than 0.1. Therefore, a uniform particle temperature T_p is assumed inside the particle and on the surface, similar to that in Ref. (49). The Nusselt number (Nu) and the Sherwood number (Sh) are estimated using the Ranz-Marshall correlation (50):

$$\mathrm{Nu} = 2 + 0.6\mathrm{Re}_p^{\frac{1}{2}}\mathrm{Pr}^{\frac{1}{3}}, \tag{2.11}$$

$$\mathrm{Sh} = 2 + 0.6\mathrm{Re}_p^{\frac{1}{2}}\mathrm{Sc}^{\frac{1}{3}}, \tag{2.12}$$

wherein Pr is the Prandtl number calculated from ν/α, and Sc is the Schmidt number calculated from ν/D. Detailed transport properties are calculated at a film temperature, T_f, using the 1/2 law (51), i.e., $T_f = (T_p + T_g)/2$. Additionally, if the particle condensed

phase were to be coupled with the gas phase, source terms of total particle mass change rate ($\dot{\omega}_p$), mass change rate of composition i in the particle ($\dot{\omega}_{p,i}$), viscosity force exerted by the particle movement ($\vec{F}_p$), and heat release source from the particle ($\dot{Q}_p$) would need to be added to the governing gas phase equations of mass, species, momentum, and energy mentioned in the previous section "Eulerian framework".

2.3 Chemical kinetic mechanism analysis

For metal particles featuring vapor phase combustion modes, vapor combustion kinetics is important in predicting the temperature and species concentration in CFD simulations. One typical example is Al combustion. There are many available Al gas phase combustion mechanisms in literature based on both experimental and theoretical studies of the reaction rate constants. This thesis performs a comprehensive review and analysis of the different sources of gas phase kinetic mechanisms following the structure described in this section. It should be noted that this general analysis structure can be extended to other metals featuring vapor phase combustion mode as well.

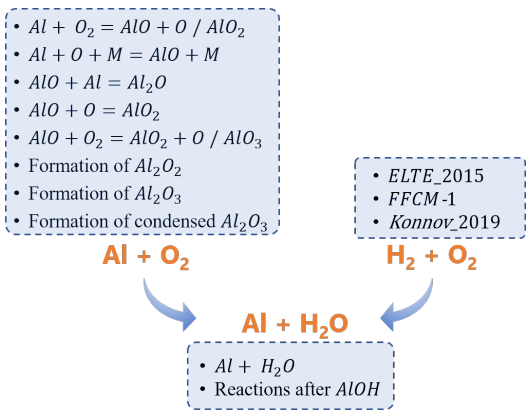

Figure 2.3: Schematic overview of the three subsets in the $Al/O_2/H_2O$ mechanism. The reactions/mechanisms listed within each subset are those of interest in this work and do not represent the complete set of reactions.

A generalized $Al/O_2/H_2O$ mechanism structure is plotted in Fig. 2.3, which can be divided into three subsets: Al/O_2, Al/H_2O, and H_2/O_2 subsets. The selected reactions for analysis are outlined in the box of each subset in Fig. 2.3. The reactions include those with currently available measured rate constant data, and those with significantly different rate constants from various mechanisms. The Al/O_2 subset contains only two elements Al and O, with reactions involving the initiation reactions of $Al + O_2$ and $Al + O + M$, the reactions regarding AlO, the formation of Al_2O_2, Al_2O_3, and the formation of condensed Al_2O_3. The Al/H_2O subset is more complicated due to additional Al / H / O sub-oxides. Considering the scarcity of experimental data, only the initialization reaction $Al + H_2O$ is examined in

this work. Nevertheless, a general description of different reaction paths after the initiation reaction is presented. The H_2 / O_2 subset lays the foundation of the Al / H_2O gas phase mechanism. There have already been many detailed H_2 / O_2 mechanisms published as well as reviews of their performance (52; 53); however, most of the Al mechanisms adopt a compact H_2 / O_2 subset with ~20 reactions. To validate the accuracy of the simplified H_2 / O_2 subset, their performance is compared against several popular detailed mechanisms, including the ELTE_2015 (54), the FFCM-1 (55), and the Konnov_2019 (56) mechanisms.

Mechanism analysis is performed on both an elementary reaction level and a global mechanism level. On an elementary reaction level, the rate constants of the elementary reactions of interest are reviewed. For some reactions, a specific backward reaction is presented in different mechanism sets. To facilitate comparison, the reverse rate constant is calculated based on the forward rate constant and thermodynamic data of the species involved using the Mechanism Analyzer module in Chemkin PRO 2020R2 (57).

On a global mechanism level, mechanism evaluation is conducted by implementing different mechanisms in the CFD simulation of a burning droplet to compare the predicted temperature and species profiles. A Boundary layer resolved model, as described in the previous "Eulerian framework" section, is adopted. For Al, the modeling is set for both the air oxidizer and the steam oxidizer cases based on the respective experimental conditions, as listed in Table 2.1. For the air case, the experimental condition of Bucher *et al.* (31; 32) is modeled with the oxidizer being air at 300 K and 1 atm, and a droplet surface temperature being ~2400 K. For the steam case, a similar condition to the experiment of Wu *et al.* (22; 23) is modeled with the oxidizer being pure H_2O at 2600 K and a droplet surface temperature of 2650 K.

Table 2.1: Experimental conditions for simulation in Al mechanism validation

Case	Particle surface Temp. T_p [K]	Surrounding Temp. T_a [K]	Surrounding oxidizer mass fractions	Refs.
air	2400	300	$0.233O_2 + 0.767N_2$	(31; 32)
steam	2650	2600	H_2O	(23)

To further exclude the diffusion effects and examine the chemical kinetics, simulations are performed with the 0-D homogeneous batch reactor in Chemkin PRO 2020R2 (57). With that, the temporal evolution of the temperature and critical species concentrations can be calculated, and the main reaction pathways can be identified. For Al, the 0-D homogeneous batch reactor simulation is set at an initial condition of a high temperature to enable the generation of Al vapor (2500 K) and of 1 atm with a stoichiometric mixture of Al/air and Al/H_2O, respectively. The main reaction pathways are analyzed at a time point when 50% of the Al is consumed. Kindly note that all the analyses mentioned in this section, including the reaction rate analysis, the boundary layer resolved model simulation, and the 0-D homogeneous batch reactor simulation, are intended for combustion conditions of

interest, i.e., at atmospheric pressure and a temperature range of 1000–5000 K.

Only part of the analysis results are selected and presented in Section 4.4, including the evaluation on the global mechanism level in the air and the steam case and a reaction pathway analysis in the steam case. Readers can refer to Papers IV and V for more detailed results and analysis.

Chapter 3

Modeling the physio-chemical processes in metal particle combustion

In this chapter, the general physio-chemical processes in metal particle combustion are presented following a series of sub-stages, including solid-phase oxidation, melting, liquid-phase oxidation, evaporation, gas-phase oxidation, and solidification/condensation. Two models, namely the "Boundary layer resolved model" within the Eulerian framework and the "Point particle model" within the Lagrangian-Eulerian framework, are proposed. The "Boundary layer resolved model" discussed in this work covers only the evaporation, gas-phase oxidation, and condensation/solidification stages, while the metal "Point particle model" contains all the mentioned sub-stages. The discussions will include both Fe and Al particles. Note that the solid-phase and liquid-phase oxidation for Al in both models are only described here but have not been implemented as a preliminary investigation. This is also mentioned in the Future work in Chapter 5. Detailed mathematical descriptions within each model for different sub-stages are given below.

3.1 Solid phase oxidation

Most oxidation kinetic studies focus on the iso-thermal condition based on the Thermogravimetric Analysis (TGA) method. The iso-thermal condition ensures enough time for the system to reach thermal equilibrium. Also, the oxygen partial pressure is high enough to enable the oxidization reaction. This is referred to as "cold burning" (58). It is different from the combustion condition of interest in this work, where the reactant is heated at a fast rate, and the system is not iso-thermal. Therefore, before the kinetic rate is discussed, direct applications of the measured oxidation kinetic parameters from TGA to combustion

modeling should be made with caution.

3.1.1 Fe

For Fe oxidation in the solid phase, a thin multi-layer structure of oxides produced on the iron surface was observed under high-temperature isothermal oxidation conditions (59; 60). The layer consists of wustite (FeO), magnetite (Fe_3O_4), and hematite (Fe_2O_3) in sequence, growing outward from the particle surface. The layer has a constant thickness ratio of ~95:4:1 within the temperature range of 973–1523 K (60). Considering the large proportion of wustite formed in the layer, a one-step global reaction is applied to describe the solid phase reaction:

$$\mathrm{Fe(s) + 0.5\,O_2(g) \longrightarrow FeO(s)} \tag{R1}$$

This oxidation is dominated by the diffusion of ions through the oxide layer (61) following a parabolic rate law, which quantifies the thickness increase or weight gain of the oxide layer over time. Raw Fe particle usually has an irregular and curved surface before melting. Thus, the weight gain equation is adopted to exclude the effects of surface curvature (62):

$$W^2 = K_p t + W_0^2, \quad K_p = K_\infty \exp(-Ea/RT_p), \tag{3.1}$$

where W is the weight gain per unit area (kg/m^2) with an initial value of W_0 = 0. K_p is the parabolic rate constant featuring an Arrhenius-like dependence on temperature. Ea = 157539 [J/mol] and K_∞= 304.7 [kg^2/(m^{4}s)], which are taken from Chen *et al.* (63).

The heat release rate during Fe solid phase oxidation is then given as

$$\dot{H}_{solid,\,Fe} = W \cdot A \cdot \xi \cdot \Delta H_{R1}/dt, \tag{3.2}$$

where ξ is the stoichiometric fuel-oxidizer mass ratio Fe/O; A is the apparent surface; ΔH_{R1} is the reaction heat [J/kg Fe] of R1; dt is the simulation time step.

3.1.2 Al

For Al oxidation in the solid phase, most studies are also based on TGA. A step-wise oxidation behavior with increasing temperature has been observed, where the oxide morphology evolves as amorphous$\rightarrow \gamma/\delta/\theta \rightarrow \alpha$–$Al_2O_3$ within a temperature range up to 1500 °C. The amorphous alumina layer is the natural oxide formed on the surface of Al at room temperature, with an initial thickness ranging 0.5–4 nm (64). The growth of this layer is slow and dominated by the outward diffusion of Al cations. It is thermodynamically stable only until a critical thickness of about 5 nm, after which the amorphous structure transitions into the partially crystallized γ-Al_2O_3. The growth of the γ-Al_2O_3 is dominated by

the inward diffusion of O anions and is accompanied by phase transformations into other transition polymorphs, e.g., δ-Al_2O_3 / θ-Al_2O_3. As temperature increases, the transition to the more stable and denser α-Al_2O_3 occurs at about 950–1250°C. The growth of the α-Al_2O_3 layer is also dominated by the inward diffusion of O anions, yet with a slower oxidation rate.

As per the Al-O phase diagram (Fig. 1.3), the stable structure for the Al oxide is α-Al_2O_3. The global reaction for Al oxidation is written as

$$Al(s) + 0.75\,O_2(g) \longrightarrow 0.5\,Al_2O_3(s) \tag{R2}$$

In correspondence with this oxidation scheme, Trunov *et al.* (64) developed a comprehensive model to characterize the simultaneous growth and phase transformation of different oxide structures. The governing equations will be presented in the following. The total oxidation rate is the sum of each morphology phase change process:

$$\dot{m}^{ox} = \sum_i \dot{m}_i^{ox}, \tag{3.3}$$

with $i = am$, γ, α denoting the amorphous, γ, and α-Al_2O_3, respectively. Only one alumina polymorph is allowed to grow at any given time. For each $\dot{m}_i^{ox}$, it is described by an Arrhenius-type expression

$$\dot{m}_i^{ox} = \frac{C_i\, exp(-Ea_i/RT_p)}{1/r_{i-1} - 1/r_i}, \tag{3.4}$$

where C_i is the diffusion coefficient; Ea_i is the activation energy; r_i and r_{i-1} are the particle radius; R is the universal gas constant. The subscripts i and $i-1$ indicate the specific oxide polymorph, i.e., amorphous, γ / α-Al_2O_3, with $i-1$ being the underlying layer, or the "parent layer" as named by the authors. The values of Ea_i and C_i are obtained from TGA data fitting. The model further describes in more detail the initial polymorph growing stage since the diffusion resistance in the developing oxide layer is much smaller than that of the polycrystalline oxide layer. More detailed mathematic descriptions can refer to Ref. (64).

The phase transformation rate of the amorphous→γ-Al_2O_3 transition and the $\gamma \rightarrow \alpha$–$Al_2O_3$ transition is described by an oxide surface outward growth rate:

$$\dot{m}^{tr}_{(i-1)\rightarrow i} = 4\pi r_{i-1}^2 \rho_{i-1} v_{(i-1)\rightarrow i}, \tag{3.5}$$

where r_{i-1} is the radius of the parent layer. $v_{(i-1)\rightarrow i}$ is the oxide growth velocity given as a phenomenological expression

$$v_{(i-1)\rightarrow i} = F_{(i-1)\rightarrow i} T_p (1 - exp(-\frac{K_{(i-1)\rightarrow i} h_{i-1}}{RT_p})) exp(-\frac{Ea_{(i-1)\rightarrow i}}{RT_p}), \tag{3.6}$$

where parameters $F_{(i-1)\to i}$ and $K_{(i-1)\to i}$ describe the effect of the parent oxide thickness, determined by fitting to the experimental TGA data. h_{i-1} is the thickness of the parent layer.

Instead of putting effort into quantifying the detailed morphology change process during Al oxidation, some studies (65; 66) simplified the oxidation and described the growth of the oxide thickness as a single parabolic law with an Arrhenius-type rate constant expression

$$\dot{m}^{ox} = \pi d^2 C_{ox}\, exp(-\frac{Ea}{RT_p}), \tag{3.7}$$

where C_{ox} is the oxidizer concentration. Ea and K are activation energy and pre-exponent, respectively.

The heat release rate during Al solid phase oxidation is then given as

$$\dot{H}_{solid,\,Al} = \sum_i (\dot{m}_i^{ox} \cdot \xi \cdot \Delta H_{R2} + \dot{m}_{(i-1)\to i}^{tr} \cdot \xi \cdot \Delta H_{Al_2O_{3(i-1)\to i}}), \tag{3.8}$$

where ξ is the stoichiometric fuel-oxidizer mass ratio of Al/O; ΔH_{R2} is the reaction heat [J/kg Al] of R2 and $\Delta H_{Al_2O_{3(i-1)\to i}}$ is the transformation heat between different morphologies of Al_2O_3. Following the work of Trunov *et al.* (64), $\Delta H_{Al_2O_{3(i-1)\to i}} = 0$. This means only the oxidation heat release is considered.

It should be noted that the above descriptions of single Al solid phase oxidation have not yet been implemented into the metal "Point particle model". They are listed here for future investigation of Al ignition.

3.1.3 Al: Melting-Ejection-Model (MEM)

From some of the experimental cases conducted by the collaborators from the Lund metal research lab, Al particle combustion is suspected to be pre-ignited before the melting of the Al_2O_3 shell. This is evidenced by the much lower surrounding temperature than the melting point of alumina at the ignition point detected by the high-speed camera. The Al particle can burn before the melting point of the shell. Moreover, the Scanning Electron Microscopy (SEM) analysis of the solid residues collected downstream in the experiments observed thin and hollow spheres with sharp-edged holes resembling eggshells, as seen in the rightmost images in Fig. 3.1. The density of Al can decrease by about 8% when its temperature increases from 300 K to the melting point (933 K) and another 5% decrease during the melting process (67), while the density of alumina is almost the same at its solid state (68). The pressure buildup in the core is calculated as 6.8 GPa taking the bulk modulus of Al to be ~50 GPa (69) at the Al melting point. This is significantly greater than the tensile strength of the alumina layer (0.1–0.25 GPa (70)). When the solid oxide shell

can no longer withstand the pressure from the expanding liquid Al, it breaks, allowing the liquid Al to splash and evaporate into gaseous Al. The gaseous Al then mixes and reacts with oxidizers. The heat release from the gas phase reaction, in turn, heats the particle and accelerates the solid phase oxidation process. This leads to the proposal of the novel "MEM" in Paper II, as illustrated in Fig. 3.1 below.

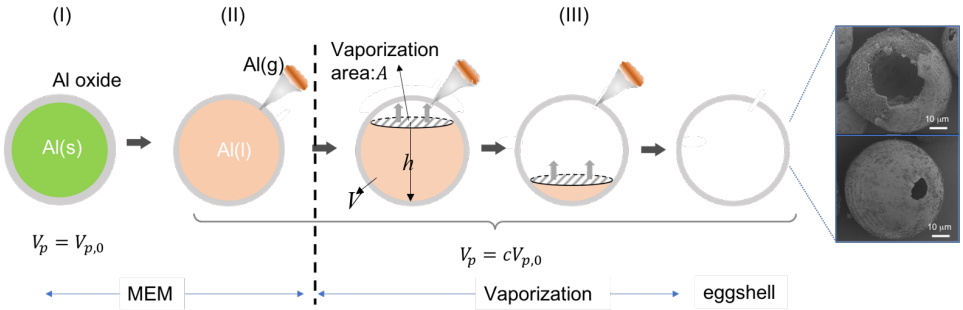

Figure 3.1: Schematic illustration of the MEM and vaporization process during Al particle heating, ignition, and combustion: I, particle heating and Al core melting; II, Al_2O_3 shell breaking and liquid Al droplets ejection; III, Al core evaporation and vapor Al combustion. The observed particle SEM images from experiments illustrating the eggshell structure are also presented.

The assumptions of the "MEM" are listed below:

(a) The heterogeneous solid phase oxidation is excluded due to its negligible oxidation mass change rate compared to the ejection from preliminary simulations.

(b) The diffusion of Al cations or O anions through the oxide layer is not considered.

(c) The Al_2O_3 shell does not expand along with the Al core before the particle ruptures.

(d) The particle ruptures once the volume of the liquid Al core is larger than a critical value, $V_{p,c} = cV_{p,0}$, i.e., c times the initial volume of the particle, $V_{p,0}$.

(e) Once the Al_2O_3 shell breaks, the liquid Al is ejected from the liquid core through the holes on the Al_2O_3 shell and splashes into tiny droplets.

(f) The tiny droplets of liquid Al undergo instant vaporization and reaction.

(g) The eruption process is driven by the thermal expansion of the liquid Al core; it finishes after the particle temperature no longer increases or after the oxide shell melts.

According to the assumption (d) listed above, once the volume of the liquid Al core reaches the critical volume $V_{p,c}$, the volume of the liquid Al core will not increase. Thus, the mass of the liquid Al core within the particle will be

$$m_{\mathrm{Al}} = \rho_{\mathrm{Al}} V_{p,c}. \tag{3.9}$$

Here, ρ_{Al} is the density of the liquid Al, which is a function of the particle temperature T_p. ρ_{Al} in different phase states is written as (67)

$$\rho_{\text{Al,s,l}} = f(T_p) = \begin{cases} 2648 + 0.322T_p - 4.99(T_p/100)^2 & T_p < 933 \text{ K} \\ 2670 - 0.299T_p & 933 \text{ K} < T_p < 2500 \text{ K} \end{cases}. \quad (3.10)$$

$V_{p,c} = cV_{p,0}$, where c is a model constant, which reflects the extent of the particle expansion. Rosenband (71) found that the most significant stress in the oxide film develops just after the melting of Al, i.e., ~933 K. From Eq. 3.10, ρ_{Al} decreases by ~5% during melting. Regarding this, c is set at $\rho_{\text{Al,l}}(933.47 \text{ K})/\rho_{\text{Al,s}}(298 \text{ K}) = 1.13$, indicating that shell breaking and ejection occur after the melting.

When the particle expands to its critical rupture volume, $V_{p,c} = cV_{p,0}$, further increase in the particle temperature will not increase the particle volume. Instead, the liquid will start to eject to the ambient gas, and the volume of the particle is assumed to remain at its maximum expanded value, $V_{p,c}$. The ejection rate can be calculated as

$$\dot{m}_{\text{eject}} = -\frac{dm_{\text{Al}}}{dt} = -V_{p,c}\frac{d\rho_{\text{Al,l}}}{dt} = -V_{p,c}f'(T_p)\frac{dT_p}{dt}. \quad (3.11)$$

The ejection ends when T_p reaches the melting point of the oxide layer, i.e., 2327 K. The ejection also ends when there is no net heat flux from the Al vapor reaction or the surrounding oxidizer. In that case, the Al particle temperature decreases, leading to an increase in ρ_{Al} and volume shrinkage of the Al particle. Thus, no oxide stress is formed. However, there can still be evaporation from the inner liquid Al surface after the ejection ends. The modeling of this inner-sphere evaporation rate will be discussed in detail in Section 3.4.

The heat release rate is then modified to account for the ejection process:

$$\dot{H}_{solid,\,Al,\,eject} = \sum_i (\dot{m}_i^{ox} \cdot \xi \cdot \Delta H_{R2} + \dot{m}_{(i-1)\to i}^{tr} \cdot \xi \cdot \Delta H_{\text{Al}_2\text{O}_{3(i-1)\to i}}) + \dot{m}_{\text{eject}} \cdot \xi \cdot \Delta H_{R2}. \quad (3.12)$$

3.2 Melting

In this work, the phase change of both Fe and Al is modeled assuming the equilibrium state, i.e., the temperature is constant during the phase change. Thus, the phase change rate is determined by the net heat flux:

$$\frac{dm}{dt} = \frac{\dot{H}_{ox} - \dot{H}_{ht}}{h_f}, \quad (3.13)$$

where h_f denotes the fusion energy, given in Table 1.1 and 1.2. $\dot{H}_{ox}$ is the oxidation heat release rate given as oxidation rate multiplied by reaction heat. $\dot{H}_{ht}$ is the heat transfer between the particle and the surrounding gas calculated from Eq. 2.9 and 2.10.

3.3 Liquid phase oxidation

The modeling method of liquid phase oxidation is similar to that of solid phase oxidation. The oxidation rate for Fe is assumed to be diffusion-limited. For Al, possible heterogeneous reaction pathways and Al consumption rates are discussed here, but it is not implemented neither in the metal "Point particle model" nor in the "Boundary layer resolved model" in this thesis as a preliminary investigation. It will be shown in Section 4.3 (Paper III) that the simulation results from the "Point particle model" for Al indicate that pure vapor phase combustion cannot sustain the development of a steady flame envelope, and other heat sources such as radiation or heterogeneous surface reaction need to be considered. In the future, this can be implemented to provide a more comprehensive understanding of the single Al particle combustion.

3.3.1 Fe

The Fe–O phase diagram (43) shows two distinct compositions in the liquid phase, termed as L1 (liquid iron) and L2 (liquid oxide). The liquid phase reaction is then described as:

$$L_1 + 0.5\,O_2(g) \longrightarrow L_2 \tag{R3}$$

It is worth noting that L1 and L2 do not have a fixed composition. The latest update of the Fe–O phase diagram (72) reported an O molar ratio of up to 10% and 47–58% in L1 and L2, respectively. The variation of oxygen concentration in L1 and L2 makes it challenging to determine their thermodynamic properties. A simplification is made here to substitute the thermodynamic data of L1 and L2 with that of Fe(l) and FeO(l), which are the only liquid species with well-established thermodynamic data in the NIST-JANAF database (44).

It will be discussed later in Section 4.1 (Paper I) that a diffusion-controlled melting process is identified based on the experimental data. This indicates a higher rate of reaction than diffusion at the melting temperature (T_m). The reaction rate increases more prominently compared to that of oxygen diffusion rate when temperature increases (73). Thus, at a particle temperature of $T_p > T_m$, the rate of reaction will be higher than the rate of diffusion. This leads to an argument of a diffusion-controlled combustion process in the liquid phase oxidation, as discussed in Section 1.2. Ning *et al.* (74) also suggest that the particle burning is primarily controlled by oxygen diffusion in the gas surrounding until

the particle reaches the peak temperature. Meanwhile, the diffusion of oxygen ions through the oxide layer is ignored in this process due to the uniform oxygen concentration found in the oxide layer of the quenched sample (75; 76).

Set against this, the liquid phase oxidation rate is determined by considering a diffusion-controlled combustion:

$$\dot{m}_{O_2} = A_p k_d (\rho_{O_2,g} - \rho_{O_2,s}), \tag{3.14}$$

where $\dot{m}_{O_2}$ is the consumed oxygen mass as per R3. $\rho_{O_2,g}$ and $\rho_{O_2,s}$ are the oxygen partial density (kg/m^3) in the surrounding gas and near the particle surface, respectively. k_d is the diffusion rate given as $k_d = \mathrm{Sh} D_f / d_p$. The liquid phase particle has a spherical shape due to surface tension, thus $A_p = \pi d_p^2$. Meanwhile, $\rho_{O_2,s}$ is simplified to 0, assuming the limited case. This "diffusion-limited" assumption will be evaluated in section 4.1.

The heat release rate during Fe liquid phase oxidation is then calculated from $\dot{m}_{O_2}$ as

$$\dot{H}_{liquid,\,Fe} = \dot{m}_{O_2} \cdot \xi \cdot \Delta H_{R3}, \tag{3.15}$$

where ξ is the stoichiometric fuel-oxidizer mass ratio of Fe / O, and ΔH_{R3} is the reaction heat [J/kg Fe] of R3.

3.3.2 Al

For Al liquid phase oxidation, the Al–O phase diagram in Fig. 1.3 shows two distinct compositions in the liquid phase, also termed as L1 and L2, which denote the Al-rich composition and Al_2O_3-rich composition, respectively. Compared to that of the Fe liquid phase, the solubility of O in Al and Al_2O_3 is reported to be much lower (<0.1 %) (45). The thermodynamic properties of Al and Al_2O_3 are obtained from the NIST-JANAF database (44).

As discussed in Section 1.2, although Al combustion is vapor phase dominated, signs of liquid phase oxidation also exist. Derizin *et al.* (37) found Al-O solutions formed inside the burning Al particle from the cross-section of the quenched burning particle, which was considered as a result of the heterogeneous surface reaction between the particle and the gaseous products transporting from the flame zone. Based on the phase diagram, the authors described this reaction as

$$L_1 + (Al_2O + AlO + Al_2O_2 + NO)_{gas} \xrightarrow{2510\,K} L_1 + L_2 + (N_2)_{gas} \tag{R4}$$

where the reactions involving NO were also included. However, the oxidation rate was not mentioned in that work.

Later, in the Beckstead model (77), the authors adopted a simpler heterogeneous surface reaction as

$$L_1 + AlO(g) \longrightarrow Al_2O(g) \tag{R5}$$

and assumes a diffusion-limited reaction rate with the mass fraction of AlO at the particle surface to be zero, i.e., $Y_{AlO,\,s} = 0$.

3.4 Evaporation

Evaporation equations are considered both for the metal "Point particle model" within the Lagrangian-Eulerian framework and the "Boundary layer resolved model" within the Eulerian framework. Evaporation is currently only addressed in Al particle combustion in this work. Considering that signs of vapor phase combustion for a Fe particle have also been observed from literature (19; 74), the evaporation sub-model can be extended to Fe particle combustion modeling in the future.

For Al, evaporation occurs when liquid Al forms and its surface is exposed to the surroundings. There exist both Al and Al_2O_3 phases in the particle. Their evaporation depends on the corresponding vapor pressure. Al vapor pressure is larger than that of its metal oxide (26), thus only the evaporation of Al is considered. In the Lagrangian framework, the evaporation rate is given assuming diffusion-controlled mass transfer (78):

$$\dot{m}_{\text{evap}} = -\frac{A}{d_{norm}}\text{Sh}\rho_s D_{\text{F}} ln(1+B), \quad T_m < T_p < T_b \tag{3.16}$$

where A is the evaporation area; d_{norm} is the apparent diameter perceived from the surrounding; Sh is the Sherwood number as per Eq. 2.12; ρ_s is the fuel vapor density near the droplet surface; D_{F} is the binary diffusivity of fuel vapor in the ambient gas mixture. The Spalding mass transfer number B is calculated as

$$B = \frac{Y_{\text{F,s}} - Y_{\text{F},\infty}}{1 - Y_{\text{F,s}}}, \tag{3.17}$$

where $Y_{\text{F,s}}$ and $Y_{\text{F},\infty}$ are the mass fractions of the fuel vapor at the evaporation surface and in the far field, respectively. $Y_{\text{F,s}}$ is calculated based on Dalton's law assuming fast equilibrium of the generated vapor:

$$Y_{\text{F,s}} = \frac{P_{F,\,sat} M_F}{(P_{atm} - P_{F,\,sat}) M_G + P_{F,\,sat} M_F}, \tag{3.18}$$

where $P_{F,\,sat}$ is the saturated vapor pressure. M_F and M_G are the molecular weights of the fuel vapor and the ambient gas mixture, respectively.

The saturated vapor pressure of Al in this work is taken from Ref. (79):

$$P_{F,\,sat} = exp(36.547 - \frac{39033}{T_p} - 1.3981 \cdot \ln(T_p) + 6.7839 \times 10^{-9} \cdot T_p^2. \tag{3.19}$$

For the Al "MEM" mentioned in Section 3.1, an exposed liquid Al surface can form inside the oxide shell when ejection ceases while there remains liquid Al. In that case, evaporation occurs on the exposed surface until the remaining Al liquid inside the particle is entirely evaporated, or particle temperature reaches the melting point of the oxide shell. The evaporation rate can still be calculated as per Eq. 3.16, whereas the particle apparent diameter d_{norm} is the diameter of the oxide shell, and the evaporation area is set as $A = \pi(d_{\text{norm}}h - h^2)$, with h determined from the volume of the remaining liquid Al as per $V = \pi h^2(d_{\text{norm}}/2 - h/3)$.

In the Eulerian framework, evaporation is considered as the mass flux in the *Fuel* boundary as shown in Fig. 2.1. There can exist potential heterogeneous surface reaction or deposition as discussed in Refs. (77; 80). These processes also lead to mass flux sources on the boundary. Those are not considered in the current model as a preliminary step. The species boundary mass flux is then written as:

$$\dot{\omega_i} = \begin{cases} \dot{\omega}_F, & i = \text{Al} \\ 0, & \text{otherwise} \end{cases}. \tag{3.20}$$

The total mass flux becomes

$$\dot{\omega} = \sum_i \dot{\omega_i} = \dot{\omega}_F. \tag{3.21}$$

The species conservation equation is given as

$$\dot{\omega_i} = \dot{\omega}(Y_i)_s - (\rho D_i \nabla Y_i \cdot \vec{n})_s, \tag{3.22}$$

where s denotes the interface; i is the i_{th} species; $\dot{\omega}$ [kg/m^{2}s] is the evaporation rate. $\vec{n}$ is the normal vector of the boundary. Eqs. 3.20-3.22 indicate that the net flux of Al is equal to the Al evaporation rate. The diffusion of Al is balanced by the bulk flow at the surface. For other species, the net flux at the surface is zero, i.e., there is no accumulation. The bulk velocity from the droplet surface, i.e., the Stefan flow velocity, can be derived from Eq. 3.22 considering i as Al (denoted as "F"):

$$v_{st} = \dot{\omega}_F \cdot (\frac{1}{\rho})_s \cdot \vec{n} = \frac{-(D_F \nabla Y_F \cdot \vec{n})_s}{1 - (Y_F)_s}. \tag{3.23}$$

The mass fraction of Al at the boundary, $(Y_F)_s$, is calculated according to Eq. 3.18 and Eq. 3.19. The species mass fraction Y_i and the v_{st} are considered as the *Fuel* boundary condition when implemented in the Eulerian framework.

The conservation of energy at the boundary, in general, is given as

$$(-\lambda \nabla T \cdot \vec{n})_s + Q_r = h_v \dot{\omega} + Q_s, \tag{3.24}$$

where λ and h_v are the gas phase thermal conductivity and heat of evaporation, respectively. The first term on the left-hand side (l.h.s) in the equation denotes the conductive heat flux transferred to the droplet surface from the surrounding hot gas; the second term on the l.h.s denotes the radiative heat flux from the hot gas and alumina smoke in the flame zone to the droplet surface; the right-hand side (r.h.s) terms denote the evaporation heat flux and heterogeneous reaction or deposition heat flux generated on the droplet surface, respectively. Currently, only the evaporation heat flux is considered on the droplet surface, with $Q_s = 0$. As for Q_r, information regarding the number density and volume fraction of the alumina smoke is insufficient, resulting in difficulty and uncertainty in the accurate modeling of Q_r. Meanwhile, considering the availability of experimentally measured surface temperature, the fixed temperature boundary condition instead of Eq. 3.24 is adopted in the current "Boundary layer resolved model". However, Eq. 3.24 will be used to analyze the Q_r and Q_s terms later in the model validation (Section 4.3).

3.5 Gas phase oxidation

Gas phase oxidation equations are considered both for the metal "Point particle model" within the Lagrangian-Eulerian framework and the "Boundary layer resolved model" within the Eulerian framework. This sub-model is currently only addressed in the Al particle combustion. Considering that signs of vapor phase combustion for a Fe particle have been observed as well from literature (19; 74), the gas phase sub-model can be extended to Fe particle combustion modeling in the future.

In the Lagrangian framework, the gas composition and properties surrounding the particle are unified within the cell where the particle is located. For metals featuring the vapor phase combustion mode, e.g., Al, the surrounding flame zone envelopes the particle and provides heat back to sustain particle evaporation. To reveal the flame envelope structure, the cell size needs to be set at a very small value. This makes the simulation difficult to converge and also increases the computation cost. To account for the elevated heating from the flame zone, a "Reaction Heat Redistribution" (RHR) model is proposed in paper II.

An additional heat transfer term Q_f is introduced to redistribute the gas phase reaction heat to the particle:

$$Q_f = \gamma Q_c \dot{m}_p, \tag{3.25}$$

where Q_c represents the reaction heat release per unit mass of evaporated Al [J/kg Al] and γ specifies a redistribution ratio of the total reaction heat. Q_c is temperature dependent, and γ can be determined from the "Boundary layer resolved model". To demonstrate this concept of reaction heat redistribution, Q_c and γ are currently treated empirically. Q_c is considered at a reference ambient temperature of $T_{ref} = 1500$ K in the range 930–2327 K. Depending on whether the oxidizer is steam or oxygen, Q_c is calculated as 28.7 MJ/kg or

42.7 MJ/kg, respectively (44). For γ, it is determined under the assumption that the evaporation is driven by combustion heat release and γQ_c will compensate for the evaporation heat needed, i.e., $\gamma = L_{evap,T_{ref}}/Q_c \approx 0.395$. The determination of γ is further verified in Paper II.

In the "Boundary layer resolved model", the gas phase reaction is modeled using a finite rate chemistry model. Detailed gas phase combustion kinetics can be implemented in the OpenFOAM solver. The kinetic file and the thermodynamic data file are in CHEMKIN format. For the transport properties, the Sutherland transport model is applied, and the diffusivity coefficients of Al-related species are fitted from the diffusivity plot using CHEMKIN PRO 2020R2 (57).

The Glorian mechanism (80) is the main gas-phase mechanism adopted in this project. For the investigated condition, 21 species and 45 reactions are extracted to constitute the Al / O_2 / H_2O gaseous sub-mechanism. The product from the gas phase reaction is observed in experiments to be nano-sized liquid alumina smoke (22). Nevertheless, in the Glorian mechanism, this process is described by an irreversible, fast, and barrierless reaction that generates "gaseous" $Al_2O_3(L)$. Those "gaseous" $Al_2O_3(L)$ molecules feature thermodynamic properties of the condensed Al_2O_3; the enthalpy change due to condensation is thus considered. The motion of Al_2O_3 molecules is governed by the gaseous species transport equation (Eq. 2.3) since the Stokes number of the nano-sized liquid alumina particles is low.

3.6 Solidification/Condensation

Solidification is considered within the Lagrangian-Eulerian framework for the Fe particle combustion as the burning metal particle is cooled by the surroundings. On the other hand, condensation is considered within the Eulerian framework for the Al particle combustion as Al is vapor phase combustion dominated and condensation mainly occurs as the formation of nano-sized reaction product in the flame zone.

3.6.1 Fe

In the "Point particle model", solidification can be modeled as a reverse process of equilibrium melting based on Eq. 3.13. The solidification temperature is the same as the melting temperature, and the energy released during solidification is the same as the fusion energy. Thus, the solidification rate is determined by the net heat flux transporting to the particle.

However, experimental results from the collaborators (19) as well as from other literature (74) observed an interesting intensity jump, which is also called a spearpoint, at the

start of solidification. We explained this as a sudden solidification of the super-cooled particle accompanied by an internal phase transformation. Ning *et al.* (28) further conducted the two-color thermometry measurement and confirmed that this radiant intensity jump is a temperature jump. The measured temperatures before and after the spearpoint are 1694 K and 1877 K, respectively. Combined with the Fe–O phase diagram in Fig. 1.2, possible phase transition reactions are pointed out to explain this special jump: the eutectic reaction $L_2 \longrightarrow Fe_3O_4(s)$ + gas (1 atm) (1855 K) or the congruent solidification reaction $L_2 \longrightarrow Fe_3O_4(3)$(∼1870 K). These temperatures are lower than the solidification/melting point of Fe-oxides (1870 K), indicating that the particle is super-cooled. The modeling of the super-cooled solidification consists of two sub-stages which are implemented in OpenFOAM by collaborator Dr. Shijie Xu in Paper I:

1) The first stage of solidification is assumed to be transitional and infinitely fast. It is triggered once particle temperature reaches the lower jump point, denoted as $T_{s,-}$ herein. Then, the particle temperature increases to the higher jump point, denoted as $T_{s,+}$, in an infinitely short time. The corresponding mass change of L2 is

$$\Delta m_{L_2} = -\frac{1}{h_f}\int_{T_{s,-}}^{T_{s,+}} m c_p(T) dT, \tag{3.26}$$

where h_f is the fusion heat for FeO given in Table 1.1. m is the particle mass and c_p is the sensible heat capacity [J/kg K]. As the first stage of solidification is assumed to be infinitely fast, the heat transfer during this transition period is ignored.

2) The second stage solidification is assumed to be in thermal equilibrium, i.e., the particle keeps a constant temperature $T_{s,+}$, which leads to a solidification rate of

$$\frac{dm_{L_2}}{dt} = -\frac{\dot{H}_{ht}}{h_f}. \tag{3.27}$$

The model parameters $T_{s,-}$ and $T_{s,+}$ can be obtained from experimental measurement. Current data of this temperature jump have been reported to be 1694 / 1877 K by Ning *et al.* (28), and 1670 / 1970 K by Dreizin *et al.* (81).

3.6.2 Al

In the "Boundary layer resolved model", the gas phase reaction surrounding the center Al droplet leads to the formation of the condensed nano-sized Al_2O_3 layer in the vicinity of the flame zone. This condensation process is important as it is accompanied by a large part of the total heat release (∼50%). This process is treated differently in different Al kinetic mechanisms.

Huang *et al.* (82) adopted a simple reversible reaction $Al_2O_3(g) = Al_2O_3(L)$ to represent the condensation process. The authors assumed a fast equilibrium phase transition with a high pre-exponential factor (1E14), ZERO temperature exponent, and activation energy. Glorian *et al.* (80; 83) followed this simplification but further increased the pre-exponential factor to 1E15 and examined the difference between adopting reversible and irreversible reactions on the predicted flame temperature, AlO, and $Al_2O_3(L)$ molar fraction profiles. They found that generally, the spatial flame temperature profile and the distribution of $Al_2O_3(L)$ near the flame region is much better captured with the irreversible reactions, although the peak position of the AlO profile predicted by the reversible reactions is closer to experimental data. Aware of a lack of knowledge, the Glorian *et al.* chose the irreversible type. As a preliminary step, the condensation process in the current thesis follows that of the mechanism from Glorian *et al.* (80). Other approaches for modeling the condensation process are described in detail in Paper IV. The limit of adopting this fast equilibrium reaction is acknowledged and requires further development in the "Boundary layer resolved model".

3.7 Summary of governing equations and numerical methods

Based on the descriptions in the previous sections, the governing equations currently implemented in the "Point particle model" and the "Boundary layer resolved model" for modeling Al and Fe are listed and summarized below.

Table 3.1: Governing equations for the "Point particle model" and the "Boundary layer resolved model" for modeling single Fe and Al particles.

	I. Point particle model		II. Boundary layer resolved model
	Fe	Al	Al
General equations	Eqs. 2.5–2.12		Eqs. 2.1–2.4
Solid-phase oxidation	Eqs. 3.1–3.2	3.9–3.12 ("MEM")	–
Melting	Eq. 3.13	Eq. 3.13	–
Liquid-phase oxidation	Eqs. 3.14–3.15	–	–
Evaporation	–	Eqs. 3.16–3.19	Eqs. 3.20–3.23
Gas-phase oxidation	–	Eq. 3.25	
Solidification/ Condensation	Eqs. 3.26–3.27 ("super-cooled" solidification)	–	Glorian mechanism (80)

The two models are implemented in OpenFOAM version 7 (48) based on the finite volume method. The gas phase continuity, momentum, species, and sensible enthalpy transport equations are solved with a second-order accuracy scheme, e.g., the diffusion and convection terms are discretized by a filtered-linear scheme, while the time integration is based on

an implicit backward scheme. In the "Point particle model", the particle seeding density is very low, and the effects of the particle mass and enthalpy change on the surrounding flame are negligible. Thus, only the particle phase is solved and the surrounding gas is considered as an input boundary condition. More details can refer to the experimental set-up Chapter 4.

Chapter 4

Results and discussion

In this chapter, the generalized combustion models, including the metal "Point particle model" and the "Boundary layer resolved" model, are validated and analyzed against experimental results. Single Fe and Al particles are studied, respectively. For Fe combustion modeling, the effort is put into simulating the whole five-stage burning process: solid-phase oxidation, melting, liquid-phase oxidation, cooling, and solidification of the super-cooled droplet. Characteristic times within each stage are compared against experiments (Paper I). For Al combustion modeling, the effort is more on the proposal of a pre-ignition model, the "Melt-Ejection-Model" (MEM), to explain the hollow egg-shell morphology observed from experiments (Paper II). Another effort on Al combustion modeling is the development of "Boundary layer resolved" model where the temperature and species profiles in the vicinity of a burning Al droplet are calculated and agreeable results of flame temperature and stand-off ratio are obtained in comparison with experimental data (Paper III). Based on this model, a review and analysis of available Al gas phase combustion kinetics in the oxygen and steam environments are performed, and important reactions and the reaction pathways are addressed (Paper IV). Apart from these, another work is presented in Paper V regarding the construction of an updated mechanism of Al gas phase reactions as well as the rate constants, but they are not discussed in this thesis.

The experimental data used for model validation are mostly from the recent works by the author's collaborators, except the Al/air case in Section 4.3, which is from earlier literature. The author did not participate in the experiments but was involved in the data analysis and discussions. Details of the experimental data are available in the referenced publications. However, since these experimental data are important for model validation, they are also briefly explained in this thesis.

4.1 Single Fe particle combustion

4.1.1 Experimental case setup

Figure 4.1 shows the experimental setup as implemented in the simulation. Sparse iron particles are supplied from an N_2 jet in the central pipe, which has an inner and outer diameter of 1.55 mm and 2.55 mm, respectively. A mixture of premixed CH_4 / O_2 / N_2 flows through the 60 mm diameter McKenna burner and is ignited at the burner exit, providing a high temperature and high oxygen concentration environment. Four cases are studied, keeping a constant flow rate of 0.5 L/min for the N_2 jet and 24.1 Standard Liter per minute (SL/min) for the pilot CH_4 / O_2 / N_2 mixture. The compositional flow rates under each case are listed in Table 4.1 below. Both the central jet and pilot mixtures have an initial temperature of 302 K. Preliminary adiabatic flame calculations indicate a decrease in the residual oxygen concentration while an increase in the maximum flame temperature from Case 1 to Case 4. The gas flow has a Reynolds number from ∼100 (pilot flame) to ∼1000 (center jet), i.e., the flow is laminar. Detailed numerical simulation is employed for the gas phase flow simulation. The computational domain is a cylinder with a radius of 200 mm ($129D$, where D is the diameter of the central fuel jet) and a height of 500 mm ($323D$), covering the central N_2 jet flame, the pilot flat-flame burner, and the ambient air. A 2-D axisymmetric mesh is employed. The total number of cells is 32400, with a minimum grid size of 0.43 mm in the axial (z) direction and 0.04 mm in the radial (x) direction around the shear layer.

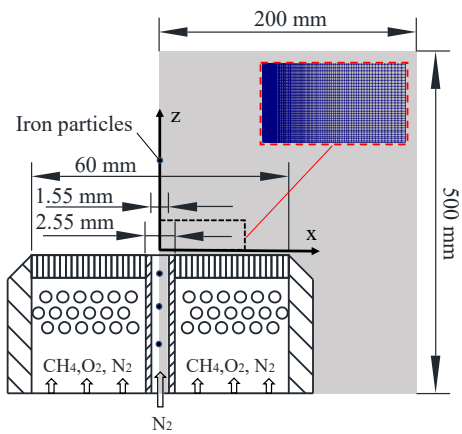

Figure 4.1: Schematic of the experimental setup and the computational domain (grey color) for the single Fe particle combustion, as well as the single Al particle combustion in Section 4.2.

In experiments, the pulverized sponge raw iron particles are sieved and divided into four size groups. Size groups with mean diameters of 20, 40, 60, and 80 μm are represented as D20, D40, D60, and D80, respectively. In simulations, single particles are injected from

the exit of the central pipe. The initial particle velocity is set to be its terminal velocity, u_t, at which the drag force and gravity have the same magnitude with opposite direction (74). In the present study, Re_p is from 1.5×10^{-3} (D20 in hot gas) to 5.6 (D80 in cold gas), i.e., the flow surrounding the particle is also laminar. Therefore, the drag coefficient C_D can be estimated according to Eq. 2.8.

The five-stage single Fe combustion model was proposed by the author after a thorough literature review, based on the discussions in Chapter 3. The implementation of the code and the simulation were mainly performed by the author's collaborator Dr. Shijie Xu. The author also contributed to the analysis of the simulation results.

Table 4.1: Experimental compositions for the CH_4 / O_2 / N_2 pilot flame and the central N_2 jet (19).

Case No.	Pilot flame [SL/min]			Central jet [SL/min]
	CH_4	O_2	N_2	N_2
1	1.60	12.81	9.67	0.5
2	2.24	12.45	9.39	
3	2.90	12.07	9.11	
4	3.74	11.58	8.74	

4.1.2 Modeling results

The five-stage combustion of a single Fe particle

Figure 4.2(a) shows the particle trajectories from both measurements and simulations. The dash-dot red line represents the streamline of the central jet. The solid and dashed black lines show the particle trajectories with diameters of 80 and 100 μm, respectively. It is worth noting that, at the burner exit, the temperatures of the gas and particles are relatively low, i.e., ~300 K. In experiments, D80 particles located below a Height Above Burner (HAB) of 29.4 mm are invisible in the camera due to their weak radiant intensity. Thus, the x-axis in Fig. 4.2(a) represents the relative time t - t_0, where t_0 is defined as the time at 29.4 mm HAB. In experiments, it is observed that most of the particles follow the central line and are centralized in a narrow cone region within a cone angle of 10°.

Fig. 4.2(b) shows the averaged gas phase temperature (T_g) and oxygen mass fraction (Y_{O_2}) in this cone region at different HAB. The results are obtained from numerical simulations. Due to the mixing of the cold central N_2 jet and the hot CH_4 / O_2 / N_2 pilot flame, T_g and Y_{O_2} increase over height when HAB is below 30 mm. As the height increases, both T_g and Y_{O_2} reach a plateau where most particles are ignited. From Case 1 to 4, the maximum T_g increases from 1665 K to 2623 K, while Y_{O_2} decreases from 0.406 to 0.232.

The simulation results for a typical particle in the D80 size group of Case 3 (the same particle

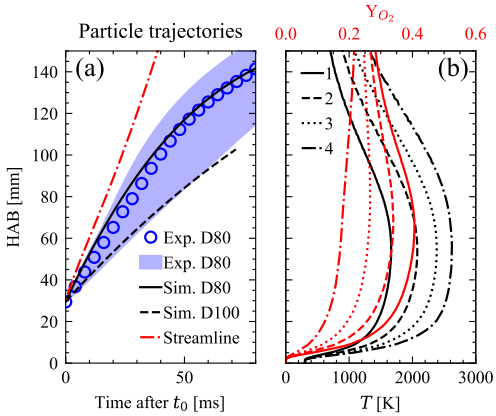

Figure 4.2: (a) The particle trajectories (Height Above Burner (HAB) over time) from both measurements and simulations. The range of measured particle trajectories for D80 is marked in blue shadow. Symbols represent the trajectory of the particle shown in Fig. 4.3(a). Lines are trajectories from numerical simulations. (b) The predicted averaged gas temperature (T_g, black) and oxygen mass fraction (Y_{O_2}, red) in a 10° cone alongside the central line of the N_2 jet in cases No. 1–4 in Table 4.1.

denoted as symbols in Fig. 4.2(a)) are shown in Fig. 4.3, together with the experimentally measured intensity. It can be seen that the predicted temperature follows a similar trajectory to the measured particle radiant intensity. Also shown in the figure is a schematic illustration of different particle phases in the combustion process and the temporal evolution of species mass fractions inside the particle.

Five stages are captured in this phenomenological model:

1) Solid phase oxidation (Phase A-B). This happens immediately after the original Fe particle enters the hot flame. Solid Fe reacts with gaseous oxygen to form a thin outer layer of solid iron oxides. The particle is heated by both heat release from the oxidation and heat transfer from the surroundings. The particle temperature increases until it reaches the melting point of FeO(s), i.e., T_m = 1650 K from Table 1.1.

2) The first phase change (melting). This is characterized by the plateaus in the radiant intensity and temperature curves. There should be two plateaus in melting, for both iron oxide (Phase B, T_m = 1650 K) and iron (Phase C, T_m = 1811 K). In Phase B, as shown in Fig. 4.3(d), FeO(s) forms and soon disappears, accompanied by a rapid increase of L2. However, this melting proceeds quickly, and the plateau is not evident due to the very small amount of oxides compared to the raw Fe.

3) Liquid phase oxidation. This starts when L1 is formed in the particle. The gaseous oxygen reacts with L1 to form L2 (Phase D). Both radiant intensity and temperature increase dramatically after melting is completed, indicating an intense heat release in the liquid phase oxidation. This stage also accounts for the main heat release. Particle temperature quickly

rises to the peak point (Phase E), where all L1 turns into L2 and heat release is completed.

4) Cooling (Phase E–F). The particle temperature drops due to heat loss to the surroundings. It is worth noting that at this stage, there is a sudden drop in particle radiant intensity, cf. Fig 4.3(a) in between t_3 and t_4, which is associated with the release of nano-size oxides and has been observed and discussed in Ref. (19).

5) The second phase change (solidification). Herein, a temperature jump before the plateau (Phase F-G) due to super-cooling is successfully captured. Finally, the particle cools down as the solid iron oxide (Phase H).

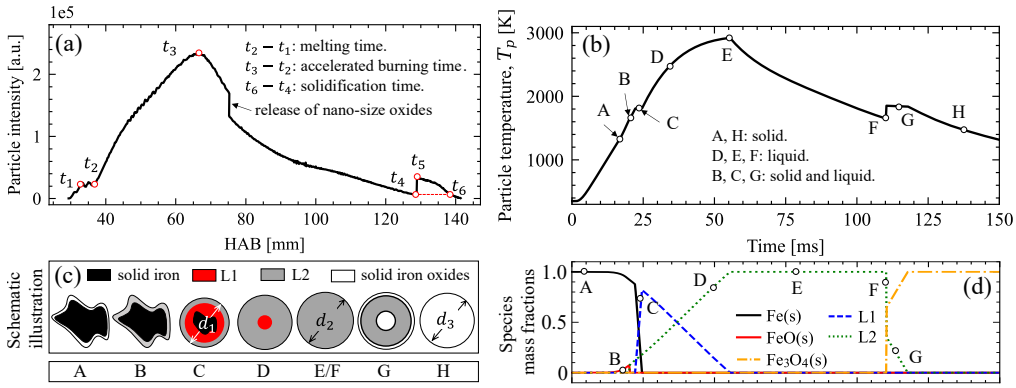

Figure 4.3: (a) A typical particle radiant intensity (I) measured in the D80 group under Case 3, and (b) the corresponding particle temperature (T_p) predicted in simulations. It is the same particle denoted as symbols in Fig. 4.2(a). (c) Schematic illustration of the five stages in iron combustion. (d) Temporal evolution of the main solid and liquid species mass fractions during the five stages.

The proposed five-stage combustion model can be compared with experimentally observed particle trajectory and morphology evolution shown in Fig. 4.4 below. The images are recorded and processed by the collaborators in the Lund metal research lab. In Fig. 4.4(a), the pilot flame is shown as the flat blue pattern at the bottom, and the micron-sized Fe particle combustion trajectory is characterized by the vertical bright stripes. Figure 4.4(b–d) shows the morphologies observed from the SEM images of sampled combustion products after they cool down in the experiments. The phase change is evidenced by the surface morphology change before and after the combustion, i.e., from an irregular shape in Fig. 4.4(b) to a spherical shape in Fig. 4.4(d). The melting process is captured in Fig. 4.4(c). Accordingly, the proposed model illustrates the particle morphology change from an irregular shape before melting to a spherical shape afterward (Fig. 4.3(c)). Furthermore, the particle diameter d_p increases first during combustion and decreases in the solidification stage due to the density difference of solid and liquid phases (75), i.e., $d_1 < d_3 < d_2$.

Overall, the five-stage model well explains the current experimental results. However, in some cases, special phenomena such as hollow structures, e.g., Fig. 4.4(d), micro explosion (20), and nano-size oxides (19; 74), have also been reported. This indicates that in the

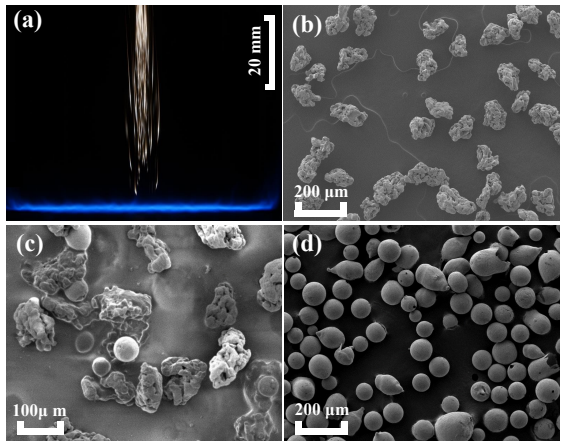

Figure 4.4: Experimentally observed (a) Fe particles in premixed CH_4 / O_2 / N_2 pilot flames, and (b–c) the combustion stages of pulverized sponge iron particles represented by the SEM images of sampled particles. (b) Before burning. (c) During the melting stage. (d) After combustion. The images are recorded and processed by the collaborators in the metal research lab at Lund University.

real case, the combustion is more complicated.

Assessment of the "diffusion-limited" assumption

In Section 3.3, a "diffusion-limited" assumption is adopted to describe the liquid phase oxidation of Fe particles. Previous experimental and theoretical studies of liquid iron combustion (58; 84; 85) concluded consistently that the kinetic-controlled particle burning rate, or the oxygen consumption rate, is proportional to the square root of oxygen partial pressure, $\sqrt{p_{O_2}}$, which, under constant surrounding temperature, is proportional to $\sqrt{\rho_{O_2,g}}$ as per the ideal gas law. On the other hand, for diffusion-controlled melting, the heat release rate $\dot{H}_{ox}$ is proportional to $(\rho_{O_2,g} - \rho_{O_2,s})$ according to the Fick's diffusion law. Furthermore, $\dot{H}_{ox}$ is proportional to $\rho_{O_2,g}$ under diffusion-limit condition as $\rho_{O_2,s} \approx 0$. Thus, in our experiments, the correlation of the oxidation heat flux ($\dot{H}_{ox}$) and the oxygen partial pressure ($\rho_{O_2,g}$) indicates the dominating combustion mode of the Fe particle.

The melting process is selected for analysis due to its constant temperature feature. Eq. 3.13 is used here to estimate the oxidation heat release rate during melting. The measured Melting Time (MT, t_2-t_1 in Fig. 4.3(a)) shows a very quick melting process (max. 3.2 ms at D80 Case 4); thus, the flow field around the particle does not vary much. T_p, T_g, $\rho_{O_2,g}$, and $\dot{H}_{ht}$ remain almost constant under each condition and can be extracted from numerical simulations. $\dot{H}_{ox}$ depends either on the oxygen diffusion rate or the kinetic reaction rate, both of which are constant at constant T_p. The reaction surface area, either on the L1/L2 boundary or the L2/gas boundary, can be assumed constant. Thus, $\dot{H}_{ox}$ can be assumed

constant as well. As per Eq. 3.13, solid iron mass reduces almost linearly. With the MT data, $\dot{H}_{ox}$ can be estimated.

Figure 4.5(a) shows the estimated $\log_{10}(\dot{H}_{ox})$ vs. $\log_{10}(\rho_{O_2,g})$ for D60 and D80, together with a fitting line with unity slope. MTs in D20 and D40 are unavailable as they are too short to be measured in the experiments. As is indicated from the plot, the experimental data are more closely aligned with $\dot{H}_{ox} \propto \rho_{O_2,g}$ relationship, supporting a diffusion-controlled melting process rather than a kinetic-controlled one.

It should be noted that in some other modelling works (73; 86), the oxidation rate is defined considering both the kinetic rate and diffusion rate. In those works, the kinetic rate is estimated as a single-step first-order Arrhenius-like reaction, leading to $\dot{H}_{ox} \propto \rho_{O_2,g}$. The setting of this "first-order" seems contradictory to experiments (58; 84; 85). Thus, that method is not adopted in our model.

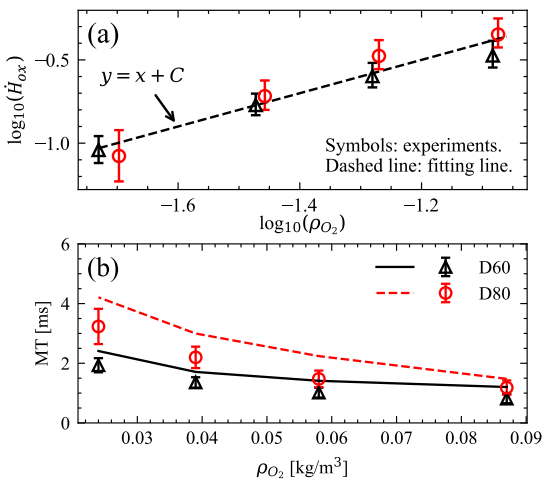

Figure 4.5: (a) The estimated oxidation heat release ($\dot{H}_{ox}$) as a function of oxygen partial density (ρ_{O_2}), shown in logarithmic scales. Symbols represent the measurements for D80 and D60. Dashed line is a fitting line showing $\dot{H}_{ox} \propto \rho_{O_2,g}$. (b) The predicted and measured melting time. Simulation results are shown using lines. Measurements are represented using symbols and error bars.

Figure 4.5(b) shows the measured and the predicted MTs. The trend of MT decreases over ρ_{O_2} is well-predicted. However, the current model over-predicts the MTs. This implies an underestimated oxygen diffusion during the melting process, although the "diffusion-limit" assumption and more precise transport data are adopted in the present model. One possible reason for the underestimated oxygen diffusion is that the surface area A_p from Eq. 3.14 is underestimated. The particle is assumed spherical, whereas the solid raw iron has a larger surface area with sponge-like morphology, cf. Fig. 4.4(b). Thus, A_p is underestimated at the beginning of the melting when a large amount of Fe(s) still exists. Interestingly, the overestimation of MTs has also been reported in a recent study (28), in which spherical

raw iron was used. Another possible explanation for the discrepancy is the non-thermal equilibrium melting process. Chattopadhyay and Goswami (87) reported delays in metal melting, i.e., metal remains solid at a temperature higher than the melting point, which is referred to as the "super-heating". This is usually observed in small particles under a fast heating process. A quick melting is triggered once the degree of super-heating reaches its critical value. In this case, a temperature drop takes place before the temperature plateau and the duration of the temperature plateau is shorter than the thermal equilibrium melting time.

"Super-cooled" solidification

Figure 4.6 shows the predicted particle temperature profile before and after the spearpoint for the same case as that of Fig. 4.3(a) (t_4–t_5 from the figure). Before the spearpoint, super-cooled L2 is formed after a fast cooling process. Right after the spearpoint, a temperature plateau is observed, followed by another cooling process. The temperature plateau is also referred to as thermal equilibrium solidification. During this stage, the particle temperature remains constant at $T_{s,+}$. It is worth noting that, in the thermal equilibrium solidification stage, the particle temperature does not change while the particle diameter decreases due to the density change, e.g., the density of L2 (3600–4900 kg/m^3) is lower than that of Fe_3O_4 (5180 kg/m^3) (75). Thus, the measured particle radiant intensity ($I \sim d_p^2 T^4$) decreases slightly during the equilibrium solidification stage, cf. Fig. 4.3(a) in this thesis and also Ref. (74).

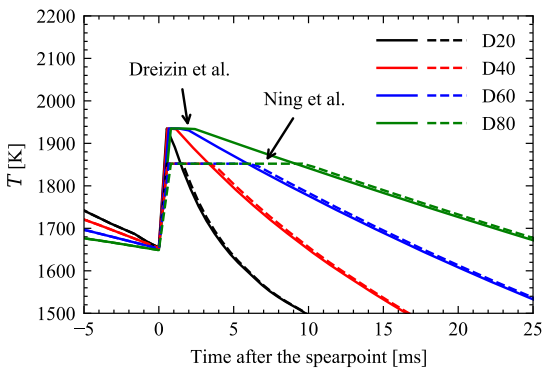

Figure 4.6: Temporal evolution of the temperature of the super-cooled iron oxide droplet during the two-stage solidification under Case 3. The simulation results based on the $T_{s,-}$ and $T_{s,+}$ measured by Dreizin *et al.* (81) (solid lines) and Ning *et al.* (28) (dashed lines) are both plotted.

As mentioned in Section 3.6, the model constants $T_{s,-}$ and $T_{s,+}$ in the first and second stage solidification have been given two sets of values, following Dreizin *et al.* (81) and Ning *et al.* (28). The Dreizin-based model constants predict a slightly faster cooling after the

equilibrium solidification. This can be due to higher heat loss during the transition stage as the Dreizin-based model constants have a higher $T_{s,+}$. A higher $T_{s,+}$ yields a higher heat loss due to convection and radiation. It is also observed that the Dreizin-based model constants predict a shorter time during solidification. The transition time increases with the increase of d_p, e.g., ∼1–2 ms in D20 and ∼5–10 ms in D80. According to Eq. 3.26, the mass of the solidified L2, Δm_{L_2}, in the first stage solidification predicted using the Dreizin-based model constants is larger than that using the Ning-based model. Consequently, less L2 remains for the second stage of solidification. The transition time is an important indicator for evaluating the performance of model constants. Unfortunately, measurements of the transition time are not available as the end of the equilibrium solidification stage is not distinguishable due to the decrease in the particle radiant intensity.

4.1.3 Summary

The five-stage Fe "Point particle model" developed within the Lagrangian-Eulerian framework is capable of replicating the whole particle burning process. The predicted particle temperature evolution trend is similar to the measured particle radiant intensity. The two phase-change processes are properly captured in the model. In addition, a diffusion-controlled mechanism is identified from the melting stage. The over-prediction of the melting time is also discussed, and possible explanations are proposed. The modeling results of the "super-cooled solidification" are able to explain the observed intensity (temperature) jump.

4.2 Single Al particle combustion: Lagrangian-Eulerian framework

4.2.1 Experimental case setup

The experimental rig is the same as that in the Fe case (Fig. 4.1). The images and the data processing are performed by the collaborators in the metal research lab at Lund University. The pilot flame consists of 22.37% H_2, 38.32% O_2, and 39.31% N_2 (on a volume basis with a total flow rate of 30.53 min/L), which has an equivalence ratio of 0.29. The combustion product is an O_2-rich hot oxidizer gas. The central jet is fed with a H_2 flow to carry the suspended micron-sized Al particles. The flow rate is 0.4 L/min, i.e., a bulk flow velocity of U = 3.53 m/s, following a parabolic velocity distribution within the pipe. The Reynolds number based on the bulk flow velocity and diameter of the fuel pipe is calculated to be 52.

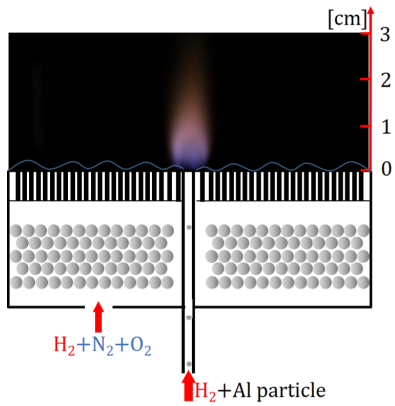

Figure 4.7: Schematic illustration of the experimental rig with the pilot flat flame and a central H_2 jet flame. Figure courtesy of the collaborators in the metal research lab at Lund University.

Figure 4.7 shows a typical background flame in the experiments, which differs from that in the Fe particle combustion experiments. Herein, the central diffusion H_2 flame is visible, while the pilot flame is almost non-visible. This background flame setup can provide a higher temperature to facilitate the melting of the Al_2O_3 shell, as well as a steam environment for the investigation of H_2 production from Al / H_2O reactions.

The amount of particles seeded into the flame can be adjusted by varying the gas flow and the voltage over the capacitor. Figure 4.8 shows the particle size (diameter) distribution determined with SEM. The mean diameter is about 65 μm. Note that the particles smaller than 20 μm are ignored due to the resolution of the high-speed camera.

To characterize the temporal and spatial evolution of the burning particle, shadowgraphy,

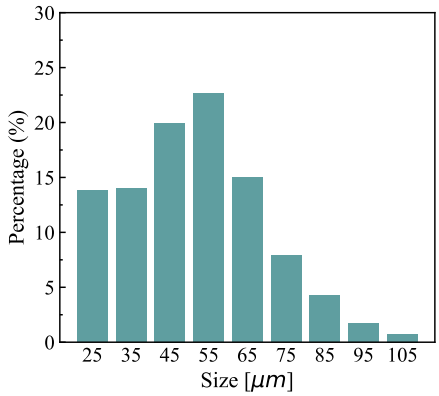

Figure 4.8: Particle size distribution. The horizontal axis shows the mean diameters of the different particle size groups, while the vertical axis indicates the normalized number of particles in a given size group relative to the total number of particles studied.

and direct emission measurements are conducted by the author's collaborators using a high-speed camera (Photron FASTCAM NOVA S16, 1024×1024 pixels, 12 bit) and a long-distance microscope. The camera operates at 16,000 fps and has a spatial resolution of approximately 6 μm/pixel. Shadowgraphy measurements are performed utilizing a continuous wave (CW) laser at 405 nm with an average output of 1.5 W for background illumination. More details about the experimental setup can be found in Paper II.

The computational domain is the same as that shown in Fig. 4.1. The center of the pilot flame is a H_2 jet flame, and the gas flow at the burner exit follows a profile of a fully developed pipe flow since the fuel pipe has a length of 300 mm (194D), much longer than its hydrodynamic entrance length. The $H_2/O_2/N_2$ chemical reaction mechanism of Choi *et al.* (88) is adopted to simulate the central H_2 jet flame and the surrounding pilot flame before injecting the Al particles. The mechanism consists of 20 reactions and 10 species. Detailed transport properties are used to compute the diffusion coefficients (89; 90). To reduce the computational cost, the pilot flame is not coupled with LPT. Considering that the particle feeding rate in the experiments is low, the heat and mass exchange between the particle and the surrounding gas is assumed to have a negligible effect on the gas phase side. The pilot flame is modeled as a hot inflow boundary. At the burner exit, the temperature is set at 1490 K, as measured from experiments. The inflow velocity is set at 0.81 m/s, accounting for the expansion of the hot product gas across the pilot flame.

The "MEM" was initiated by Prof. Bai, and implemented by the author in collaboration with Sheng Feng, based on the previous Fe "Point particle model". The simulations and the analysis of the results were also mainly performed by the author and Sheng Feng, with valuable discussions from all other collaborators.

4.2.2 Ignition data processing

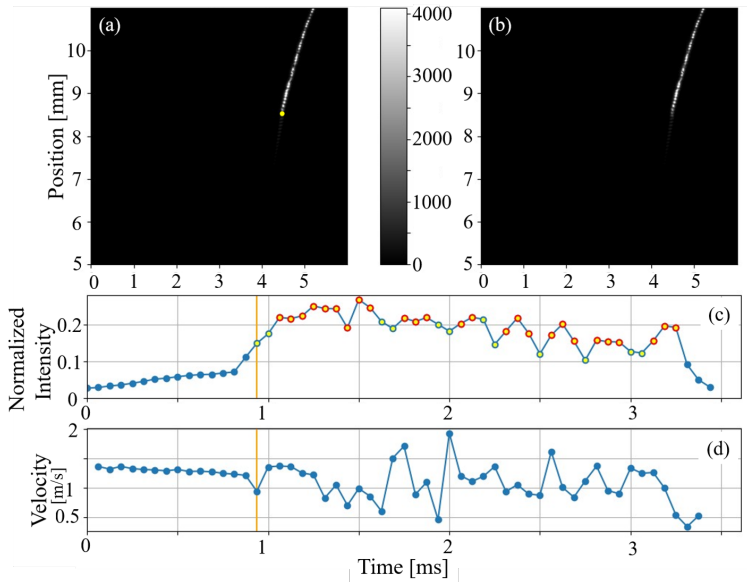

Figure 4.9: Illustration of particle tracking and definition of the ignition point: (a-b) accumulated images from the high-speed camera showing the trajectory of one particle with the marked ignition point in (a); (c) normalized emission intensity from a particle, where the yellow dots represent that the particle is ignited and red dots represent that at least one pixel of the intensity is saturated; (d) particle velocity derived from the particle position. The images and data processing are performed by collaborators from the metal research lab at Lund University.

From the measured emission intensity image, particles were identified and tracked using an in-house algorithm from our collaborators based on the tracking method "4 Frame: Best Estimate" (91). A more detailed description of the processing can be found in Roth *et al.* (92). Generally, the detection can be divided into two steps: (a) identifying the droplet coordinates in the images and (b) extracting the particle positions and velocities using Particle Tracking Velocimetry (PTV). Figure 4.9 shows an example of data processing. The ignition point is determined when the normalized intensity continues to be higher than a threshold (as indicated by the marked yellow dot in Fig. 4.9(a) and the yellow lines in Fig. 4.9(c-d)). During the image analysis process, more than 200 particles were analyzed. It was found that the threshold of 0.12 corresponds to the peak intensity increase gradient during the ignition stage. Therefore, the ignition point is defined at the normalized intensity of 0.12.

The velocity is calculated from the particle coordinates in the two consecutive frames divided by the time interval, i.e., 62.5 µs. It can be observed that the particle velocity undergoes a sudden increase after ignition, e.g., at a time of ∼1 ms. These abrupt changes are likely attributed to the ejection of liquid droplets or the rapid evaporation of the liquid Al core through the holes in the alumina shell. Such mass release can introduce an additional force and lead to an abrupt change in particle trajectory (93). Note that the particle

velocity also exhibits strong fluctuations after ignition. This could be due to the spinning motion of the particles. If the hole through which ejection occurs is not perfectly aligned with the particle trajectory, it can not only induce a change in the particle's trajectory but also impart spinning motion to the particle. Consequently, this spinning motion may lead to instances of acceleration or deceleration. The force induced by ejection is akin to the "rocket force" observed in the pyrolysis of pulverized biomass particles (94; 95).

4.2.3 Modeling results

Combustion stages of the single Al particle

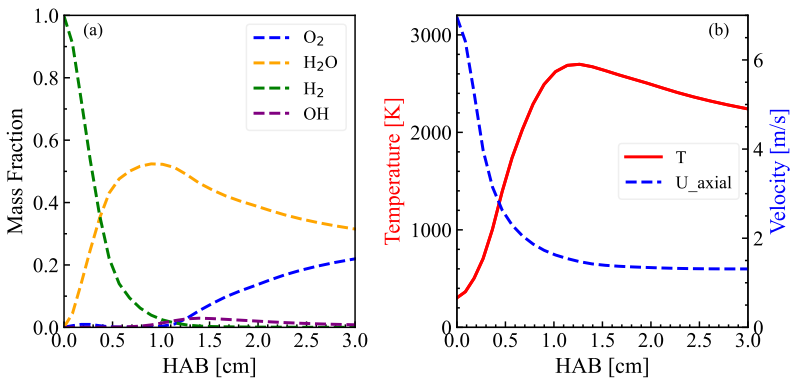

Figure 4.10: Numerically simulated results along the jet center line: (a) mass fractions of O_2, H_2O, H_2, and OH, and (b) temperature and axial velocity of the gas mixture.

Fig. 4.10 displays the predicted mass fractions of H_2, O_2, H_2O, OH, axial velocity of the flow, and temperature along the jet axis. The flow velocity decreases from around 7 m/s to 1.3 m/s along the axial direction due to jet expansion and mixing with ambient gas in the radial direction. The oxygen concentration is nearly zero in the region near the burner exit, i.e., HAB$<$ 12 mm. In this region, the temperature of the gas mixture increases from 300 K to 2100 K, and the oxidizer is mainly H_2O. As will be shown later, this region is critical for the ignition of the particles.

Numerical simulations of micron-sized Al particles in the fuel pipe are conducted to investigate the particle velocity at different radial positions at the burner exit plane. It has been shown that for the micron-sized particles studied in the experiments, the particle velocity is slower than the local gas flow, and their velocity at the exit plane of the fuel pipe is written as

$$U_p = \alpha U_g, \tag{4.1}$$

where U_g is the gas velocity at the exit plane of the fuel pipe, which follows the parabolic profile, i.e.,

$$U_g = 2U(1 - r^2/R^2), \tag{4.2}$$

where U is the bulk flow velocity of the hydrogen jet. R is the radius of the fuel pipe. Particle motion inside the fuel pipe is simulated using Eqs. 2.5 and 2.6 to determine the value of α.

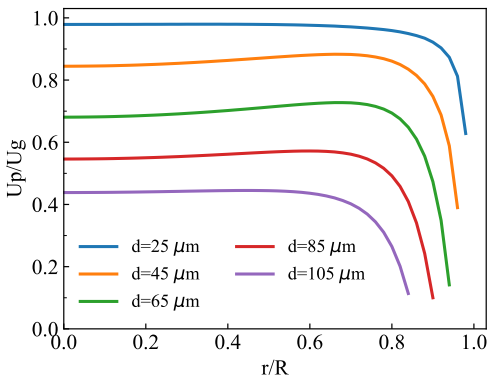

Figure 4.11: Particle velocity at the fuel pipe exit plane normalized with the local flow velocity. The results are from numerical simulations of the flow and particles inside the supplying pipe (~300 mm in length). The initial particle velocity is assumed to be zero at the bottom of the fuel pipe.

Figure 4.11 shows the calculated α under different initial positions and particle sizes. The particle velocity U_p is generally lower than the local gas velocity U_g at the exit plane. For the small particles with a diameter of 25 μm, $U_p \approx 0.98U_g$ close to the pipe central axis. Larger particles tend to deviate more from the local flow velocity. Close to the pipe walls, e.g., $r/R > 0.8$, all particle velocities show a fast decrease and more significant deviation from the local flow velocity. In the Al "Point particle model" simulation, a single particle is placed randomly (assuming uniform distribution) in the burner exit plane, with an initial velocity determined from Eqs. 4.1-4.2.

A typical heating, ignition, and combustion process of a 45 μm diameter Al particle is displayed in Fig. 4.12. The particle position, velocity, temperature, mass, and apparent volume ratio are determined as the particle moves with the gas flow upon its deposition at the jet exit plane at a radial position of $r/R = 0.82$. The initial velocity of the particle is 2 m/s. The simulation only contains combustion stages of solid-phase oxidation, melting, evaporation, and gas-phase oxidation. The computation ends when the particle temperature reaches the Al boiling point. Thereafter, a boiling model is needed to account for the phase change of the Al liquid core, which will be considered in future studies.

The particle undergoes three stages before reaching the point of liquid core boiling. In the

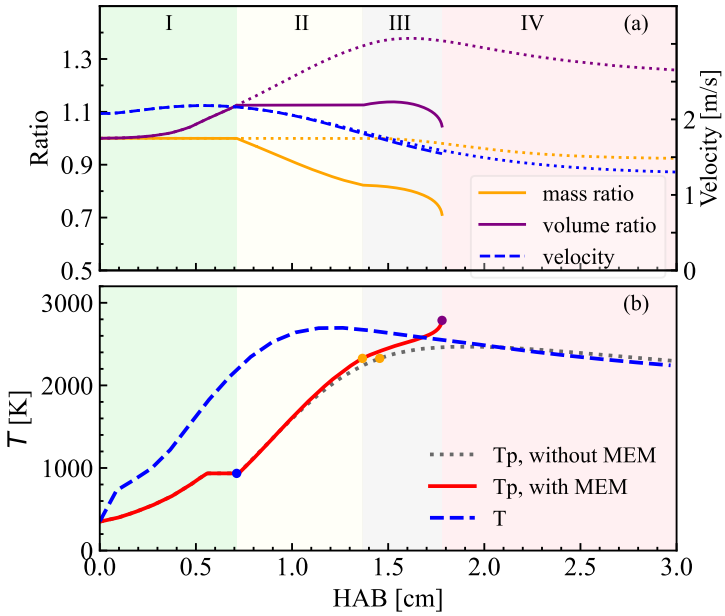

Figure 4.12: Numerically predicted results along the particle vertical position characterized as the Height Above Burner (HAB): (a) particle mass ratio (particle mass normalized with its initial mass), apparent volume ratio (volume held by the Al_2O_3 shell normalized with its initial volume), and velocity; (b) particle temperature with and without "MEM", and the local gas temperature. The Al particle has an initial diameter of 45 μm and a velocity of 2 m/s. The blue dot marks the initiation of ejection. The yellow dot marks the end of the ejection, and the purple dot indicates the boiling point of the Al core. The solid and dashed lines represent results with "MEM", while the dotted lines are those without "MEM". Different particle stages are shown from the plot– Stage I, heating and melting of the solid particle; Stage II, breaking of the aluminum shell and ejection of the liquid Al; Stage III, evaporation of the liquid Al core; and Stage IV, boiling of the Al core.

first stage, the particle is heated by the hot gas. As the temperature increases, the particle density decreases, and the particle volume expands. When the particle temperature reaches the melting temperature of the Al core, phase change occurs, and the particle volume also increases as the density decreases along with melting. The oxide shell breaks after the Al core melts because of the tensile strength built by the thermal expansion of the inner Al core (marked by the blue dot in Fig. 4.12).

In Stage II, the particle mass decreases due to the ejection of liquid Al droplets into the surrounding gas, while the volume of the liquid core remains constant. The released liquid droplets instantaneously evaporate into gaseous aluminum, triggering a reaction between the Al vapor and the oxidizers (O_2 and H_2O) and enhancing the particle heating. During this stage, the gas temperature is higher than the particle temperature ($T > T_p$). The heat release from the gas phase, along with the higher surrounding gas temperature, leads to a faster temperature increase in stage II compared to stage I. When the temperature reaches the melting point of alumina, the alumina shell melts, exposing the inner liquid

Al. Ejection ceases at this point, and the evaporation begins. The particle temperature continues to rise until it reaches the boiling point. The volume of the liquid core increases a little at the beginning of the evaporation stage due to the increase in particle temperature, followed by an eventual decrease in the later evaporation stage. According to the simulation, approximately 18% of the mass is consumed in stage II and 10% in stage III. Thereafter, the remaining particle mass will be consumed during the boiling stage.

If the shell breaking and droplet ejection processes are not considered, as indicated in the dotted lines of Fig. 4.12, the particle volume would increase by 40% during stage II, and the mass of the particle would remain constant. The melting point of the alumina shell is reached further downstream. Since the gas temperature decreases along the downstream direction above an HAB of 1 cm, the particle starts cooling down, and the particle is nearly extinguished, as indicated by the nearly constant mass of the particle in the region HAB $>$ 25 mm. About 8% of the mass is burned for the d_p = 45 μm Al particle. Numerical simulation of larger particles, e.g., d_p = 75 μm, shows that the particle would never reach the melting point of the alumina shell. Ejection stops at about 17 ms, where dT_p/dt = 0. Thereafter, evaporation occurs at the exposed surface of the inner Al liquid as shown in Fig. 3.1 (III). These larger particles are likely the ones exhibiting an eggshell residual structure.

Particle size effects

The effects of particle sizes on the Al particle ignition and combustion processes are shown in Fig. 4.13. All the particles are assumed to have a velocity of 2 m/s to align with the simulation condition in Fig. 4.12. The particle sizes studied are within the experimental size distribution, as shown in Fig. 4.8.

Particles with different sizes undergo different stages at different paces. The smaller particles, i.e., those with a diameter of 25 μm–45 μm, can progress through the four stages discussed earlier. The particle with a diameter of 55 μm reaches the melting point of the alumina shell; however, it does not reach the boiling point of the liquid core. In contrast, the larger particles, with diameters of 75 μm–105 μm, can not reach the melting point of the alumina shell. These particles can exhibit eggshell residual structures as shown in Fig. 3.1.

A smaller particle has a lower heat capacity and is thus heated faster. In the heating stage I, the heating rate increases from about 9×10^4 to 3×10^5 K/s when the particle size decreases from 105 μm to 25 μm. In the ejection stage II, the ejection rate per volume (and mass) is proportional to the heating rate, as per Eq. 3.11. Therefore, smaller particles eject the liquid Al faster, leading to a faster decrease in the mass ratio and the volume ratio. The heat release from the ejected Al vapor, in turn, helps heat the particle to a higher temperature. In the evaporation stage III, the evaporation rate is proportional to the particle size d according

to Eq. 3.16. The heat transfer from the vapor phase reaction, according to Eq. 3.25, is proportional to mass change rate, which, in the case of evaporation, is proportional to particle size. The resulting particle temperature increase is proportional to $1/d^2$. Thus, the smaller particles also undergo a faster temperature increase during the evaporation stage.

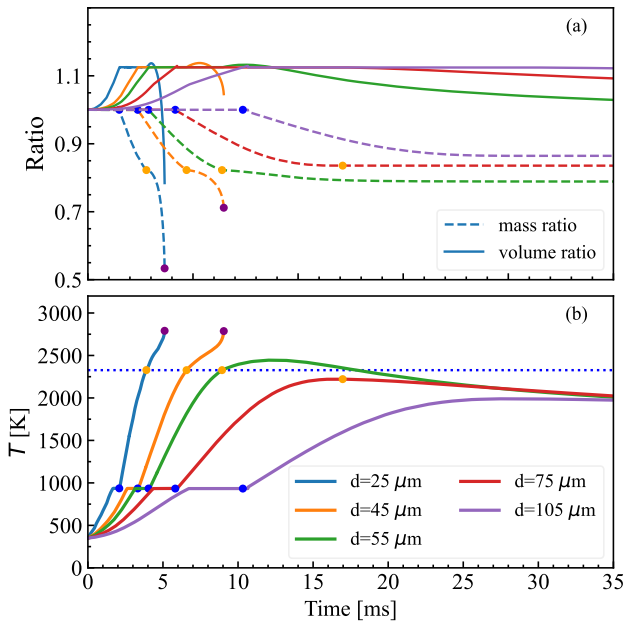

Figure 4.13: Numerically predicted temporal evolution of (a) mass ratio (particle mass normalized with its initial mass) and core volume ratio (volume of the Al core normalized with its initial value), and (b) particle temperature. The particles have initial diameters ranging from 25–105 μm and a velocity of 2 m/s. The dots mark the end points of the different stages as explained in Fig. 4.12.

For the particles reaching the alumina shell melting point, i.e., the 25–55 μm particles, about 18% of the mass is ejected from the particles. In contrast, for the larger particles that do not reach the shell melting point, i.e., particles with a diameter of 75 μm or larger, the ejection lasts longer, and the ejection rate is low during the later stages. This is due to a slow increase or even decrease in the particle temperature in the later time, e.g., $>$ 20 ms. The ejection stops when particle temperature begins to decrease. In the present experimental setup, the high-temperature region is relatively narrow, as shown in Fig. 4.10. The larger particles take a longer time to reach the melting point. Before reaching it, the particles have already passed the hot region and started to cool down.

Ignition Delay Time (IDT) variation

An important parameter characterizing the aluminum particle ignition behavior is the IDT. In the experiments (Fig. 4.9), particle ignition is defined when the normalized intensity is higher than the threshold value of 0.12, after which the intensity profile increases remarkably. Accordingly, ignition in the simulation is defined as the starting point of stage II, i.e., at the beginning of the ejection stage. When the ejection of liquid Al droplets starts, a vapor flame is quickly formed close to the holes of the alumina shell, which gives rise to a rapid increase in emission intensity.

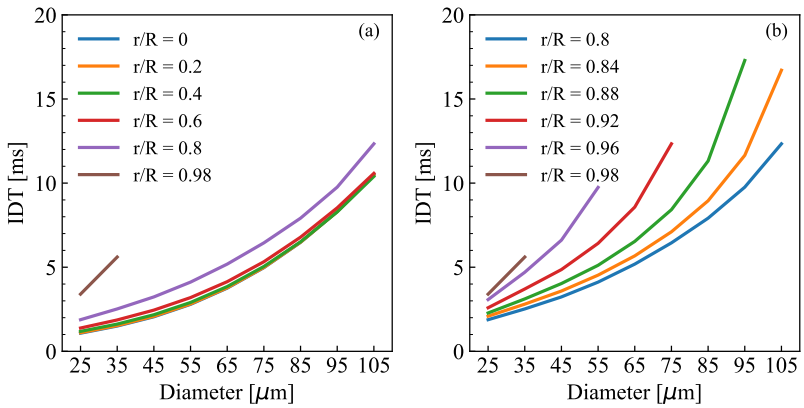

Figure 4.14: IDT variation with Al particle sizes at different initial positions: (a) r/R = 0–0.98 with an interval of ~0.2; (b) a narrower region of r/R = 0.8–0.98 with an interval of 0.04.

Figure 4.14 shows the IDT variation with particle sizes at different initial positions of the jet exit. The IDT increases with the particle size, as already indicated in Fig. 4.13. For the particles close to the center axis ($r/R \leq 0.6$), their IDTs are not sensitive to the particle positions. However, for the particles close to the wall of the fuel pipe, i.e., $r/R > 0.8$, their initial velocities are lower (cf. Eq. 4.1), and the particles have a longer residence time in the near-burner low-temperature region, resulting in a longer IDT.

In Fig. 4.15, the particle positions and velocities at the ignition point are depicted. It is evident that when the particles are located around the center axis ($r/R \leq 0.6$), the particle velocity is about 3–6 m/s. The residence time in the low-temperature region (HAB $<$ 5 mm, cf. Fig. 4.10) is about 1 ms. This residence time is relatively small compared to the IDT. Consequently, the IDT is insensitive to the particle velocity in these cases.

On the other hand, when the particles are located near the wall of the fuel pipe, i.e., r/R = 0.98, the particle velocity is about 1.5 m/s. The corresponding residence time of the particle in the low-temperature region is about 3 ms, explaining the longer IDT and the higher

sensitivity to the initial position of the particles compared to the particles near the center axis. As for the ignition distance (Fig. 4.15(b)), it is important to note that the particle velocities are different at different initial positions due to the fully-developed parabolic velocity profile in the pipe flow. This also leads to a varied ignition distance.

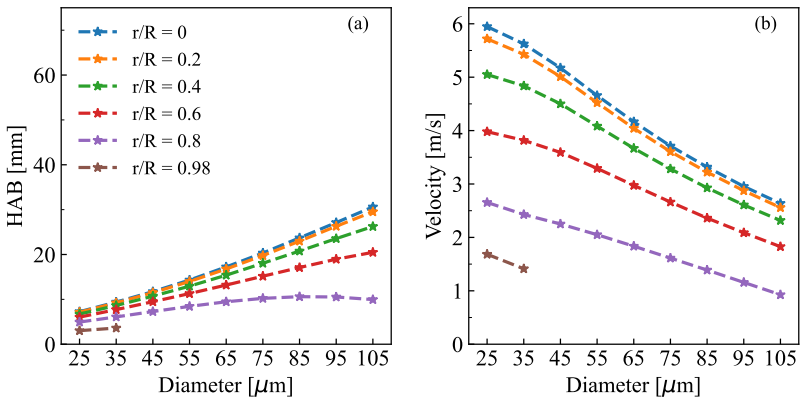

Figure 4.15: Numerically predicted (a) axial positions and (b) velocities of particles at the ignition point for varying particle sizes and initial positions.

With the above understanding of IDT from the simulation, a statistical analysis of the particle axial positions and velocities at the ignition point is conducted. Fig. 4.16 shows the Probability Density Function (PDF) of particle velocity and axial position at the ignition point, based on particles of all sizes and initial radial positions. The data are fitted to a log-normal distribution function.

A similar statistical analysis is performed for the numerically predicted particle position and velocity at the ignition point. The PDF of the particle size is taken from the experiment, as given in Fig. 4.8. The initial particle location at the burner exit plane is assumed to follow a uniform distribution. Combining the ignition height and velocity shown in Fig. 4.15, the PDF of particle size shown in Fig. 4.8, and the initial locations, the PDFs of the particle velocity and height at the ignition point can be calculated. The results are shown in the lower row of Fig. 4.16.

Mean particle heights at ignition are 7.92 mm and 6.95 mm from the experiments and simulations, respectively. The experimental mean particle velocity at ignition is approximately 1.34 m/s, while in simulation, it is approximately 1.54 m/s. The statistical analysis of ignition velocity shows a broader distribution compared to ignition height. The predicted particle height is slightly lower than that in the experiments, while the predicted particle velocity is close. Overall, the current model effectively captures the ignition behavior of the particles.

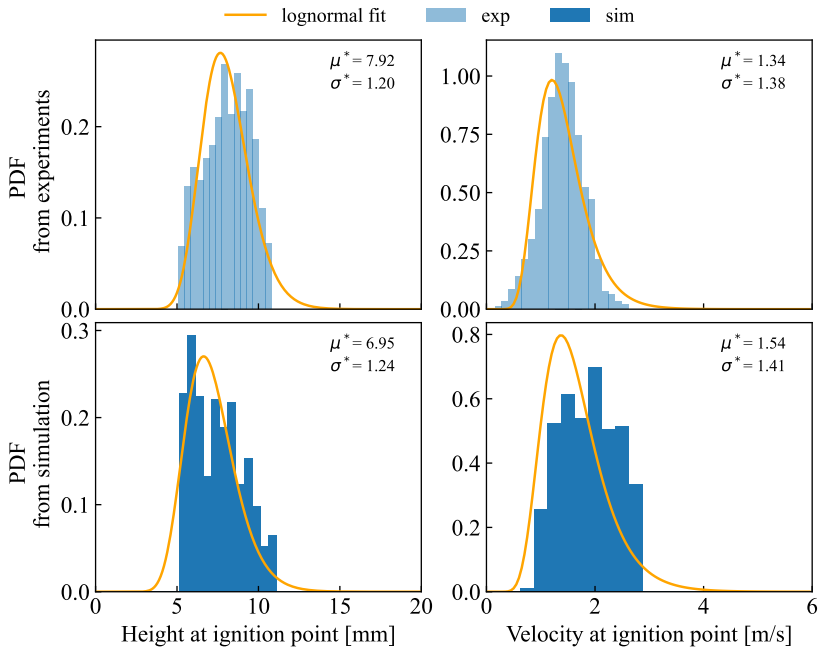

Figure 4.16: PDF of particle axial position (HAB) above the burner and velocity at the ignition points. Upper row: experimental results; lower row: model prediction. μ^* and σ^* denote the mean and standard deviation of velocity and height at the ignition point converted from the lognormal fit, wherein $\mu^* = e^{\mu(x)}$ and $\sigma^* = e^{\sigma(ln(x))}$.

4.2.4 Summary

In this subsection, a metal "Point particle model" for Al has been proposed, focusing on the ignition and combustion stages. The "MEM" proposed in this work is capable of explaining the eggshell-shaped hollow alumina sphere morphology observed with the SEM. The model focuses on the three combustion stages in Al particle combustion: the heating and melting of the solid Al particle, the breaking of the alumina shell and ejection of the liquid Al core, and the evaporation of the liquid Al core until its boiling point. The predicted IDTs agree well with experimentally measured ones. It should be noted that the model is specifically designed for predicting particle combustion within the Lagrangian-Eulerian framework, where the adjacent flame near the individual particle is not resolved. Meanwhile, the assumptions for the "MEM" simulation require stringent validation and further development.

4.3 Single Al particle combustion: Eulerian framework

4.3.1 Experimental case setup

In the experiment, the stable generation of Al droplets of similar sizes is realized by positioning an Al wire orthogonal to the centerline of a modified McKenna burner. More details of the design can refer to collaborators' work in Refs. (21; 22; 23). In the experiment, the burner has a central H_2/O_2 diffusion flame to heat the wire to the melting point of the alumina shell (∼2327 K in Table 1.2). Once the shell melts, the wire breaks, and the Al droplet is generated from the wire due to surface tension, which then moves slowly upward with the flow. In the surroundings, a premixed $H_2/O_2/N_2$ flat flame provides the oxidizing environment for droplet burning.

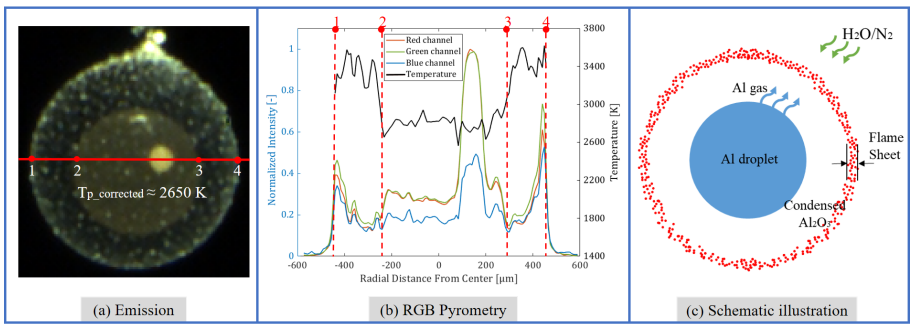

Figure 4.17: Experimental measurement for a burning aluminum droplet by (a) high-speed color imaging and (b) RGB pyrometry (22), together with (c) a schematic illustration of the droplet and the enveloping flame. The droplet radius is 275 μm. The experimental condition is the C1 case in Refs. (22; 23).

Figure 4.17 shows a typical emission and resolved temperature measurement of a steadily burning Al droplet with a radius of 275 μm. The experiments and data processing are performed by the collaborators in the metal research lab at Lund University. The central droplet and the enveloping flame are visualized with high resolution. Based on Fig. 4.17(a), a schematic illustration of a burning Al droplet is demonstrated in Fig. 4.17(c). Due to the surface tension, the Al droplet is spherical. Al continuously evaporates from the surface and reacts with the oxidizer surrounding the droplet, forming a layer of condensed $Al_2O_3(L)$. Important parameters to characterize the droplet evaporation and burning include flame temperature (T_f), flame stand-off ratio (STR, the ratio of the position of the peak temperature over the position of the droplet surface, i.e., R_f/R), and the Stefan flow velocity (v_{st}). With the RGB pyrometry, the droplet surface temperature and flame temperature are measured to be ∼2650 K and ∼3400 K for all the droplet sizes. With the resolved droplet image, the droplet surface and its surrounding flame zone can be anchored to obtain STR. Moreover, the droplet size evolution [m^2/s] can be obtained from the resolved images by fitting to a D^2-law (96). Then the evaporation rate $\dot{\omega}$ can be calculated as per

$\dot{\omega} = d(\rho_l \cdot \pi D^3/6)/dt$, from which v_{st} can be further calculated. These experimental results will be used to validate the "Point particle model" for Al.

The simulation domain is illustrated in Fig. 2.1 in Section 2.1. Detailed numerical simulation of the $H_2/O_2/N_2$ flame shows that during the steady-state burning stage of the droplet, the surrounding temperature and oxidizer concentration can be considered constant at ~2600 K and a composition of 55% H_2O / 45% N_2 by mole, respectively. This information will be used as the oxidizer's initial composition in the current simulation. A fixed droplet surface temperature of 2650 K will also be adopted in the simulation. Three particle sizes with radii of 275, 120, and 55 μm are investigated. Target parameters (T_f, STR, and v_{st}) are computed and compared with the experimental data mentioned above. In the simulation, T_f is taken as the peak value in the temperature profile. STR is taken as the ratio of the position of the peak temperature over the position of the droplet surface (R_f/R). v_{st} is the normal component of the bulk flow velocity $(\vec{u})_s$ in Eq. 3.23.

The size of the computational domain is determined so that there is enough oxidizer to sustain the reaction until the computation ends. As a steady-state solution is pursued, the computation end time is set so that temperature and species profile variation is smaller than 2%. Preliminary grid sensitivity analysis yields a mesh size ~2 μm, which is ~0.036R for the smallest droplet. A grid-independent numerical solution is obtained by adopting different mesh sizes, from 1.5 to 5.5 μm, and simulation results from these meshes overlap for temperature and main species distributions within the investigated region, i.e., the region between the droplet surface and the flame zone. The detailed information on temperature and species distribution in this region can be accurately resolved with the 2 μm mesh size, which is adopted in the following simulations. The implementation of the model, as well as the simulation, were mainly performed by the author.

4.3.2 Modeling results

The resolved flame struture

Figure 4.18 presents the simulation results of temperature, Stefan flow velocity, and species distribution in the vicinity of a steadily burning aluminum droplet with a radius of 275 μm. The oxidizer condition is pure H_2O at 2600 K. The boundary temperature is set constant at 2650 K. Temperature profile starts with a sharp increase from the *Fuel* boundary to peak value, denoted herein as flame temperature T_f, and then gradually decreases due to heat dissipation to the surrounding. The determination of T_f, v_{st}, and STR from the temperature profile is shown in the figure. The velocity is the highest near the boundary and then gradually decreases due to expansion. Species with a maximum mass fraction larger than 3% are plotted in Fig. 4.18(b). The species distribution profile shows a classical diffusion flame structure (97).

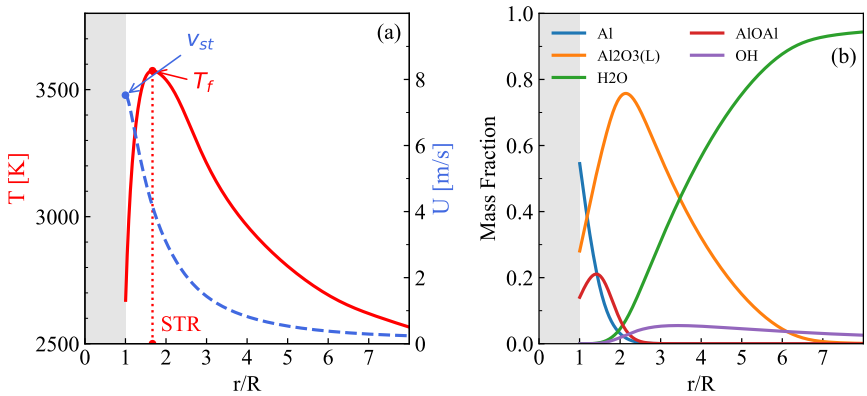

Figure 4.18: Numerically predicted (a) flame temperature T_f, flow velocity, and flame stand-off ratio (STR), and (b) main species distribution along the radial direction of a steadily burning Al droplet. v_{st} in (a) denotes the Stefan flow velocity at the droplet surface. Droplet radius: 275 μm. Oxidizing condition: 2600 K in pure H_2O.

On the *Fuel* side, Al has the highest mass fraction and gradually decreases outwards, while an opposite trend is observed for steam. The main reaction product calculated from the current mechanism is $Al_2O_3(L)$, which has significant concentration over the region and peaks near the flame temperature. Apart from that, AlOAl also has a non-negligible contribution within $3R$ from the surface. OH begins to form after the peak of AlOAl and diffuses quite fast to the surrounding gas. It is interesting to note that the concentration of AlO is negligible in the steam case, although it is often interpreted as a marker for the flame position when oxygen is the oxidizer (31). Other intermediate species include some Al/O/H sub-oxides such as AlH, AlOH, and Al_2O_2. However, their mass fractions are much lower than those plotted in the figure. Meanwhile, due to the species diffusion, products can reach the droplet surface, opening up some possibility for surface reaction or deposition.

Furthermore, although Eq. 3.24 is not implemented in the current model, the first term on the l.h.s and the first term on the r.h.s of the equation can be used to calculate heat fluxes through the *Fuel* boundary. Based on the results from the pure steam case simulation in Fig. 4.18, the evaporation rate $\dot{\omega}$ is calculated to be ∼0.726 kg/m^{2}s from Eq. 3.23. The specific evaporation heat of Al at 2650 K is ∼10.94 MJ/kg; thus, the evaporation heat flux, given by the first term on the r.h.s of Eq. 3.24, is approximately 7.94 MW/m^2. On the other hand, the conductive heat flux transported from the flame zone to the surface is calculated to be ∼2.55 MW/m^2 as per the first term on the l.h.s of Eq. 3.24. It is somewhat surprising to find that the conductive heat only accounts for ∼32% of the heat needed to sustain Al evaporation. Note that the calculated evaporation velocity oscillates between 5 and 10 m/s, which might slightly influence the evaporation heat flux. However, in any case, it is more than twice the conductive heat flux from the flame zone. Meanwhile, the calculation for

the other two droplet sizes shows similar ratios of the heat from the flame zone to that needed for evaporation. This demonstrates that the inclusion of other heat source terms, e.g., radiative heat flux (Q_r) and/or heat flux at droplet surface (Q_s) as shown in Eq. 3.24 are indispensable. The evaporation heat cannot be balanced solely by heat conduction from the flame zone. This imbalance is also observed in the simulation of the experimental C1 case, where approximately 27%, 22%, and 18% of evaporation heat is provided by the heat conduction from the flame for droplet radii of 275, 120, and 55 μm, respectively.

In the simulation, the boundary temperature is fixed at 2650 K based on experimental measurement. A variation of the boundary temperature can lead to a different portion of the heat flux ratio. Table 4.2 lists the simulation results with boundary temperatures between 2350 and 2650 K. The flame temperature and the Stefan flow velocity decrease as the boundary temperature decreases. STR first decreases and then increases as boundary temperature decreases. There is a significant increase in the proportion of the conduction heat over the evaporation heat from 18% at 2650 K to 69% at 2350 K. Further lowering the temperature will reach the solidification/melting point of $Al_2O_3(L)$, which is not physical in that the burning of Al droplet is generally considered to be activated after the melting of the Al_2O_3 coating layer (77; 98). This result reveals that the heat imbalance becomes more significant at a higher surface temperature, suggesting the increasing importance of other heat sources that should be further quantified.

Table 4.2: Predicted flame parameters for varying boundary temperatures under the experiment condition (55% H_2O / 45% N_2 by mole at 2600 K). The droplet radius is 55 μm.

Radius [μm]	T_p [K]	T_f [K]	STR	v_{st} [m/s]	Q_f/Q_{evap} [%]
	2650	3555	2.11	24	18
	2600	3500	1.94	20	26
55	2500	3255	1.86	14	45
	2400	3055	2.68	10	61
	2350	2994	3.06	8	69

Experimental data validation

Table 4.3 allows a comparison between the predicted flame parameters T_f, STR, and v_{st} and the corresponding experimental data. Experimental results find that the surface temperature and flame temperature do not vary much for different droplet sizes under the current ambient hot steam condition. The measured STR shows a moderate decrease with increasing droplet size. The droplet burning rate, which is related to the Stefan flow velocity, decreases with increasing droplet size.

Meanwhile, results from the simulation show that all the predicted values are of the same

order of magnitude as those of the experiments. The flame temperatures deviate less than 5% of the experimental value. The STR and v_{st} of smaller droplets (55 μm radius) agree quite well with experiments, yet larger STR and smaller v_{st} are obtained for larger droplets (radii of 120 and 275 μm). It should be pointed out that the current model simulates the burning of a single Al droplet in a quiescent environment, while in experiments, the droplet is moving together with the surrounding flow. Smaller droplets can follow the flow better. For large droplets, both the diameter and slip velocity are larger, which results in a larger particle Reynolds number and, consequently, a larger Nusselt number to enhance evaporation and droplet burning (96).

Table 4.3: Comparison of key parameters between the experiments and numerical simulation. Oxidizer condition: 55% H_2O / 45% N_2 by mole at 2600 K.

Radius [μm]	Simulation			Experiment			
	T_f [K]	STR	v_{st} [m/s]	T_p [K]	T_f [K]	STR	v_{st} [m/s]
275	3496	2.12	6			1.75	15
120	3545	2.3	10	2650	3400	1.83	20
55	3555	2.11	24			2	26

Particle size effects

It is interesting to note the dependence of flame parameters on droplet sizes. Fig. 4.19 presents the detailed temperature and species profiles for the three droplet sizes. Although the steady-state conditions are modeled separately for three droplet sizes, combining them, the evolution of the droplet burning, i.e., different statuses as the droplet evaporates and shrinks, can be revealed. The predicted flame temperatures do not vary much under three droplet sizes, with a slight increase within 60 K, which agrees with experimental data. The predicted STRs also do not vary much with a slight increase and then decrease as the droplet size increases, while the experiment result shows a slightly decreasing trend of STR as droplet size increases. It is worth noting that in experiments, larger droplets feature a larger slip velocity. This exerts a "stretching" effect on the droplet and its surrounding flame, leading to non-concentricity. Smaller droplets are observed to follow the flow better and are closer to symmetric combustion. Thus, STR is more accurately determined for the smaller droplets. On the contrary, symmetric combustion with no slip velocity is considered in the simulation. In this sense, the case of smaller droplets is closer to the simulation setup, which is also evidenced by the closer alignment of the predicted and the measured STR for the 55 μm radius case. The Stefan flow velocity decreases as droplet size increases, with the predicted values decreasing much faster than those results from the experiment. As per Eq. 3.23, if the boundary temperature were constant, the Al partial pressure at the boundary would also be constant. Considering that the species mass fraction at the boundary is

almost the same, ρ and D will also be almost the same. Then, Stefan flow velocity is almost proportional to the gradient of Al at the boundary. From Fig. 4.19, the Al profiles overlap near the boundary along the normalized radius, which indicates that the actual gradient is almost inversely proportional to the droplet radius. Thus, it is reasonable that the simulated Stefan flow velocity increases as droplet size decreases.

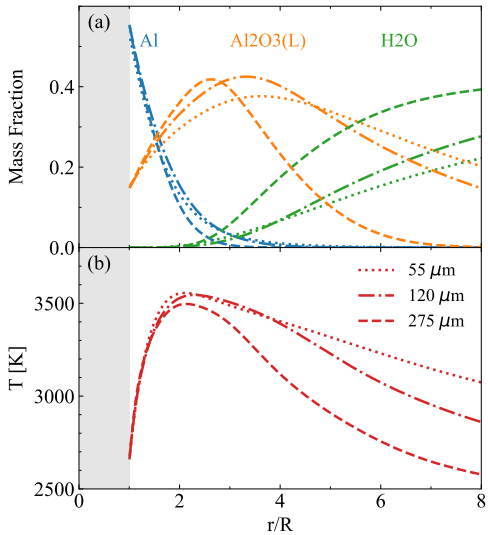

Figure 4.19: Predicted results profiles of (a) species mass fraction and (b) temperature along the normalized radius for different droplet sizes (R = 275, 120, 55 μm) under the experimental condition of C1.

4.3.3 Summary

The single Al combustion model is capable of reproducing the experimentally observed detailed flame structure of a micron-sized Al droplet in hot steam-dominated environments. The numerical model incorporates detailed mass and heat transfer equations between the gas phase and the droplet phase, along with a detailed chemical kinetic mechanism for the Al vapor reaction. The simulated flame exhibits a classical diffusion flame structure close to the droplet, whereas, near the boundary, there is a non-negligible amount of AlOAl apart from the main product $Al_2O_3(L)$. The simulation results show agreeable consistency with experimental data in flame temperature for all the droplet sizes, and the flame stand-off ratio and the Stefan flow velocity for small droplet sizes (radius of 55 μm). Heat flux analysis shows that conduction heat from the flame front accounts for less than 30% of the heat needed in Al evaporation, and the imbalance becomes more significant as droplet surface temperature increases. More detailed investigations into quantifying the terms in the energy conservation equation (Eq. 3.24) can be performed in the future for model development.

4.4 Analysis of Al gas phase kinetics

4.4.1 Selected mechanisms for evaluation

Table 4.4 summarizes the available mechanisms for combustion of gas phase Al in different oxidizers. The current thesis mainly addresses Al combustion with oxygen (air) and steam as oxidizers. Al can also react in other oxidants, e.g., CO_2 and HCl (80), which may provide a fundamental understanding of its general combustion kinetics, and, therefore, will be included in this thesis. For the sake of simplicity, the mechanisms listed here will later be referred to by an identifier composed by the name of the first author(s) or the research group, e.g., "the Catoire mechanism", with no further citations afterward.

For evaluation of the Al / O_2 subset, the Glorian mechanism, the Saba mechanism, and the Starik mechanism are selected. For evaluation of the Al / H_2O subset, the Glorian mechanism, the Storozhev mechanism, and the Starik mechanism are selected. For evaluation of the H_2 / O_2 subset, all the selected mechanisms for the validation of the Al / H_2O subset are included, as well as three other popular detailed H_2 / O_2 mechanisms, namely the ELTE_2015 mechanism (54), the FFCM-1 mechanism (55), and the Konnov_2019 mechanism (56). A more in-depth description of the three detailed H_2 / O_2 mechanisms can refer to Paper V. A brief description of each Al-related mechanism is given below.

Washburn *et al.* (99) presented a "first generation model" of gas phase kinetics for the Al/Cl/O/C/H system, which was applied to the simulation of micron-sized particles burning in steam and then further in oxygen and carbon dioxide (100). The mechanisms partly rely on earlier works by Swihart, Catoire, and co-workers (101; 102; 103). They employed quantum chemistry and transition state theory to determine reaction rate constants and compared them to experiments in a few cases where data were available. An Al / H / C / O kinetic model was proposed based on the calculated rate constants and added to an existing H_2 / O_2 mechanism. The authors of these early mechanisms emphasized the preliminary nature of their calculations and estimates. They called for further experimental and quantum chemistry work to obtain accurate reaction rate constants and, in many cases, to determine whether certain particular reactions would indeed happen at all. Since then, improvements have been made to a few of the chemical reactions, but later models still, to a large extent, rely on these early works.

Glorian *et al.* (80) proposed a coupled gas-surface chemical kinetics based on the Washburn mechanism (99; 100) and the work of Huang *et al.* (82). The surface mechanism includes species in the bulk phase and surface sites, which can react with gaseous species at a rate given by a sticking coefficient. The work resulted in several publications on gas-surface chemical kinetics and thermochemistry of micron-sized particles (40; 80). The oxidizer O_2/Ar is the main focus of his work, but simulations in pure steam, CO, and CO_2 are also

Table 4.4: Al combustion kinetic mechanisms studied in this work

Refs.	Year	Oxidizers	Source of rate constants	Validation range	Comments
Swihart *et al.* (102)	2003	HCl	TST/RRKM/DFT[1]	1500–4000 K, 1–50 atm	Homogeneous combustion
Catoire *et al.* (103)	2003	O_2, CO_2, H_2O	(102; 104; 105; 106; 107; 108)/estimated	1000-−1300 K, 30–200 atm	
Beckstead *et al.* (77; 109)	2005	O_2, CO_2, H_2O	Not stated	Not stated	Global oxidation steps
Washburn *et al.* (99; 100)	2008–2010	H_2O, O_2, CO_2, HCl	Theory/(102; 103; 109)	2300–3200 K, -18 atm	Full Al/Cl/O/C/H chemistry
Starik *et al.* (110; 111; 112)	2012–2014	CH_4, air, H_2O	Theory/(99; 102; 113; 114; 115)	300–2800 K, 1 atm	Nano-size
Glorian *et al.* (40; 80)	2016	O_2, CO_2, CO, H_2O	(99; 102; 103)	1–10 atm, 1–400 μm	Micron-size
Saba *et al.* (116; 117)	2021	CO_2	VTST/RRKM/DFT[2]	1 atm	
Storozhev *et al.* (118; 119; 120; 121; 122)	2014–2021	H_2O	Exp./Theory/data evaluation	1 atm	Nano-size

[1] TST: Transition State Theory. RRKM: Rice Ramsperger Kassel Marcus. DFT: Density Functional Theory.
[2] VTST: Variational Transition State Theory.

conducted and discussed. The Glorian mechanism has been implemented in several later modeling works, including one recently published by Hu *et al.* (123).

Saba *et al.* (116; 117) performed quantum chemistry calculations to investigate the possible Al_xO_y species along with the reaction pathways. Density Functional Theory (DFT) level calculation was applied to search intermediates and transition states, and the CBS–QB3 method was applied to accurately calculate potential energies. For the estimation of the reaction rate coefficients, Variational Transition State Theory (VTST) and unimolecular reaction theory were adopted for the elementary reactions. The Rice-Ramsperger-Kassel-Marcus (RRKM) theory was applied to calculate the microscopic reaction rates. Reaction mechanisms of the Al/O_2 and Al/CO_2 systems were proposed. A special feature of the mechanism is that the authors treated the condensation process as a dimerization process from sub-oxides to form gaseous large intermediates of Al_2O_4, Al_4O_6, and Al_8O_{12}. This way, multi-phase complexity is relaxed, and pure gas phase reaction simulation can be performed.

Storozhev and Yermakov published a series of articles developing both physical and chemical models for Al nano-particle combustion in steam (118; 119; 120; 121; 122), including the effect of O_2 addition (121). The gas phase mechanisms consist of explicitly given forward and backward reactions. An important part of their work is the inclusion of a physiochemical model to describe the condensation of alumina oxides whose fate can involve adsorption/condensation on the original particle as an oxide cap or formation of new particles in the flame zone (120; 122).

Starik *et al.* (111; 112; 124) conducted a comprehensive theoretical study on the reaction scheme of the Al/CH_4/air and Al/H_2O systems. These studies are partly driven by the challenges met in improving hydrocarbon fuel combustion by adding some amounts of nano-sized Al particles. The oxidation of Al gas proceeds very rapidly, much faster than the oxidation of saturated hydrocarbons. The potential energy surfaces of the elementary reactions with Al-containing species were calculated by quantum chemical studies, and the rate constants of the corresponding reaction channels were estimated. They also calculated the thermodynamic and transport properties of some of the Al-containing species. For the condensation, the authors initially adopted the partial equilibrium phase change equation of Huang *et al.* (82) but later also investigated possible physiochemical models of homogeneous and non-homogeneous nucleation.

The above-mentioned mechanisms are scrutinized according to the mechanism analysis structure presented in Section 2.3. The analysis of the elementary reaction analysis is not included in this thesis, and only the analysis of the global performance in the "Boundary layer resolved model" and a reaction pathway analysis for the Al/H_2O system are summarized and discussed herein. More detailed descriptions of the model setup can refer to Paper III and mechanism analysis results can refer to Paper IV. The simulation settings

are provided in Table 2.1 in Section 2.3. Dr. Nilsson conceptualized this subproject. The experiment data for the steam case were provided by collaborators (22; 23) and for the air case by literature (32). The review and analysis, together with the simulations, were mainly performed by the author.

4.4.2 Modeling results

Al / O_2 subset

Figure 4.20 presents the modeling results for validation of the Al / O_2 subset based on the experiment of the air case. The simulation condition is set at 300 K and 1 atm with an Al droplet surface temperature of ~2400 K. The measured peak temperature, i.e., the flame temperature T_f, is ~3500 K shown as a plateau between a normalized radius of 3.5–4.5, denoting the flame zone (32).

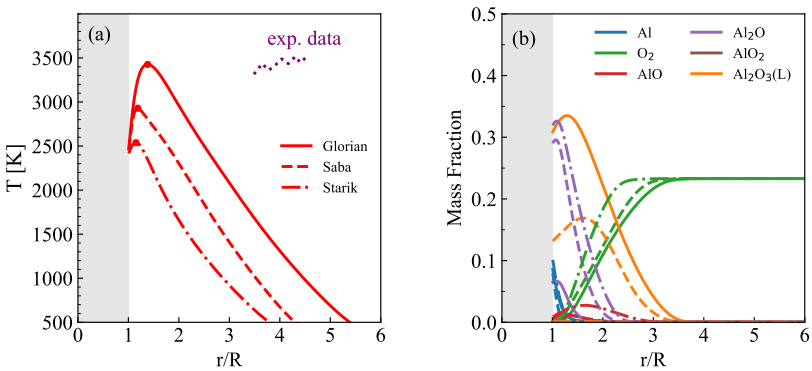

Figure 4.20: Performances of different mechanisms in modeling the (a) temperature profile and (b) main species mass fraction profiles for the air case. Solid line: the Glorian mechanism; dashed line: the Saba mechanism; dash-dotted line: the Starik mechanism. Note that the Al_2O_3(L) profile from the Saba mechanism refers to the total mass fraction of polymerized Al_2O_3 including Al_2O_4, Al_4O_6, and Al_8O_{12}. The red dots mark the simulated T_f, and the purple dotted line marks the experimentally observed peak temperature plateau from Bucher *et al.* (32).

Comparing the simulation results from different mechanisms, it is found that the predicted temperature and main species profiles are similar in general. Nevertheless, obvious differences in magnitude can be observed. As for the temperature profile, the Glorian mechanism predicts the highest flame temperature at ~3500 K, followed by the Saba mechanism at ~3000 K, and the Starik mechanism at ~2550 K. The Glorian mechanism predicts a flame temperature much closer to the experiment data. The value of flame temperature is closely related to heat release, wherein the "condensation" reaction plays an important role via either the one-step reaction forming "Al_2O_3(L)" or multi-step reactions forming polymerized Al_2O_3. In that sense, the concentration of Al_2O_3(L) can be correlated with

flame temperature, as is supported in Fig. 4.20(b). The positions of the flame temperature predicted from different mechanisms are close and lie between 1–1.5. This is not the case for the experiments where a peak temperature plateau was observed. This can probably be due to the simulation setting or the experimental uncertainty, especially when the condensed nano-sized Al_2O_3 layer is present.

A closer look at the species profile in Fig. 4.20(b) can provide more insight into the reaction progress predicted by the different mechanisms. Al is consumed faster in the Saba mechanism than the other two mechanisms, which can be attributed to the higher initiation reaction rates of Al + O_2, as shown in Section 4.1 of Paper IV. Different from the trend of Al, O_2 is consumed faster with a thinner flame zone in the Starik mechanism than the other two mechanisms, probably due to an earlier termination of the reaction progress when Al_2O is formed. It seems that Al_2O in the Starik mechanism tends to accumulate without advancing to Al_2O_3(L), leading to an almost negligible fraction of Al_2O_3(L). The AlxOy-related reaction sets in the Starik mechanism are combinations of the authors' theoretical calculations and those from the Glorian mechanism. For reactions of AlO + O = AlO_2 and those forming Al_2O_2, the Starik mechanism adopts a TROE-type reaction rate constant expression, leading to smaller rate constants than those in the Glorian mechanism. For the reaction AlO + O_2 = AlO_2 + O, its rate constant in the Starik mechanism is obtained by quantum chemistry calculation and is also lower than that in the Glorian mechanism. The condensation reaction step is reversible in the Starik mechanism, and its rate constant is one order of magnitude smaller than that of the Glorian mechanism. Overall, all the above reasons lead to a slower reaction progress in the Starik mechanism compared to the Glorian mechanism. It is also shown in Fig. 4.20(b) that the peaks of different species profiles occur at distinct positions, indicating a deviation from the classical flame sheet structure (97). The relative peak position goes from that of the Al-rich oxide species to the Al-lean oxide species, i.e., from Al_2O to AlO, and then to Al_2O_3(L).

Al / H_2O subset

Figure 4.21 shows the simulation results of the Al / H_2O system using different mechanisms. The simulation condition is the steam case (droplet surface temperature of 2650 K with the oxidizer being H_2O at 2000 K and 1 atm) similar to the experiment of Wu *et al.* (22; 23). In those experimental works, the Al droplet was burned in the post-flame of a H_2 diffusion flame surrounded by a flat flame (cf. setup in Fig. 4.7). The products were estimated to be 55% H_2O in N_2 by mole. The droplet temperature and flame temperature were measured to be ∼2650 K and 3400 K, respectively. The STR was measured to be 2. Since the concentration of H_2O in experiments is diluted, direct comparison is not available. However, the predicted flame temperature and STR from different mechanisms are still of comparable magnitude to experiment data. The predicted flame temperature

profiles from different mechanisms are similar in general. The Glorian mechanism and the Storozhev mechanism predict quite close values, and they are ~250 K higher than that of the Starik mechanism, especially at the flame zone and post-flame zone. The STRs predicted from the three mechanism sets are also close to each other, with that of the Starik mechanism being closer to the droplet than the other two mechanisms. Compared with the air case, the model predicts STRs in the steam case better. The predicted mass fractions of Al_2O_3(L) and H_2 follow the same trend as that of the temperature profile, wherein the mass fraction of Al_2O_3(L) varies more. The Starik mechanism predicts less than half of the mass fraction of Al_2O_3(L) compared to that of the Glorian mechanism and the Storozhev mechanism, which can probably be due to similar reasons as discussed in the modeling results of the Al/O_2 subset. The Al atom accumulates in Al_2O and AlO, indicating less complete reaction progress in the Starik mechanism. It is also noteworthy that the Glorian mechanism predicts a negligible fraction of AlOH compared to that of AlO. In contrast, the other three mechanisms predict a comparable or even higher fraction of AlOH than AlO. This difference is further discussed in Paper V.

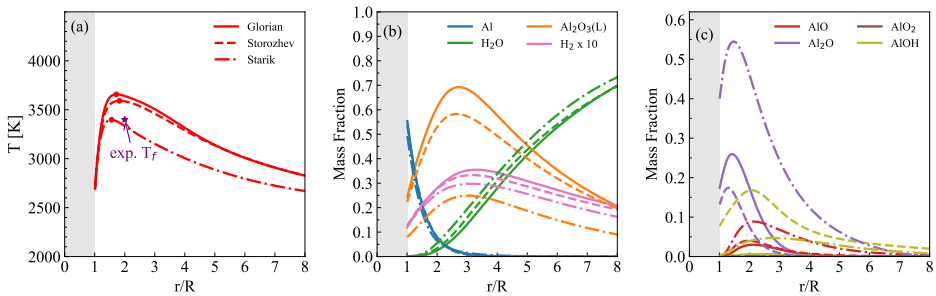

Figure 4.21: Performance of different mechanisms in modeling (a) the temperature profile and (b, c) the main species mass fraction profiles in the steam case (droplet surface temperature of 2650 K with the oxidizer being H_2O at 2000 K and 1 atm). Solid line: the Glorian mechanism; dashed line: the Storozhev mechanism; dash-dotted line: the Starik mechanism. The red dots mark the simulated T_f and the purple star marks the experimentally measured T_f from Wu *et al.* (22; 23).

Figure 4.22 presents the reaction pathway analysis, which helps unveil more details in the reaction system. At an initial condition of 2500 K, 1 atm, and an equivalence ratio of 1, the three mechanisms behave differently. The Glorian mechanism favors the formation of AlO from the initiation reaction Al + H_2O, which then leads to a reaction path similar to that of the Al/ O_2 system. The role of AlOH is almost negligible in the reaction progress. On the other hand, the Starik mechanism only includes the pathway of Al + H_2O = AlOH + H without considering Al + H_2O = AlO + H_2, leading to a much larger formation of AlOH. This can be one explanation for the lower mass fraction of AlOH than AlO seen in Fig. 4.21(b). Moreover, the concentrations of AlOH can serve as a method to assess the Glorian mechanism and the Starik mechanism, if it can be quantified by experiments. The additional Al(OH)x reaction set in the Starik mechanism also contributes to another

pathway after AlOH, although their concentrations are trivial in the system. Meanwhile, a small fraction (∼2%) of Al will form AlH which then reacts back to form Al, and slows down the reaction progress. For the Storozhev mechanism at the selected time point, it seems that the initiation reaction Al + H_2O = AlOH + H is still dominant, and the system is trying to balance between AlOH and Al. Simulation shows that the main compositions of the system include H_2O, Al, AlOH, and H, where the mole fractions of Al and AlOH are very close. This indicates that further reaction pathways in the Storozhev mechanism have not been activated yet.

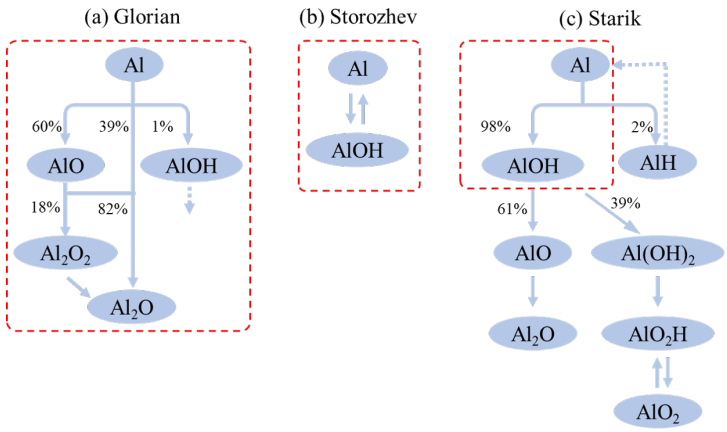

Figure 4.22: Reaction Pathway Analysis (RPA) of the homogeneous Al/H_2O system at 2500 K, 1 atm, and an equivalence ratio of 1 from (a) the Glorian mechanism, (b) the Storozhev mechanism, and (c) the Starik mechanism. The simulation is performed in a Chemkin 0-D homogeneous batch reactor with "constrain pressure and solve energy equation". The reaction pathways are plotted when ∼50% Al is consumed. The reaction progress without any numbers aside indicates an almost exclusive pathway. The red box outlines the main Al-related species at the selected time point.

The Glorian mechanism and the Starik mechanism both include the O_2 and H_2O sub-mechanisms. If we compare different oxidizers, the Glorian mechanism almost has the same reaction pathway for both oxidizers, while a distinct difference can be observed in the Starik mechanism where Al(OH)x reaction set plays an important role in the H_2O part. To the authors' knowledge, the Al(OH)x species has only been theoretically studied, more experimental measurements would be favored to validate the Starik mechanism and the Glorian mechanism.

H_2 / O_2 subset

Figure 4.23 shows the simulation results for the steam case integrated with the H_2 / O_2 subsets from other Al mechanisms as well as the detailed H_2 / O_2 mechanisms. The temperature and main Al-related species profiles from different H_2 / O_2 subsets are almost identical under the simulated condition. The profiles of consumed H_2O and produced H_2 are indistinguishable from the plot. The only difference is the mass fraction of OH after its

peak position, where the Konnov_2019 mechanism has almost the same prediction as the FFCM-1 mechanism, ~10% higher than the ELTE_2015 mechanism, and ~20% higher than the Glorian mechanism. The predicted mass fraction of OH from the Starik mechanism and the Storozhev mechanism are close, and they agree well with those from the FFCM-1 and the ELTE_2015. However, the absolute value of OH mass fractions is very small, being less than 5%. This difference is not reflected in the global temperature profile or the main species profiles. In this regard, the more compact version of the H_2 / O_2 subset in the Glorian mechanism, the Storozhev mechanism, and the Starik mechanism are all valid.

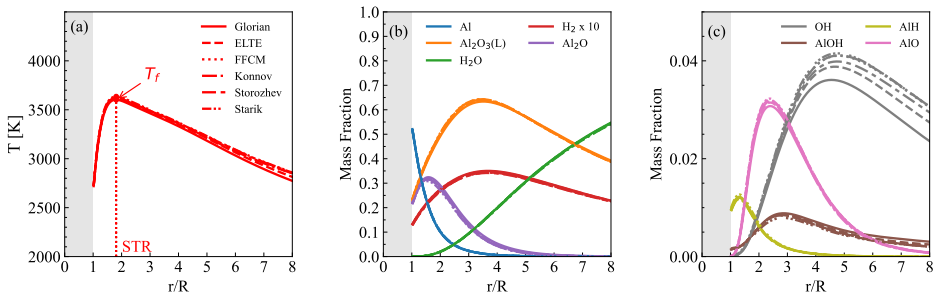

Figure 4.23: Performances of different H_2 / O_2 mechanisms in modeling (a) the temperature profile and (b, c) the mass fraction profiles of key species. The droplet surface temperature is 2650 K, and the oxidizer is H_2O at 2000 K and 1 atm. The Al-related reactions are taken from the Glorian mechanism. The H_2 / O_2 subset is adopted from the Glorian mechanism, the Storozhev mechanism, the Starik mechanism, and three other detailed mechanisms. Solid line: the Glorian H_2 / O_2 subset; dashed line: the ELTE_2015 mechanism; dotted line: the FFCM-1 mechanism; dash-dotted line: the Konnov_2019 mechanism; the long-short-dashed line: the Storozhev mechanism; the dash-dot-dotted line: the Starik mechanism.

4.4.3 Summary

A comprehensive review and analysis of the Al gas phase kinetic mechanism is performed. First, a list of available mechanisms from open literature is provided in Table 4.4. Further analysis of these mechanisms leads to the division of the Al / O_2 / H_2O system into three subsets: the Al / O_2 subset, the H_2 / O_2 subset, and the Al / H_2O subset. Analysis on both the elementary reaction level and the global mechanism level is performed. Key elementary reactions and their rate constants from both available experiment data and theoretical analysis are reviewed for each subset (not presented here, but in Paper IV). Thereafter, the various mechanisms are evaluated in the numerical simulation of the combustion of a liquid Al droplet in both the air case and the steam case. Agreeable results have been found. The general reaction pathways in the steam case are different in different mechanisms, which requires further experimental validations. The H_2 / O_2 subsets in different mechanisms have little effect on the predicted flame structure, and they are almost identical to the results with detailed H_2 / O_2 mechanisms.

Chapter 5

Conclusion and future work

5.1 Conclusion

This thesis aims to deepen the understanding of single metal particle combustion from chemical kinetics and modeling perspectives. Conducted within the framework of a collaborative project integrating experiments, kinetics, and modeling, this work seeks to develop a generalized combustion model for single metal particles, with Fe and Al as the target fuels. Various physical and chemical sub-stages are considered, including solid-phase oxidation, melting, liquid-phase oxidation, evaporation, gas-phase oxidation, and solidification/condensation.

Two models are proposed in this thesis, with each describing a different aspect of the metal particle combustion process: the metal "Point particle model" within the Lagrangian-Eulerian framework and the "Boundary layer resolved model" within the Eulerian framework. This thesis also provides a comprehensive review and analysis of Al gas phase kinetics considering that Al combustion is vapor phase reaction dominated. The main conclusions are outlined as follows:

1. For Fe single particle combustion, the metal "Point particle model" focuses on the five sub-stages, including solid-phase oxidation, melting, liquid-phase oxidation, cooling, and solidification. The model is capable of predicting the whole burning process in consistency with experimental data. The predicted particle temperature evolution trend is similar to the measured particle radiant intensity. Two phase-change processes are captured in the model. In addition, a diffusion-controlled mechanism is identified from the melting sub-stage. The over-prediction of the melting time is also discussed, and possible explanations are presented. The proposed

conjecture of "super-cooled solidification" explains the experimentally observed intensity (temperature) jump.

2. For Al single particle combustion in the metal "Point particle model", the focus is on the four sub-stages: solid-phase heating, melting, evaporation, and gas-phase oxidation. An RHR model is proposed to capture the heat flux transporting to the particle surface from the surrounding flame zone. A special pre-ignition phenomenon is addressed with the conjecture of "MEM". The model is capable of explaining the eggshell-shaped hollow alumina sphere morphology from the SEM images. The predicted IDT statistics agree well with experimental measurements. The effects of particle size and initial position on the particle position and velocity at the ignition point are also discussed. It is found that particles with a larger diameter and an initial position closer to the wall are heated up more slowly and are ignited at a higher position and lower velocity (longer IDT).

3. For Al single particle combustion, the "Boundary layer resolved model" characterizes the detailed flame structure of a micron-sized Al droplet in hot steam-dominated environments. The numerical model incorporates detailed mass and heat transfer between the gas phase and droplet phase, along with a detailed chemical kinetic mechanism. The simulated flame exhibits a similar structure to a classical diffusion flame. Nevertheless, near the boundary, there is a non-negligible amount of AlOAl apart from the main product $Al_2O_3(L)$. Agreeable consistency between the experiment and the simulation is observed in flame temperature for all the droplet sizes, and in the flame stand-off ratio and the Stefan flow velocity for the small droplet size (radius of 55 μm). Heat flux analysis shows that conduction heat from the flame zone accounts for less than 30% of the heat needed to sustain Al evaporation, and this imbalance becomes more significant as droplet surface temperature increases.

4. Based on the "Boundary layer resolved model", a comprehensive review and analysis is performed for the Al / O_2 / H_2O gas phase kinetic mechanism. After reviewing the various mechanisms from the literature, the mechanism is divided into three subsets: the Al / O_2 subset, the H_2 / O_2 subset, and the Al / H_2O subset. Analysis on both the elementary reaction level and the global mechanism level is performed. For the Al / O_2 case, the Glorian mechanism generally predicts a higher temperature profile and more complete conversion of Al to Al_2O_3(L) than the Saba mechanism, followed by the Starik mechanism. The Glorian mechanism also predicts a flame temperature closest to the experimental data. For the Al / H_2O case, the Glorian mechanism predicts a higher temperature profile than the Storozhev mechanism, followed by the Starik mechanism. The general reaction pathways in the steam case are different in different mechanisms, which requires further experimental validations. The H_2 / O_2 subsets in different mechanisms have little effect on the predicted flame structure, and they are almost identical to the results with detailed H_2 / O_2 mechanisms. It is

hoped that this information can serve as a foundation for chemical kinetic modelers to improve further and optimize the gas phase mechanism and for CFD modelers to choose a proper mechanism.

5.2 Future work

Based on the current results, future work can be made regarding model improvements and application extension. Some points are listed below for consideration:

1. For Fe single particle combustion, evaporation followed by gas phase reaction and nano-oxide formation has already been observed from experiments (19; 35; 36). Still, their contribution to the whole burning process is uncertain. In the future, the evaporation and gas-phase reaction sub-stages can be incorporated into the current Fe "Point particle model" to investigate the effects of evaporation on the particle temperature evolution and the characteristic burning times.

2. For Al single particle combustion, the main combustion stage occurs after the melting of the Al_2O_3 layer. However, the ignition of Al particles is also essential for real applications. In the future, the solid-phase oxidation sub-stage, as described in Section 3.1.2, can be incorporated into the model to investigate the solid-phase oxidation and ignition of single Al particles in more detail. This will also provide valuable information for experimental studies.

3. For Al single particle combustion, the current Al "Point particle model" terminates as the Al particle reaches its boiling point. The model can be extended to include the boiling sub-stage, where the boiling rate needs to be quantified. Note that special phenomena can shorten the burning time during the boiling sub-stage, e.g., collision followed by fragmentation (22). Characterizing the underlying mechanisms would be helpful to improve the Al "Point particle model".

4. For Al single particle combustion, the current "Boundary layer resolved model" does not solve the energy conservation equation due to a lack of information on other heat sources. Future works can include quantifying the contribution of different heat sources, e.g., radiation and heterogeneous surface reaction. In this way, the steady-state burning of Al metal droplets can be solved solely based on the input from the surrounding oxidizer temperature and composition.

5. For the Al gas phase kinetic analysis, the condensation reaction step is currently modeled as a simplified one-step reaction with a large pre-exponent factor and ZERO activation energy. This condensation sub-stage can be further explored to include more physical processes.

References

[1] Naturvårdsverket. Sweden's climate act and climate policy framework [online] (2024). Accessed: 2024-12-29.

[2] Panorama. Panorama–visualizing one pathway for Sweden's climate transition [online] (2024). Accessed: 2024-12-29.

[3] A. Boretti, Towards hydrogen gas turbine engines aviation: A review of production, infrastructure, storage, aircraft design and combustion technologies, International Journal of Hydrogen Energy 88 (2024) 279–288.

[4] H. Goyal, P. Jones, A. Bajwa, et al., Design trends and challenges in hydrogen direct injection (H_2DI) internal combustion engines – A review, International Journal of Hydrogen Energy 86 (2024) 1179–1194.

[5] A. Valera-Medina, H. Xiao, M. Owen-Jones, et al., Ammonia for power, Progress in Energy and Combustion Science 69 (2018) 63–102.

[6] Y. Kojima, M. Yamaguchi, Ammonia as a hydrogen energy carrier, International Journal of Hydrogen Energy 47 (54) (2022) 22832–22839.

[7] P. Su-Ungkavatin, L. Tiruta-Barna, L. Hamelin, Biofuels, electrofuels, electric or hydrogen?: A review of current and emerging sustainable aviation systems, Progress in Energy and Combustion Science 96 (2023) 101073.

[8] K. A. Trowell, S. Goroshin, D. L. Frost, et al., Aluminum and its role as a recyclable, sustainable carrier of renewable energy, Applied Energy 275 (2020) 115112.

[9] J. M. Bergthorson, S. Goroshin, M. J. Soo, et al., Direct combustion of recyclable metal fuels for zero-carbon heat and power, Applied Energy 160 (2015) 368–382.

[10] W. Prasidha, M. Baigmohammadi, Y. Shoshin, et al., Towards an efficient metal energy carrier for zero-emission heating and power: Iron powder combustion, Combustion and Flame 268 (2024) 113655.

[11] U.S. Geological Survey, Mineral Commodity Summaries 2024, Tech. Rep., National Minerals Information Center (2024).

[12] M. Baigmohammadi, W. Prasidha, N. C. Stevens, et al., Towards utilization of iron powders for heating and power, Applications in Energy and Combustion Science 13 (2023) 100116.

[13] P. Debiagi, R. C. Rocha, A. Scholtissek, et al., Iron as a sustainable chemical carrier of renewable energy: Analysis of opportunities and challenges for retrofitting coal-fired power plants, Renewable and Sustainable Energy Reviews 165 (2022) 112579.

[14] Eindhoven University of Technology (TU/e). TU/e demonstrates iron fuel at brewery Bavaria: A new circular and CO_2-free fuel for the industry [online] (2020). Accessed: 2024-12-29.

[15] Eindhoven University of Technology (TU/e). Big step toward commercializing iron power [online] (2024). Accessed: 2024-12-29.

[16] M. Y. Haller, D. Amstad, M. Dudita, et al., Combined heat and power production based on renewable aluminium-water reaction, Renewable Energy 174 (2021) 879–893.

[17] M. Milani, L. Montorsi, F. Paltrinieri, et al., Experimental and numerical analysis of the combustor for a cogeneration system based on the aluminum/water reaction, Energy Conversion and Management 87 (2014) 1291–1296.

[18] M. Trogen Pahlén. Replacing fossil fuels with metals | Knut and Alice Wallenberg Foundation [online] (2021). Accessed: 2025-01-12.

[19] S. Li, J. Huang, W. Weng, et al., Ignition and combustion behavior of single micron-sized iron particle in hot gas flow, Combustion and Flame 241 (2022) 112099.

[20] J. Huang, S. Li, D. Sanned, et al., A detailed study on the micro-explosion of burning iron particles in hot oxidizing environments, Combustion and Flame (2021) 111755.

[21] C. Ruan, Z. Wu, M. Stiti, et al., Combustion of micron-sized Al-Mg alloy wires in hot $H_2O/O_2/N_2$ flows, Fuel 357 (2024) 129719.

[22] Z. Wu, C. Ruan, M. Stiti, et al., Spatiotemporally resolved surface temperature measurement of aluminum ignition and combustion in steam and oxygenated environments, Combustion and Flame 264 (2024) 113446.

[23] Z. Wu, C. Ruan, Y. Qiu, et al., Flame structure of single aluminum droplets burning in hot steam-dominated flows, Combustion and Flame 271 (2025) 113838.

[24] C. Ruan, Z. Wu, J. Sun, et al., Ignition, stabilization and particle-particle collision in lifted aluminum particle cloud flames, Proceedings of the Combustion Institute 40 (1) (2024) 105596.

[25] N. Jüngst, Z. Wu, C. Ruan, et al., Light extinction and scattering to determine nanoparticle formation rates during droplet jetting in aluminum dust flames, Powder Technology 453 (2025) 120633.

[26] I. Glassman, Metal Combustion Process, Tech. Rep. 473, Aeronautical Engineering Lab, Princeton Univ., NJ (1959).

[27] I. Glassman, R. A. Yetter, N. G. Glumac, Combustion, 5th Edition, Academic Press, Boston, MA, 2015, pp. 477–536.

[28] D. Ning, Y. Shoshin, M. van Stiphout, et al., Temperature and phase transitions of laser-ignited single iron particle, Combustion and Flame 236 (2022) 111801.

[29] J. Hameete, M. S. Abdallah, L. C. Thijs, et al., Particle-resolved hyperspectral pyrometry of metal particles, Combustion and Flame 264 (2024) 113435.

[30] M. Bidabadi, M. Mafi, Analytical modeling of combustion of a single iron particle burning in the gaseous oxidizing medium, Proceedings of the Institution of Mechanical Engineers, Part C: Journal of Mechanical Engineering Science 227 (5) (2013) 1006–1021.

[31] P. Bucher, R. A. Yetter, F. L. Dryer, et al., Flames structure measurement of single, isolated aluminum particles burning in air, Symposium (International) on Combustion 26 (2) (1996) 1899–1908.

[32] P. Bucher, R. A. Yetter, F. L. Dryer, et al., PLIF species and ratiometric temperature measurements of aluminum particle combustion in O_2, CO_2 and N_2O oxidizers, and comparison with model calculations, Symposium (International) on Combustion 27 (2) (1998) 2421–2429.

[33] C. K. Law, A simplified theoretical model for the vapor-phase combustion of metal particles, Combustion Science and Technology 7 (5) (1973) 197–212.

[34] P. E. DesJardin, J. D. Felske, M. D. Carrara, Mechanistic model for aluminum particle ignition and combustion in air, Journal of Propulsion and Power 21 (3) (2005) 478–485.

[35] T. Li, F. Heck, F. Reinauer, et al., Visualizing particle melting and nanoparticle formation during single iron particle oxidation with multi-parameter optical diagnostics, Combustion and Flame 245 (2022) 112357.

[36] D. Ning, Y. Shoshin, J. A. van Oijen, et al., Critical temperature for nanoparticle cloud formation during combustion of single micron-sized iron particle, Combustion and Flame 244 (2022) 112296.

[37] E. L. Dreizin, Experimental study of stages in aluminium particle combustion in air, Combustion and Flame 105 (4) (1996) 541–556.

[38] T. Bazyn, H. Krier, N. Glumac, Evidence for the transition from the diffusion-limit in aluminum particle combustion, Proceedings of the Combustion Institute 31 (2) (2007) 2021–2028.

[39] S. Mohan, M. A. Trunov, E. L. Dreizin, On possibility of vapor-phase combustion for fine aluminum particles, Combustion and Flame 156 (11) (2009) 2213–2216.

[40] J. Glorian, L. Catoire, S. Gallier, et al., Gas-surface thermochemistry and kinetics for aluminum particle combustion, Proceedings of the Combustion Institute 35 (2) (2015) 2439–2446.

[41] R. A. Yetter, G. A. Risha, S. F. Son, Metal particle combustion and nanotechnology, Proceedings of the Combustion Institute 32 (2) (2009) 1819–1838.

[42] D. S. Sundaram, P. Puri, V. Yang, A general theory of ignition and combustion of nano-and micron-sized aluminum particles, Combustion and Flame 169 (2016) 94–109.

[43] H. A. Wriedt, The Fe-O (iron-oxygen) system, Journal of Phase Equilibria 12 (2) (1991) 170–200.

[44] M. W. Chase, NIST-JANAF thermochemical tables, Journals of Physical Chemistry 9 (1998).

[45] J. R. Taylor, A. T. Dinsdale, M. Hilleit, et al., A Critical assessment of thermodynamic and phase diagram data for the Al-O system, Calphad 16 (2) (1992) 173–179.

[46] J. Zhang, Z. Xia, O. T. Stein, et al., Combustion characteristics of aluminum particle jet flames in a hot co-flow, Chemical Engineering Journal 442 (2022) 135876.

[47] M. Yang, J. Zhang, S. Zhong, et al., CFD modeling of biomass combustion and gasification in fluidized bed reactors using a distribution kernel method, Combustion and Flame 236 (2022) 111744.

[48] H. G. Weller, G. Tabor, H. Jasak, et al., A tensorial approach to computational continuum mechanics using object-oriented techniques, Computers in Physics 12 (6) (1998) 620–631.

[49] X. Mi, A. Fujinawa, J. M. Bergthorson, A quantitative analysis of the ignition characteristics of fine iron particles, Combustion and Flame 240 (2022) 112011.

[50] W. E. Ranz, W. R. Marshall, Evaporation from drops, Chemical Engineering Progress 48 (3) (1952) 141–146.

[51] M. Renksizbulut, M. C. Yuen, Experimental study of droplet evaporation in a high-temperature air stream, ASME Journal of Heat and Mass Transfer 105 (2) (1983) 384–388.

[52] Y. Wang, S. Verhelst, Comparative analysis and optimisation of hydrogen combustion mechanism for laminar burning velocity calculation in combustion engine modelling, International Journal of Hydrogen Energy 56 (2024) 880–893.

[53] C. Olm, I. G. Zsély, R. Pálvölgyi, et al., Comparison of the performance of several recent hydrogen combustion mechanisms, Combustion and Flame 161 (9) (2014) 2219–2234.

[54] T. Varga, T. Nagy, C. Olm, et al., Optimization of a hydrogen combustion mechanism using both direct and indirect measurements, Proceedings of the Combustion Institute 35 (1) (2015) 589–596.

[55] G. P. Smith, Y. Tao, H. Wang. Foundational Fuel Chemistry Model Version 1.0 (FFCM-1) [online] (2016). Accessed: 2024-03-24.

[56] A. A. Konnov, Yet another kinetic mechanism for hydrogen combustion, Combustion and Flame 203 (2019) 14–22.

[57] Reaction Design, CHEMKIN PRO 2020R2, Software (2020).

[58] D. B. Wilson, T. A. Steinberg, J. M. Stoltzfus, Thermodynamics and kinetics of burning iron, ASTM Special Technical Publication 1319 (1997) 240–257.

[59] M. H. Davies, M. T. Simnad, C. E. Birchenall, On the mechanism and kinetics of the scaling of iron, Journal of The Minerals, Metals & Materials Society 3 (10) (1951) 889–896.

[60] J. Païdassi, The kinetics of the air oxidation of iron in 700–1250°C, Acta Metallurgica 6 (3) (1958) 184–194.

[61] A. S. Khanna, Chapter 5–High Temperature Oxidation, in: M. Kutz (Ed.), Handbook of Environmental Degradation of Materials, 2nd Edition, William Andrew Publishing, Oxford, 2012, pp. 127–194.

[62] R. E. Bedworth, N. B. Pilling, The oxidation of metals at high temperatures, Journal of the Institute of Metals 29 (3) (1923) 529–582.

[63] R. Y. Chen, W. Y. D. Yeun, Review of the high-temperature oxidation of iron and carbon steels in air or oxygen, Oxidation of Metals 59 (5) (2003) 433–468.

[64] M. A. Trunov, M. Schoenitz, E. L. Dreizin, Effect of polymorphic phase transformations in alumina layer on ignition of aluminium particles, Combustion Theory and Modelling 10 (4) (2006) 603–623.

[65] S. Mohan, L. Furet, E. L. Dreizin, Aluminum particle ignition in different oxidizing environments, Combustion and Flame 157 (7) (2010) 1356–1363.

[66] M. A. Gurevich, G. E. Ozerova, A. Stepanov, Heterogeneous ignition of an aluminum particle in oxygen and water vapor, Combustion, Explosion and Shock Waves 6 (3) (1970) 291–297.

[67] M. Leitner, T. Leitner, A. Schmon, et al., Thermophysical properties of liquid aluminum, Metallurgical and Materials Transactions A 48 (2017) 3036–3045.

[68] J. R. Rumble. CRC Handbook of Chemistry and Physics 105th Edition [online] (2025). Accessed: 2025-01-06.

[69] A. F. Chebanov, Determination of the temperature dependence of the bulk modulus of elasticity of certain pure metals, Soviet Materials Science 27 (1992) 184–188.

[70] J. F. Shackelford, Y.-H. Han, S. Kim, et al., CRC materials science and engineering handbook (4th Edition), CRC Press, Boca Raton, FL, 2012.

[71] V. Rosenband, Thermo-mechanical aspects of the heterogeneous ignition of metals, Combustion and Flame 137 (3) (2004) 366–375.

[72] T. Hidayat, D. Shishin, E. Jak, et al., Thermodynamic reevaluation of the Fe-O system, Calphad 48 (2015) 131–144.

[73] T. Hazenberg, J. A. van Oijen, Structures and burning velocities of flames in iron aerosols, Proceedings of the Combustion Institute 38 (3) (2021) 4383–4390.

[74] D. Ning, Y. Shoshin, J. A. van Oijen, et al., Burn time and combustion regime of laser-ignited single iron particle, Combustion and Flame 230 (2021) 111424.

[75] T. A. Steinberg, J. Kurtz, D. B. Wilson, The solubility of oxygen in liquid iron oxide during the combustion of iron rods in high-pressure oxygen, Combustion and Flame 113 (1) (1998) 27–37.

[76] M. Muller, H. El-Rabii, R. Fabbro, Liquid phase combustion of iron in an oxygen atmosphere, Journal of Materials Science 50 (9) (2015) 3337–3350.

[77] M. W. Beckstead, A summary of aluminum combustion, Tech. Rep. N00014-95-1-1338, Brigham Young Univ., Ut (2004).

[78] D. B. Spalding, The combustion of liquid fuels, Symposium (International) on Combustion 4 (1) (1953) 847–864.

[79] R. E. Honig, Vapor pressure data for the solid and liquid elements, RCA Review 23 (12) (1962) 295.

[80] J. Glorian, S. Gallier, L. Catoire, On the role of heterogeneous reactions in aluminum combustion, Combustion and Flame 168 (2016) 378–392.

[81] E. L. Dreizin, A. V. Suslov, M. A. Trunov, General trends in metal particles heterogeneous combustion, Combustion Science and Technology 90 (1-4) (1993) 79–99.

[82] Y. Huang, G. A. Risha, V. Yang, et al., Analysis of nano-aluminum particle dust cloud combustion in different oxidizer environments, in: 43rd AIAA Aerospace Sciences Meeting and Exhibit, 2005.

[83] J. Glorian, Cinétique hétérogène pour la combustion de l' aluminium, Ph.D. thesis, ENSTA ParisTech (2014).

[84] T. Emi, W. M. Boorstein, R. D. Pehlke, Absorption of gaseous oxygen by liquid iron, Metallurgical Transactions 5 (9) (1974) 1959–1966.

[85] S. Ban-Ya, J.-D. Shim, Rate of oxidation of liquid iron by pure oxygen, Tetsu To Hagane-journal of The Iron and Steel Institute of Japan 66 (12) (1980) 1631–1639.

[86] M. Soo, X. C. Mi, S. Goroshin, et al., Combustion of particles, agglomerates, and suspensions – A basic thermophysical analysis, Combustion and Flame 192 (2018) 384–400.

[87] K. Chattopadhyay, R. Goswami, Melting and superheating of metals and alloys, Progress in Materials Science 42 (1-4) (1997) 287–300.

[88] J.-Y. Choi, I.-S. Jeung, Y. Yoon, Computational fluid dynamics algorithms for unsteady shock-induced combustion, part 1: Validation, AIAA journal 38 (7) (2000) 1179–1187.

[89] R. J. Kee, G. Dixon-Lewis, J. Warnatz, et al., A Fortran computer code package for the evaluation of gas-phase multicomponent transport properties, Tech. Rep. SAND-86-8246, Sandia National Labs, Livermore, CA (1986).

[90] R. C. Rocha, S. Zhong, L. Xu, et al., Structure and laminar flame speed of an ammonia/methane/air premixed flame under varying pressure and equivalence ratio, Energy & Fuels 35 (9) (2021) 7179–7192.

[91] N. T. Ouellette, H. Xu, E. Bodenschatz, A quantitative study of three-dimensional lagrangian particle tracking algorithms, Experiments in Fluids 40 (2006) 301–313.

[92] A. Roth, M. Stiti, A. Matamis, et al., Analysis of coughed droplets using stereoscopic high-speed imaging, in: ICLASS 2021, 15th Triennial International Conference on Liquid Atomization and Spray Systems, 2021.

[93] A. Braconnier, C. Chauveau, F. Halter, et al., Detailed analysis of combustion process of a single aluminum particle in air using an improved experimental approach, International Journal of Energetic Materials and Chemical Propulsion 17 (2018) 111–124.

[94] A. Elfasakhany, T. Klason, X.-S. Bai, Modelling of pulverised wood combustion using a functional group model, Combustion Theory and Modelling 12 (5) (2008) 883–904.

[95] A. Elfasakhany, L. Tao, B. Espenas, et al., Pulverised wood combustion in a vertical furnace: Experimental and computational analyses, Applied Energy 112 (2013) 454–464.

[96] K. P. Brooks, M. W. Beckstead, Dynamics of aluminum combustion, Journal of Propulsion and Power 11 (4) (1995) 769–780.

[97] C. K. Law, Combustion Physics, Cambridge University Press, Cambridge, 2010.

[98] M. W. Beckstead, Correlating aluminum burning times, Combustion, Explosion, and Shock Waves 41 (5) (2005) 533–546.

[99] E. B. Washburn, J. N. Trivedi, L. Catoire, et al., The simulation of the combustion of micrometer-sized aluminum particles with steam, Combustion Science and Technology 180 (8) (2008) 1502–1517.

[100] E. B. Washburn, J. A. Webb, M. W. Beckstead, The simulation of the combustion of micrometer-sized aluminum particles with oxygen and carbon dioxide, Combustion and Flame 157 (3) (2010) 540–545.

[101] M. T. Swihart, L. Catoire, Thermochemistry of aluminum species for combustion modeling from ab initio molecular orbital calculations, Combustion and Flame 121 (1) (2000) 210–222.

[102] M. T. Swihart, L. Catoire, B. Legrand, et al., Rate constants for the homogeneous gas-phase Al/HCl combustion chemistry, Combustion and Flame 132 (1-2) (2003) 91–101.

[103] L. Catoire, J.-F. Legendre, M. Giraud, Kinetic model for aluminum-sensitized ram accelerator combustion, Journal of Propulsion and Power 19 (2) (2003) 196–202.

[104] N. L. Garland, H. H. Nelson, Temperature dependence of the kinetics of the reaction Al + O_2 → AlO + O, Chemical Physics Letters 191 (3-4) (1992) 269–272.

[105] N. L. Garland, C. H. Douglass, H. H. Nelson, Pressure and temperature dependence of the kinetics of the reaction Al + CO_2, The Journal of Physical Chemistry 96 (21) (1992) 8390–8394.

[106] D. F. Rogowski, A. J. English, A. Fontijn, A high-temperature fast-flow-reactor kinetics study of the reaction AlO + CO_2 → AlO_2 + CO. Thermochemical implications, The Journal of Physical Chemistry 90 (8) (1986) 1688–1691.

[107] D. P. Belyung, A. Fontijn, The AlO + O_2 reaction system over a wide temperature range, The Journal of Physical Chemistry 99 (32) (1995) 12225–12230.

[108] R. E. McClean, H. H. Nelson, M. L. Campbell, Kinetics of the reaction Al($^2P^0$) + H_2O over an extended temperature range, The Journal of Physical Chemistry 97 (38) (1993) 9673–9676.

[109] M. W. Beckstead, Y. Liang, K. V. Pudduppakkam, Numerical simulation of single aluminum particle combustion, Combustion, Explosion and Shock Waves 41 (2005) 622–638.

[110] A. S. Sharipov, N. S. Titova, A. M. Starik, Evaluation of the reaction rate constants for the gas-phase Al-CH_4-air combustion chemistry, Combustion Theory and Modelling 16 (5) (2012) 842–868.

[111] A. M. Starik, P. S. Kuleshov, A. S. Sharipov, et al., Kinetics of ignition and combustion in the Al-CH_4-O_2 system, Energy & Fuels 28 (10) (2014) 6579–6588.

[112] A. M. Starik, P. S. Kuleshov, A. S. Sharipov, et al., Numerical analysis of nanoaluminum combustion in steam, Combustion and Flame 161 (6) (2014) 1659–1667.

[113] S. Álvarez-Barcia, J. R. Flores, The interaction of Al atoms with water molecules: A theoretical study, The Journal of Chemical Physics 131 (17) (2009) 174307.

[114] D. P. Belyung, A. Fontijn, P. Marshall, Gas-phase reactions between hydrocarbons and metal oxides: The AlO + CH_4 reaction from 590 to 1380 K, The Journal of Physical Chemistry 97 (14) (1993) 3456–3459.

[115] Y. Huang, G. A. Risha, V. Yang, et al., Effect of particle size on combustion of aluminum particle dust in air, Combustion and Flame 156 (1) (2009) 5–13.

[116] M. Saba, T. Kato, T. Oguchi, Chemical kinetics modeling for combustion of Al in CO_2, Combustion and Flame 233 (2021) 111613.

[117] M. Saba, T. Kato, T. Oguchi, Reaction modeling study on the combustion of aluminum in gas phase: The Al + O_2 and related reactions, Combustion and Flame 225 (2021) 535–550.

[118] V. B. Storozhev, A. N. Yermakov, On the interplay of chemical and physical processes during the combustion of aluminum in water vapor, Russian Journal of Physical Chemistry B 8 (2014) 672–679.

[119] V. B. Storozhev, A. N. Yermakov, Combustion of nano-sized aluminum particles in steam: Numerical modeling, Combustion and Flame 162 (11) (2015) 4129–4137.

[120] V. B. Storozhev, A. N. Yermakov, Effect of suboxides on dynamics of combustion of aluminum nanopowder in water vapor: Numerical estimate, Combustion and Flame 190 (2018) 103–111.

[121] V. B. Storozhev, A. N. Yermakov, Activation of aluminum nanopowder combustion in water vapor by O_2 additions, Combustion and Flame 200 (2019) 82–84.

[122] V. B. Storozhev, A. N. Yermakov, Effect on combustion of oxide coating formed on aluminum nanoparticles burned in steam, Combustion and Flame 226 (2021) 182–189.

[123] Z. Hu, T. Yang, Z. Xia, et al., The simulation of different combustion stages of micron-sized aluminum particles, Applied Sciences 11 (4) (2021) 1774.

[124] A. M. Starik, A. M. Savel'ev, N. S. Titova, Specific features of ignition and combustion of composite fuels containing aluminum nanoparticles, Combustion, Explosion, and Shock Waves 51 (2015) 197–222.

Scientific publications

Author contributions

Co-authors are abbreviated as follows in the text:
Yue Qiu (Y.Q), Sheng Feng (S.F), Shijie Xu (SJ.X), Leilei Xu (LL.X), Jianqing Huang (JQ.H), Shen Li (S.L), Elna J.K. Nilsson (E.N), Zhongshan Li (ZS.L), Weiwei Cai (WW.C), Marcus Aldén (M.A), Xue-Song Bai (XS.B), Zhiyong Wu (ZY.W), Can Ruan (C.R), Adrian Roth (A.R), Edouard Berrocal (E.B)

Paper 1: Phase change and combustion of iron particles in premixed CH_4 / O_2 / N_2 flames

Shijie Xu, **Yue Qiu**, Leilei Xu, Jianqing Huang, Shen Li, Elna J.K. Nilsson, Zhongshan Li, Weiwei Cai, Marcus Aldén, Xue-Song Bai.

In this paper, a new phenomenological five-stage "Point particle model" describing the single Fe particle combustion is constructed based on a literature review and the experimental findings from collaborators. The model is implemented in OpenFOAM based on the Eulerian-Lagrangian framework, and validated with experimental data. A "super-cooled solidification" sub-model is proposed to explain the intensity jump observed at the start of solidification.

The author (Y.Q) and SJ.X developed the model together. Y.Q did the literature review to construct the five sub-stage kinetic model. SJ.X implemented the model in OpenFOAM, did the simulation, results analysis, and most writing. LL.X did results visualization and analysis together with SJ.X. Y.Q wrote the initial draft of Section 2.1 "Solid/liquid phase oxidation", Section 2.2 "Melting and solidification", Section 4.1 "Five-stage behaviour of iron combustion", and Section 4.2 "Melting". JQ.H and S.L provided the experimental data and participated in the analysis of the results. E.N, ZS.L, WW.C, M.A, and XS.B supervised the work and revised the draft.

Paper II: Modeling of micron-sized aluminum particle combustion in hot gas flow

Sheng Feng, **Yue Qiu**, Shijie Xu, Zhiyong Wu, Can Ruan, Adrian Roth, Elna J.K. Nilsson, Edouard Berrocal, Zhongshan Li, Marcus Aldén, Xue-Song Bai.

In this paper, a phenomenological Al "Point particle model" describing the ignition and combustion of a micron-sized single Al particle is constructed based on the literature review and experimental data from collaborators. The model is then implemented within the Eulerian-Lagrangian framework in OpenFOAM and validated with experimental data. The special egg-shell morphology from the collected products is also addressed.

XS.B did the conceptualization, coordination, and part of the "Results and discussion". Y.Q developed the model and implemented it together with S.F. Y.Q did the simulation, results analysis, and writing together with S.F. ZY.W, C.R, and A.R offered experimental data and participated in the analysis of the results. E.N, E.B, ZS.L, M.A, and XS.B supervised the work and reviewed the manuscript.

Paper III: Detailed numerical simulation and experiments of a steadily burning micron-sized aluminum droplet in hot steam

Yue Qiu, Sheng Feng, Zhiyong Wu, Shijie Xu, Can Ruan, Xue-Song Bai, Elna J.K. Nilsson, Marcus Aldén, Zhongshan Li.

In this paper, a "Boundary layer resolved model" is proposed to resolve the detailed flame structure in the vicinity of a burning Al droplet. The model is implemented within the Eulerian framework in OpenFOAM, and the simulation results demonstrate agreeable consistency with experimental data. Meanwhile, it is pointed out that the heat from the flame zone only accounts for a portion of the evaporation heat needed. Other heat sources should also be considered.

Y.Q developed the model and implemented it in OpenFOAM with the help of XS.B. Y.Q did the simulation, results analysis, and most writing. E.N wrote the introduction. S.F and SJ.X participated in the results analysis, illustration, and paper review. C.R and ZY.W provided the experimental data and participated in the analysis of the results. XS.B, E.N, M.A, and ZS.L supervised the work and helped review the manuscript.

Paper IV: A comprehensive review of aluminum gas phase combustion kinetics in oxygen and steam environments

Yue Qiu, Elna J.K. Nilsson, Xue-Song Bai.

In this paper, the Al gas-phase combustion kinetics in oxygen and steam environments are comprehensively reviewed and evaluated for the first time. Crucial elementary reactions together with their rate constants are scrutinized based on literature data and simulations in CHEMKIN. The global performance of different mechanisms is evaluated with an in-house CFD model in comparison with experimental data. Quantification of heat release and H_2 production from Al / H_2O combustion is illustrated. Suggestions are made for future research on Al combustion kinetics and an appropriate selection of mechanisms for CFD simulations.

E.N did the conceptualization, coordination, and initial literature review study of the elementary reactions. Y.Q followed and furthered the literature review. Y.Q did the simulation, results analysis, and most writing. E.N and XS.B supervised the work and revised the manuscript.

Paper v: An updated kinetic mechanism for aluminum gas phase combustion in oxygen and steam environments

Yue Qiu, Elna J.K. Nilsson, Xue-Song Bai.

This is a follow-up work of paper IV. In this paper, an updated $Al / O_2 / H_2O$ mechanism is proposed and analyzed, unifying the various mechanisms in the literature. The updated mechanism combines both experimental measurements and theoretical calculations from different sources. The proposed mechanism is then compared with other mechanisms from the literature, where important elementary reactions in the quantification of the flame structure are identified. The reaction pathways in different cases are analyzed. Quantification of heat release and H_2 production from Al / H_2O combustion with different mechanisms is illustrated. Meanwhile, suggestions are made for future efforts on Al combustion kinetics for CFD simulations.

XS.B did the conceptualization. E.N did the coordination. Y.Q did the literature review, the construction of the updated mechanism, the simulation, the results analysis, and most writing. E.N and XS.B supervised the work and revised the manuscript.